CHARACTERIZATION OF POINT DEFECTS IN LITHIUM ALUMINATE ($LiAlO_2$) SINGLE CRYSTALS

DISSERTATION

Maurio S. Holston, CPT, USA

AFIT-ENP-DS-15-S-025

DEPARTMENT OF THE AIR FORCE
AIR UNIVERSITY

AIR FORCE INSTITUTE OF TECHNOLOGY

Wright-Patterson Air Force Base, Ohio

AFIT-ENP-DS-15-S-025

CHARACTERIZATION OF POINT DEFECTS IN LITHIUM ALUMINATE ($LiAlO_2$) SINGLE CRYSTALS

DISSERTATION

Presented to the Faculty

Graduate School of Engineering and Management

Air Force Institute of Technology

Air University

Air Education and Training Command

in Partial Fulfillment of the Requirements for the

Degree of Doctor of Philosophy

Maurio S. Holston, BS, MS

CPT, USA

September 2015

AFIT-ENP-DS-15-S-025

CHARACTERIZATION OF POINT DEFECTS IN LITHIUM ALUMINATE ($LiAlO_2$) SINGLE CRYSTALS

DISSERTATION

Maurio S. Holston, BS, MS
CPT, USA

Committee Membership:

John W. McClory, PhD
Chairman

Benjamin F. Akers, PhD
Member

Nancy C. Giles, PhD
Member

Dr. Larry E. Halliburton, PhD
Member

ADEDJI B. BADIRU, PhD
Dean, Graduate School of Engineering and Management

AFIT-ENP-DS-15-S-025

Abstract

Lithium aluminate ($LiAlO_2$) is an insulating wide-band gap material currently under development for tritium breeding and radiation detection and dosimetry applications. Point defects are imperfections in a crystal lattice localized over a few atomic lengths that can alter the electrical, mechanical, or optical properties of materials. An understanding of point defect behavior is a necessary precursor for optimizing lithium aluminate for nuclear technology applications. This dissertation has identified and characterized the major point defects created and induced through x ray and neutron radiation using electron paramagnetic resonance (EPR) and fluorescence spectroscopies, thermoluminescence, and optical absorption. After x ray irradiation, the major hole-trapping defect is found to be a hole trapped on an oxygen ion adjacent to a lithium vacancy. The major electron-trapping defect is found to be an Fe^{2+} ion substituting for a Li^+ ion. During exposure to x rays, an O^{2-} ion next to a lithium vacancy will trap a hole, forming O^-, and an Fe^{2+} ion on a lithium site will trap an electron, forming Fe^+. $LiAlO_2$ diffused with copper has been found to have potential use as an optically stimulated luminescence (OSL) dosimeter. The OSL effect arises from electron-hole recombination occurring at Cu^{2+} ions substituting for Li^+ ions. The major intrinsic defect after neutron irradiation is an F^+ center; an oxygen vacancy with one trapped electron. This defect has two states, a stable state that survives up to 500 °C and a metastable state that survives up to 200 °C. This dissertation explains for the first time the mechanism responsible for OSL in copper-diffused $LiAlO_2$ and characterizes for the first time the intrinsic hole and electron-trapping defects. These results should prove useful in $LiAlO_2$ applications involving radiation.

AFIT-ENP-DS-15-S-025

This dissertation is dedicated to my wife. Thank you for your love and support in this endeavor.

Acknowledgements

I would like to thank Mr. Rob Beimler for suggesting that I attend AFIT in the first place. I never heard of AFIT until you mentioned it and I'm glad you did. I wish to thank Dr. John McClory for serving as my research advisor, Committee Chairman and mentor. You have provided me with valuable insight not only on my research, but also my professional development as an Army officer. Thank you also for your leadership in guiding me through this process and making sure I succeeded. I would like to thank Dr. Larry Halliburton for suggesting $LiAlO_2$ as a material to study, and for being a goldmine of professional and scientific experience. This dissertation is immeasurably better than it would have been without your presence. I would like to thank Dr. Nancy Giles for agreeing to serve on my committee, and for her contributions to my published research. I would like to thank Dr. Benjamin Akers for also agreeing to serve on my committee. I would like to thank 2d Lt Ian Ferguson for helping conduct some of the experiments and for the interesting conversations we had. I would like to thank Mr. Mike Ranft and Mr. Greg Smith for always being ready to provide assistance and for helping keep our equipment up and running. Lastly, I would like to thank Mr. Kevin Herminghuysen and Dr. Susan White at the Ohio State University Nuclear Reactor Lab for their expertise, time, and assistance.

Maurio S. Holston

Table of Contents

Page

Page

List of Figures

List of Tables

CHARACTERIZATION OF POINT DEFECTS IN LITHIUM ALUMINATE ($LiAlO_2$) SINGLE CRYSTALS

I. Introduction

1.1 Motivation

Lithium aluminate ($LiAlO_2$) is an insulating material currently under development by several researchers for various applications. The most important areas of focus are its suitability as a substrate for GaN epitaxy because of a maximum ≈1.7% lattice mismatch [1, 2], as a tritium breeding blanket for fusion reactors [3, 4], as a thermal neutron scintillator material [5, 6], and as a radiation dosimeter using optically stimulated luminescence (OSL) [7–10]. Its application as a tritium breeding blanket, as well as its applications in radiation detection and dosimetry, have important national security considerations and are elaborated upon below.

1.1.1 Tritium Breeding Blanket.

Fusion power offers the promise of near limitless renewable energy and the United States has spent billions of dollars on fusion research in trying to achieve fusion power generation. A controlled fusion reactor attempts to harness the energy released in the deuterium-tritium (D-T) reaction

$$^2\mathrm{H} + {}^3\mathrm{H} \rightarrow {}^4\mathrm{He}\,(3.5\,\mathrm{MeV}) + \mathrm{n}\,(14.1\,\mathrm{MeV}) \qquad (Q = 17.6\,\mathrm{MeV}), \tag{1.1}$$

where ^{2}H is a hydrogen nucleus with one neutron known as deuterium, ^{3}H is a hydrogen nucleus with two neutrons known as tritium, ^{4}He is a helium nucleus that is

referred to as an alpha particle when it is created in nuclear reactions, n is a free neutron, and Q, or Q value, represents the energy released per D-T reaction [11]. A tritium breeding blanket is needed because it enables a fusion reactor to self-generate its own supply of tritium from the neutrons emitted in equation (1.1). This is important because the world supply of tritium is estimated to be around 20 kg [12] while the initial startup tritium supply needed for each fusion reactor is estimated to be 23 kg [13]. By surrounding the fusion chamber with a ceramic blanket of lithium aluminate, tritium can be generated when neutrons from equation (1.1) are absorbed into the blanket and react with the two naturally occurring isotopes of lithium

$$^{6}\mathrm{Li} + \mathrm{n} \rightarrow {}^{3}\mathrm{H}\,(2.75\,\mathrm{MeV}) + {}^{4}\mathrm{He}\,(2.05\,\mathrm{MeV}) \qquad (Q = 4.80\,\mathrm{MeV}) \tag{1.2}$$

$$^{7}\mathrm{Li} + \mathrm{n} \rightarrow {}^{3}\mathrm{H} + {}^{4}\mathrm{He} + \mathrm{n} \qquad (Q = -2.467\,\mathrm{MeV}). \tag{1.3}$$

The ^{6}Li neutron reaction can occur for thermal or higher energy neutrons. The ^{7}Li reaction only occurs for high-energy neutrons because it consumes energy, and its neutron capture cross section is significantly smaller compared to ^{6}Li for the neutron energies that exist in the reactor. After tritium is created from either equation (1.2) or (1.3), it can be extracted through isotopic exchange by running a helium sweep gas with 0.1% hydrogen over the breeder blanket as discussed in [3]. ^{6}Li comprises only 7.5% of natural lithium, so enriching lithium aluminate with ^{6}Li during the crystal-growth process will increase the tritium production for a given volume of $LiAlO_2$.

1.1.2 Neutron Scintillator.

The threat of terrorists employing nuclear materials in an attack, either in a radiological dirty bomb, or an improvised nuclear weapon, is of such concern to national security that the Department of Homeland Security (DHS) has an entire office dedicated to the detection of radiological and nuclear threats [14]. DTRA has developed

a direct relationship with the DHS Domestic Nuclear Detection Office in order to achieve a multi-layered defense strategy to protect the U.S. from nuclear or radiological attack. Crucial to that goal is the development of high-quality neutron detectors since ^{235}U and ^{239}Pu, the two isotopes used to fuel nuclear weapons, both emit neutrons through spontaneous fission of their nuclei. $LiAlO_2$ has shown the potential for improved performance in thermal neutron detection over current detectors [5, 6]. $LiAlO_2$ crystals are especially suited for neutron-detection applications because of the presence of ^{6}Li which has a large thermal neutron capture cross-section. Enriching the crystals with ^{6}Li during growth will increase their sensitivity for detecting neutrons.

The scintillation properties of an inorganic scintillator are determined by the electronic energy states that exist within the crystal lattice. In an insulator or semiconductor there exist discrete bands of energy states that an electron can occupy known as the valence band and conduction band. Electrons in the lower valence band are essentially bound to the crystal lattice sites but electrons in the conduction band can move freely about the crystal lattice. The energy that separates the top of the valence band from the bottom of the conduction band is known as the band gap energy, and is normally represented by E_g. If a photon with an energy equal to or greater than the band gap energy is absorbed by an electron with initial energy E_0 in the valence band, that electron will be excited into the conduction band with a final energy E_f, while leaving behind a hole in the normally filled valence band [15]. This process is known as the creation of an electron-hole pair. An electron in the conduction band will relax to the bottom of the conduction band, before emitting energy and returning to the valence band in the process of electron-hole recombination [16]. When the process of electron-hole recombination includes photon emission it is known as radiative recombination as depicted in Figure 1.1.

In a pure crystal, the process of photon emission from electron-hole recombination

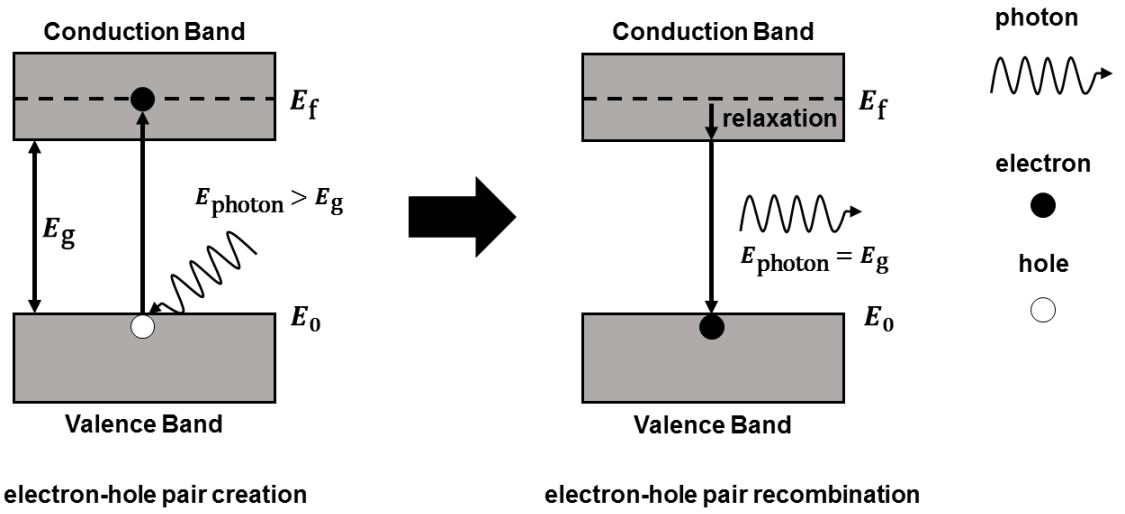

Figure 1.1. An electron-hole pair is created when an electron in the valence band absorbs a photon and is excited into the conduction band. E_0 is the initial energy state of the electron and E_f the final energy state. An electron will then relax to the bottom of the conduction band and then return to the valence band through the emission of a photon.

is not an efficient process, and typical band gap energies are so high that the energy of the emitted photon would not be in the visible light range [17]. To circumvent this problem, impurities are introduced into the pure crystal in a process known as doping. These dopants have the effect of introducing energy levels within the normally forbidden range of energies inside the band gap known as activator states. Electrons excited to the conduction band in electron-hole pair creation can then non-radiatively relax to these activator states. When these electrons de-excite to the ground state of the activator levels, the photons they emit have an energy less than that of the full band gap. These photons may be in the visible spectrum, if the correct dopant is chosen, and can transmit through the crystal to a photodetector. The activator sites are also known as luminescence centers or recombination centers, and their energy structure within the crystal lattice will determine the emission spectrum of the scintillator. Figure 1.2 shows how activators affect the energy levels and emission of light.

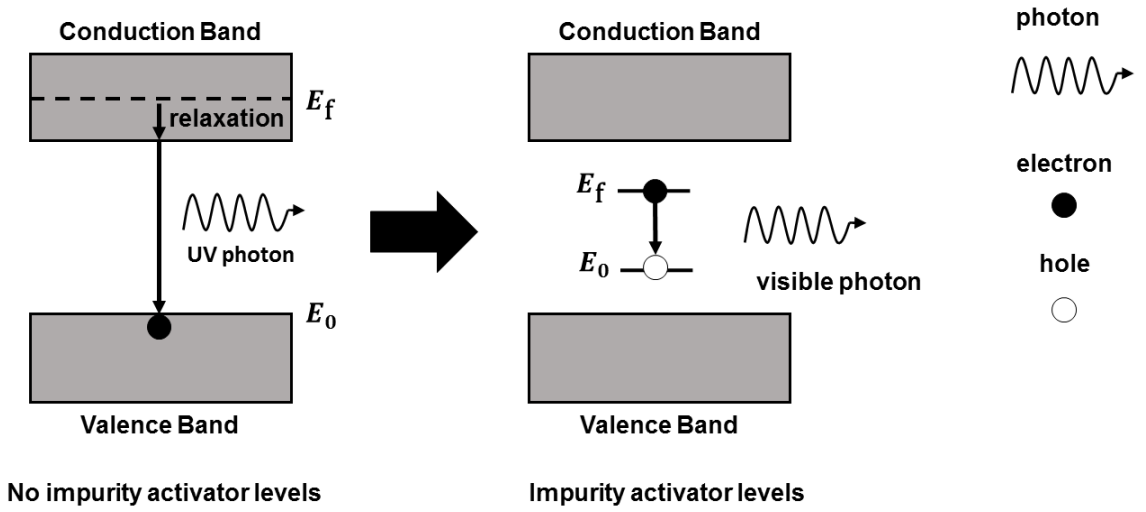

Figure 1.2. Adding impurities to a material introduces new energy levels within the band gap. Electrons that de-excite from an activator excited state to a ground state can emit light in the visible wavelength range.

As an energetic charged particle such as an electron or an alpha particle moves through the scintillator medium, they will transfer their kinetic energy to electrons in the valence band and create electron-hole pairs. Compounds like $LiAlO_2$ can serve as neutron scintillators because neutron-lithium reactions will create charged particles, such as the alpha particle from equations (1.2) and (1.3), that will cause light scintillation through the creation of electron-hole pairs and activator site photon emission. Lithium is one of the elements frequently present in neutron scintillators because its ^{6}Li isotope has a relatively high neutron interaction probability, with a neutron capture cross section of several hundred barns at thermal neutron energies. As with the tritium breeding blanket, the neutron detector may be enriched to higher concentrations of ^{6}Li [18].

1.1.3 Dosimetry.

A personal dosimeter measures how much ionizing radiation a person has been exposed to. This is critically important for people who regularly work with radioac-

tive materials, and dosimeters are used by military personnel when they conduct operations in a radiologically contaminated environment. The military has regulations that govern the lifetime exposures of service members, and if these exposures are met the service member would be permanently unable to serve in a radiological environment. This is why it is very important that accurate and reliable dosimeters are available. There is existing research which indicates that $LiAlO_2$ may hold the promise of exceeding the performance of commercially available dosimeters for mixed-field dosimetry (neutrons and gamma rays) [10].

A dosimeter is an integrating passive detector that works by trapping electrons and holes at activator states within the band gap during exposure to ionizing radiation. Unlike the neutron scintillator, however, where the electrons and holes immediately recombine and emit light, the trapped charge in dosimeters will remain that way until exposed to some form of stimulation that induces recombination. The number of trapped charges created in ionizing radiation interactions is related to the absorbed dose of incident radiation, and the population will continue to build up through subsequent exposures until the trapped charges are released. The release of trapped charge can occur through heat, in a process known as thermoluminescence (TL), or through optical means, known as optically stimulated luminescence (OSL). While the dosimeter material is being "read" or stimulated with heat or light, the trapped charges are recombining and emitting photons, and the number of emitted photons is proportional to the deposited energy integrated over the exposure time. This then provides a measure of the radiation dose to which a dosimeter has been exposed. Sections 2.4 and 2.5 elaborate further on the theory of these techniques.

1.2 Research Objectives

Most of the research on $LiAlO_2$ has focused on its optical properties and bulk physical properties such as its structural integrity [19] or thermal conductivity [20] after neutron irradiation. Attempts to truly understand the behavior of lithium aluminate on a fundamental level, through the study of point defects, have been very limited. For any solid state device, point defects play an important role, sometimes the most important role, in determining how that device will function. Point defects are defined as imperfections in the lattice of crystalline solids that are localized over a few atomic sites [21]. Figure 1.3 shows the four fundamental point defects. The first three are considered intrinsic defects: antisite defects which occur whenever an element of a compound occupies the wrong lattice site; interstitial defects which occur whenever atoms occupy non-lattice sites; and vacancy defects which occur whenever an atom is missing from its normal lattice position. The last point defect in Figure 1.3 is an extrinsic defect known as an impurity that occurs whenever a foreign atom has entered the crystal lattice. More complicated point defect structures can be created from combinations of the four shown in Figure 1.3.

Point defects are important because of the effects they can have on a given material and any devices made from that material. The most well known example of point defects altering material properties is semiconductor doping. When a semiconductor is doped to make it $p-$type (holes are the dominant charge carrier) or $n-$type (electrons are the dominant charge carrier), impurity ions are added to the crystal lattice of the semiconductor which replace regular lattice ions, subsequently altering the electrical properties. Point defects can change the optical properties of materials as well; chlorine vacancies in KCl cause the normally colorless crystal to turn purple because they cause light in the $450-650\,\text{nm}$ range to be absorbed (purple is the primary color of the transmitted light) [22]. Point defects can also modify the me-

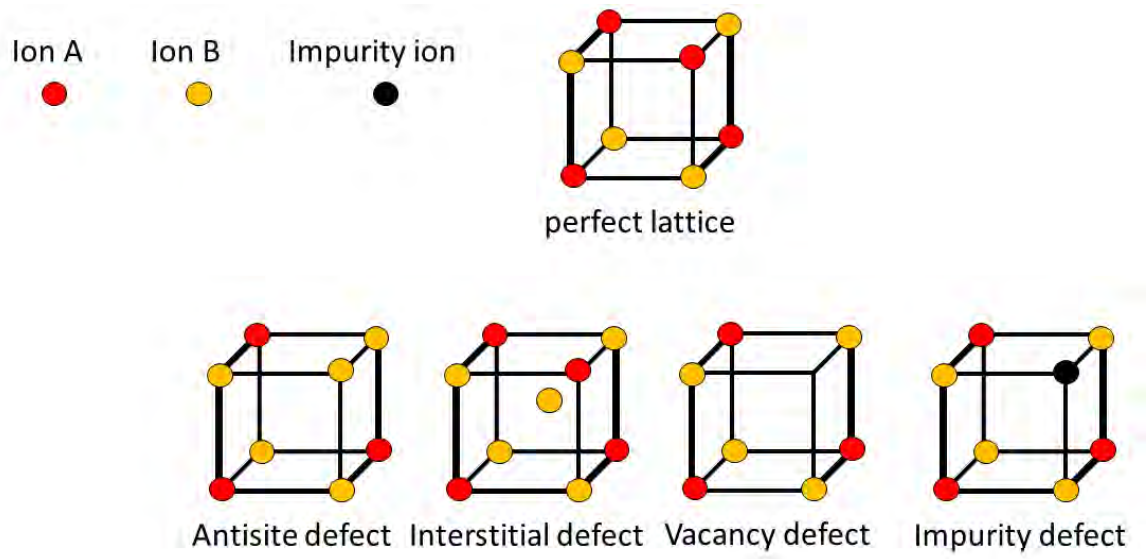

Figure 1.3. Examples of the four fundamental point defects for crystalline solids are shown above. More complicated point defects structures are created from combinations of these four.

chanical properties of materials; point defect hardening occurs when point defects act as obstacles to dislocation motion caused by stress, increasing a materials resistance to plastic deformation [23].

An understanding of how point defects behave and the effects they cause in lithium aluminate will be vital to optimizing device applications for this material. While there have been many papers attempting to characterize the bulk properties of $LiAlO_2$, only three research papers since 1988 have attempted to understand point defect behavior in single crystals of $LiAlO_2$ [24–26]. In the present study, an examination of the point defects induced in $LiAlO_2$ by ionizing and non-ionizing radiation has been conducted using electron paramagnetic resonance (EPR), thermoluminescence (TL), optical absorption, and fluorescence spectroscopy. EPR is particularly useful in identifying paramagnetic defects and describing their environment. Ionizing radiation such as x rays create electron-hole pairs in materials, and while this doesn't normally create point defects at typical x ray energies, it can make a non-paramagnetic defect paramagnetic if it gains or loses an electron. This is necessary because EPR can only

measure paramagnetic species. High-energy electrons not only create electron-hole pairs but also have the possibility of inducing lattice ion displacements through collisions. Neutron irradiation will primarily create lattice defects such as interstitials and vacancies, but can also produce ionizing radiation effects through secondary reactions.

The theory underlying the experimental techniques is explained in Chapter 2. Chapter 3 describes in detail the experimental equipment used in this study. Chapter 4 describes the characterization of the primary intrinsic point defect in as-grown lithium aluminate crystals; a hole trapped near an oxygen ion that is adjacent to a lithium vacancy. Chapter 5 describes the characterization of the primary extrinsic point defect caused by iron impurities; an Fe^{2+} ion that has substituted for a Li^{+} ion. Chapter 6 describes the OSL mechanism in copper-diffused $LiAlO_2$ crystals. Chapter 7 describes the characterization of the point defects induced in $LiAlO_2$ by neutron irradiation, and Chapter 8 summarizes the key results and conclusions of this dissertation. The following section will explain some basic properties of $LiAlO_2$.

1.3 Properties of $LiAlO_2$

$LiAlO_2$ is an insulator that can be grown into three distinct crystal structures which are referred to in the literature as α-phase, β-phase, and γ-phase [28]. α-$LiAlO_2$ has a hexagonal structure where the cations have octahedral coordination. In this structure each lithium and aluminum ion is surrounded by six oxygen ions. α-$LiAlO_2$ also has the highest density of the three phases at $3.401\,\mathrm{g\,cm^{-3}}$ which makes it the most stable of the phases at high pressure [29]. β-$LiAlO_2$ has an orthorhombic crystal structure and the aluminum ions have both tetrahedral and octahedral coordination with the oxygen ions. Tetrahedral coordination has each lithium and aluminum ion surrounded by four oxygen ions. β-$LiAlO_2$ has a density of $2.61\,\mathrm{g\,cm^{-3}}$ and can be converted to the γ-phase by heating to $900\,^{\circ}\mathrm{C}$ [30, 31].

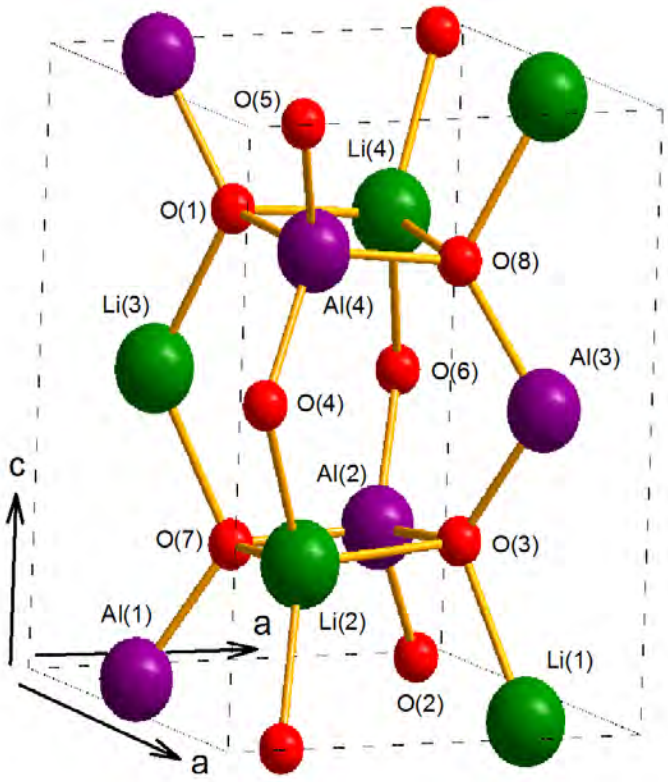

Figure 1.4. A 3D representation of the unit cell of γ-$LiAlO_2$ viewed from an arbitrary direction. The green spheres represent lithium, the violet are aluminum, and the red spheres are oxygen. The labels of the ions correspond to the coordinates given in Table 1.2. This was drawn using Diamond v. 3.0 software [27].

γ-$LiAlO_2$ is the most commonly occurring phase and the one used in the various applications that have been discussed previously. This phase will be the focus of the current study and all subsequent references to $LiAlO_2$ in this study are to the γ-phase. The Hermman-Maugiun symbol for γ-$LiAlO_2$ is $P4_12_12$ with space group number 92 [32]. This is a tetragonal crystal structure with cell dimensions $a = 5.1687\,\text{Å}$ and $c = 6.2697\,\text{Å}$, a calculated density of $2.615\,\text{g}\,\text{cm}^{-3}$, and with each cation tetrahedrally coordinated with the oxygen ions [33]. The tetrahedral coordination can be looked at in one of two ways. It can be visualized as each oxygen ion forming the vertices of lithium and aluminum centered tetrahedra, or conversely, the aluminum and lithium ions can be thought of as forming the vertices of oxygen centered tetrahedra. The

Table 1.1. Anion - Cation Bond Lengths

Bond	Bond Length (Å)
O(7) - Li(2)	2.059
O(7) - Li(3)	1.948
O(7) - Al(1)	1.755
O(7) - Al(2)	1.767

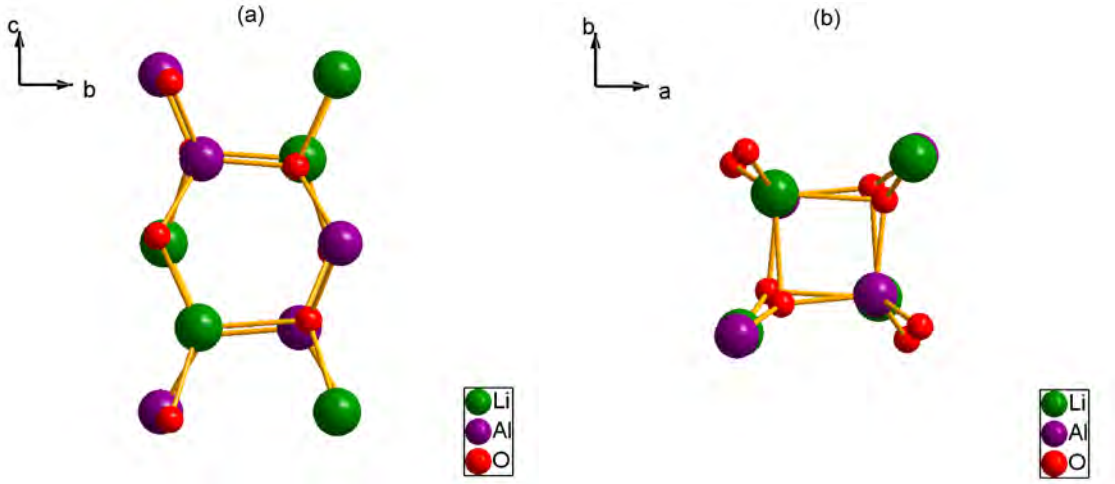

Figure 1.5. A 3D representation of the $LiAlO_2$ crystal structure drawn using Diamond v. 3.0 software [27]. The green spheres represent lithium, the violet are aluminum, and the small red spheres are oxygen. (a) The unit cell viewed from the [100] direction. (b) The unit cell viewed from the [001] direction.

crystal structure is then built upon an infinite three dimensional array of tetrahedra that have certain edges and vertices in common. Symmetry operations are a four-fold rotation about the [001] direction, twofold rotations about the [100] and [010] directions, and a twofold rotation about the [110] direction.

Figure 1.4 is a 3D representation of the $LiAlO_2$ crystal structure viewed from an arbitrary direction with all of the ions in a unit cell visible. Each ion is equivalent to every other ion of the same element but the lithium and aluminum ions that surround each oxygen are not equivalent relative to the oxygen. The differences in the bond lengths are shown in Table 1.1.

Figure 1.5 shows the crystal structure of lithium aluminate from two different viewing directions. The figure shows how the tetrahedra are distorted from normal

Table 1.2. $LiAlO_2$ Unit Cell Ion Coordinates in Angstroms [34]

Ion	x	y	z
Li (1)	4.200	4.200	0.000
Li (2)	3.553	1.616	1.567
Li (3)	0.969	0.969	3.134
Li (4)	1.616	3.553	4.701
Al (1)	0.909	0.909	0.000
Al (2)	1.675	3.494	1.567
Al (3)	4.260	4.260	4.292
Al (4)	3.494	1.675	4.701
O (1)	1.741	1.502	4.841
O (2)	1.082	4.326	0.140
O (3)	3.427	3.667	1.707
O (4)	4.086	0.843	3.274
O (5)	4.326	1.082	6.128
O (6)	0.843	4.086	2.994
O (7)	1.502	1.741	1.427
O (8)	3.667	3.427	4.561

because the structure has to accommodate metallic ions of different sizes. The Li and Al ions occupy the Wyckoff special position of 4a(x,x,0) while the O ions occupy the general position of 8b(x,y,z) [35]. The coordinates of every ion in a unit cell is given in Table 1.2 and each unit cell contains four formula units.

The undoped crystal is colorless and transparent from 200 to 2500 nm with a 191 nm absorption edge and estimated band gap of 6.5 eV [36]. γ-$LiAlO_2$ has the highest melting point of all three phases at $1700 \pm 20\,^{\circ}C$ [37], although lithium begins to evaporate from solid lithium aluminate at $900\,^{\circ}C$ [38].

II. Theoretical Foundation

2.1 Electron Paramagnetic Resonance (EPR)

An electron has an inherent angular momentum known as spin that is represented by the spin angular momentum operator $\hat{\mathbf{S}}$ [39]. It is analogous to the angular momentum that would be generated classically if a sphere were rotating about its central axis, however, it is not identical to any classical angular momentum because an electron is a point particle with no internal structure and spin is solely quantum mechanical in origin. The electron also has a spin-induced magnetic moment related to the spin by

$$\hat{\mu} = \gamma\hat{\mathbf{S}} = -g\frac{q}{2m_e}\hat{\mathbf{S}} \qquad [\text{J T}^{-1}], \tag{2.1}$$

where γ is the gyromagnetic ratio which relates angular momentum to magnetic moment, g is a dimensionless number known as the Zeeman splitting factor or g factor, q is the electronic charge, and m_e is the electronic mass. The negative sign in equation (2.1) implies that the direction of the magnetic moment is anti-parallel to the direction of the spin. A classical analogue to the electron magnetic moment would be the magnetic moment that arises from a current i that flows through a loop of wire in the $x-y$ plane having a radius r and area A. The loop of wire then behaves as a point magnetic dipole with a moment normal to the plane of the loop with a magnitude of iA, where $i = qv/2\pi r$ and $A = \pi r^2$. If we now think of the current as a particle with mass m and charge q moving around the loop with speed v, we then have for the magnetic moment

$$\mu_z = iA = \pm\frac{qv}{2\pi r}\pi r^2 = \pm\frac{q}{2m}mvr = \frac{q}{2m}L_z, \tag{2.2}$$

where L_z would be the orbital angular momentum of the particle about the z-axis [40]. The choice of sign depends on the direction of rotation of the particle. In equation (2.2), $g = 1$, but for the free electron in equation (2.1)

$$g_e = 2.0023. \tag{2.3}$$

The value of the g factor for an electron in a material depends on the relative contributions from the orbital angular momentum $\hat{\mathbf{L}}$ of the electron, which arises from its motion about a nucleus, and the spin $\hat{\mathbf{S}}$ of the electron, to the electron's total angular momentum [41].

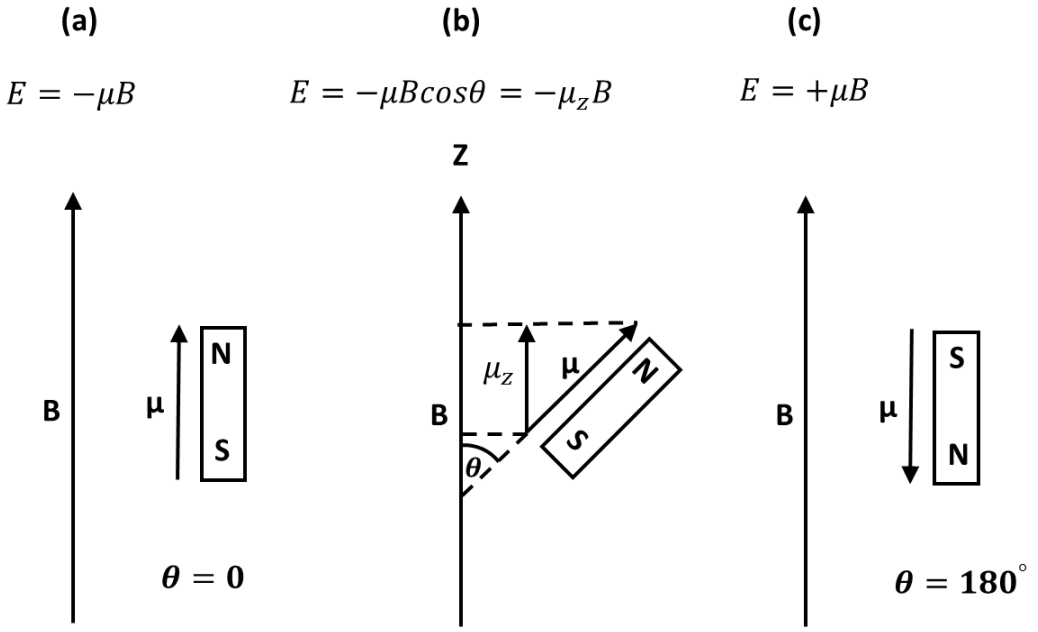

Figure 2.1. Energy of a classical magnetic dipole in a static magnetic field B as a function of the angle θ between the magnetic field and the axis of the dipole: (a) minimum energy configuration; (b) arbitrary value of θ; (c) maximum energy configuration. Adapted from [42].

The electron's magnetic moment means that the electron can be treated as a magnetic dipole when subjected to an external static magnetic field $\mathbf{B}$ as shown in

Figure 2.1. The energy of this interaction is given by

$$E = -\hat{\mu} \cdot \mathbf{B} \qquad [\mathrm{J}] \tag{2.4}$$

$$= -|\hat{\mu}| B \cos\theta \tag{2.5}$$

$$= -\hat{\mu_z} B, \tag{2.6}$$

where $\hat{\mu_z}$ is the z-axis component of $\hat{\mu}$ and $\mathbf{B}$ is along the z-axis. Substituting equation (2.1) into equation (2.4) results in

$$E = g\frac{q}{2m_\mathrm{e}}\hat{S}_z B \tag{2.7}$$

$$= g\frac{q\hbar}{2m_\mathrm{e}} m_S B \tag{2.8}$$

$$= g\mu_B m_S B, \tag{2.9}$$

where $\hat{S}_z$ represents the z-axis component of $\hat{\mathbf{S}}$ with eigenvalue $\hbar m_S$, m_S is the spin magnetic quantum number,

$$\mu_B = \frac{q\hbar}{2m_e} \tag{2.10}$$

is the Bohr magneton, and $\hbar$ is Planck's constant reduced. m_S can assume values that range from S to $-S$ in increments of one where S is the spin quantum number. S can assume any half-integer or integer value including zero. For an electron, $S = 1/2$ [43]. Unlike the classical magnetic dipole depicted in Figure 2.1 which can assume all angles with respect to $\mathbf{B}$ between 0 and 180°, the spin angular momentum and thus the magnetic moment, can only assume discrete directions with respect to $\mathbf{B}$ as shown in Figure 2.2. The magnitude squared of the spin vector in Figure 2.2 is

$$\hat{\mathbf{S}}^2 = \hbar^2 [S(S+1)] \qquad [\mathrm{J}^2 \cdot \mathrm{s}^2] \tag{2.11}$$

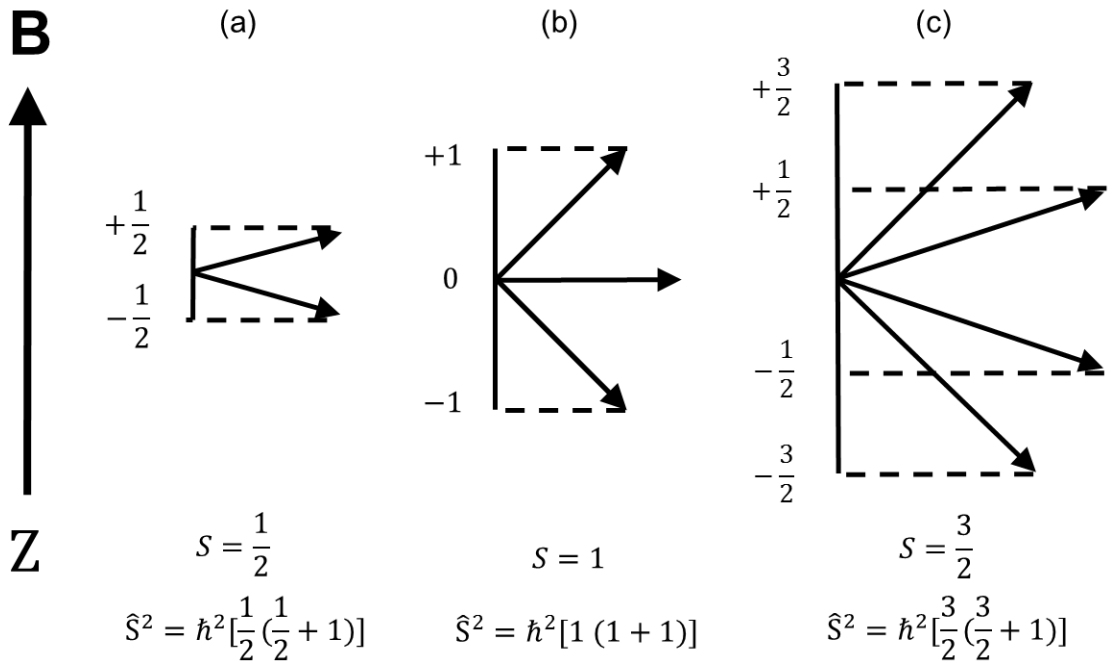

Figure 2.2. The allowed orientations of the spin angular momentum vector with respect to a static magnetic field parallel to the z-axis for (a) $S = 1/2$, (b) $S = 1$, (c) $S = 3/2$. $\hat{\mathbf{S}}^2$ is the magnitude squared of the spin vector. Adapted from [44].

and the magnetic quantum number m_S determines the magnitude of its component along the **B** field direction. The quantization of spin direction leads to the quantization of the energy levels of a quantum magnetic dipole as shown in Figure 2.3 for an $S = 1/2$ system.

In Figure 2.3, the electron can only assume an energy of

$$E = \pm g\mu_B \frac{B}{2} \tag{2.12}$$

depending on the value of m_S and the difference between the two energy levels is

$$\Delta E = g\mu_B B. \tag{2.13}$$

The energy levels in Figure 2.3 are known as electron Zeeman energy levels and

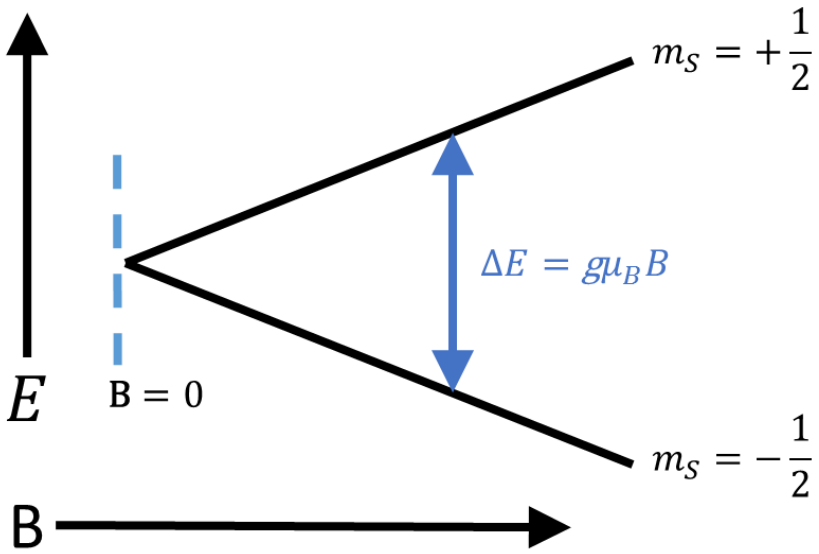

Figure 2.3. The energy levels for a single unpaired electron with $S = 1/2$ as a function of applied magnetic field B. This is sometimes referred to as the electron Zeeman energies [45].

electron paramagnetic resonance (EPR) spectroscopy arises from the fact that an oscillating electromagnetic field $\mathbf{B}_1$, can induce an unpaired electron in an external static magnetic field to transition between electron Zeeman levels if certain conditions are met. $\mathbf{B}_1$ must be perpendicular to the static magnetic field $\mathbf{B}$, and it must have an appropriate frequency ν such that the photon energy is equal to ΔE. For most EPR spectrometers including the one used in this study, microwave energies are used with $\nu \approx 9.4\,\text{GHz}$. EPR spectrometers that operate at this microwave frequency are known as "X-band" spectrometers, but other spectrometers operating at lower or higher frequencies do exist [46]. If these conditions are met then the electron can be induced to transition from $m_S = +1/2$ to $m_S = -1/2$ or vice versa. The relationship between the energy of a photon and ΔE is

$$\Delta E = h\nu = g\mu_B B, \tag{2.14}$$

where $h = 2\pi\hbar$. ΔE is called the resonance energy and equation (2.14) is known as

the resonance condition [47]. In theory, the resonance condition could be achieved in two equivalent ways. **B** could be held fixed as one varied the frequency of the incident radiation until absorption occurs, or alternatively, the frequency of the incident radiation could be held fixed while **B** is varied. Most EPR spectrometers use this latter approach because it is more difficult to vary ν, however, this also places limitations on the EPR transitions that can be measured because it is difficult to create a static magnetic field much greater than 1.3 T.

An EPR spectrometer fundamentally measures the absorption of incident electromagnetic energy by a paramagnetic sample. Figure 2.4(a) shows a representative

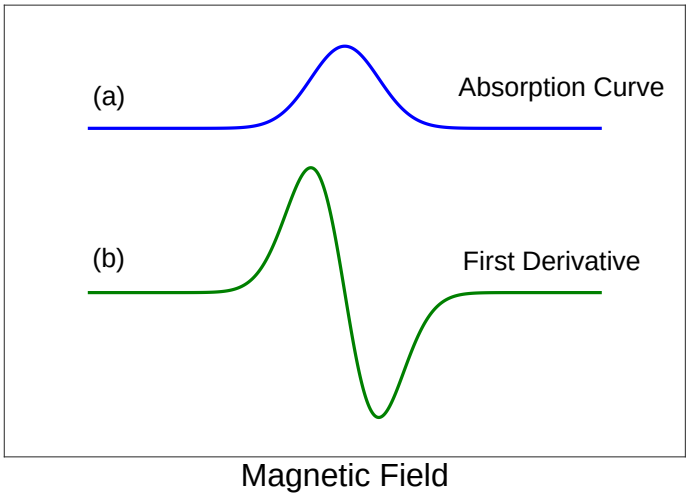

Figure 2.4. (a) A representative microwave absorption spectrum, (b) first derivative of an absorption spectrum.

example of a microwave absorption spectrum. A 100 kHz modulation of the static **B** field is employed to improve the sensitivity of the spectrometer. This results in the EPR lines appearing as the first derivatives of the absorption spectrum and is what is normally observed in the output of an EPR spectrometer as shown in Figure 2.4(b) [48]. Some paramagnetic species have more than one unpaired electron, such as the transition-metal ions, where the total spin is often greater than 1/2. In such a situation there will be more than one EPR transition, and the number of EPR

transitions or first derivatives observed by the spectrometer is $2S$.

2.2 The Spin Hamiltonian

If an electron had only the electron Zeeman interaction, all EPR spectra would look like Figure 2.4(b). In reality, there are several interactions an electron is subjected to in a crystal lattice that can change the EPR spectrum, such as splitting of the EPR lines or changes in the expected g value. The solution of the Schrödinger equation that takes into account all of the interactions between a single unpaired electron and its external environment, as well as its internal interactions from phenomena such as its spin-orbit coupling, is far too complicated to be generally applicable to EPR [49]. In order to simplify analysis of paramagnetic systems studied with EPR, the concept of the spin Hamiltonian was introduced to describe the behavior of an unpaired electron in a crystalline environment using only electron and nuclear spin operators and parameters. This is useful because these parameters can be measured using EPR without knowing the true wave function of the defect system. The spin Hamiltonian is given by

$$\mathcal{H} = \mathcal{H}_{EZ} + \mathcal{H}_{FS} + \mathcal{H}_{HF} + \mathcal{H}_{NZ} + \mathcal{H}_{Q} \quad \text{[J]} \tag{2.15}$$

$$\mathcal{H}_{EZ} = \mu_B \hat{\mathbf{S}} \cdot \mathbf{g} \cdot \mathbf{B} \quad \text{electron Zeeman interaction} \tag{2.16}$$

$$\mathcal{H}_{FS} = \hat{\mathbf{S}} \cdot \mathbf{D} \cdot \hat{\mathbf{S}} \quad \text{fine-structure interaction} \tag{2.17}$$

$$\mathcal{H}_{HF} = \hat{\mathbf{S}} \cdot \mathbf{A} \cdot \hat{\mathbf{I}} \quad \text{hyperfine interaction} \tag{2.18}$$

$$\mathcal{H}_{NZ} = g_n \mu_n \hat{\mathbf{I}} \cdot \mathbf{B} \quad \text{nuclear Zeeman interaction} \tag{2.19}$$

$$\mathcal{H}_{Q} = \hat{\mathbf{I}} \cdot \mathbf{Q} \cdot \hat{\mathbf{I}} \quad \text{nuclear quadrupole interaction} \tag{2.20}$$

where $\mathbf{D}$ is the fine structure matrix, $\mathbf{A}$ is the hyperfine matrix, $\hat{\mathbf{I}}$ is the nuclear spin operator, g_n is the nuclear g factor, μ_n is the nuclear magneton, and $\mathbf{Q}$ is the nuclear

electric quadrupole matrix. In equation (2.16), **g** is a matrix because the EPR spectra of many defects exhibit angular anisotropy in their g value. Paramagnetic defects having all three principal g values (eigenvalues) the same are known as isotropic defects.

2.2.1 Fine-Structure Interaction.

Fine-structure splitting arises for paramagnetic defects with $S > 1/2$. The fine-structure interaction comes about because of the influence of the crystal electric field on the electron spin through the spin-orbit interaction and through the magnetic dipole-dipole interaction between unpaired electrons [50]. The effects of fine-structure splitting on the energy levels of an unpaired electron with $S = 1$ are demonstrated in Figure 2.5. Figure 2.5 shows that even at zero **B** field, the energy levels are split by

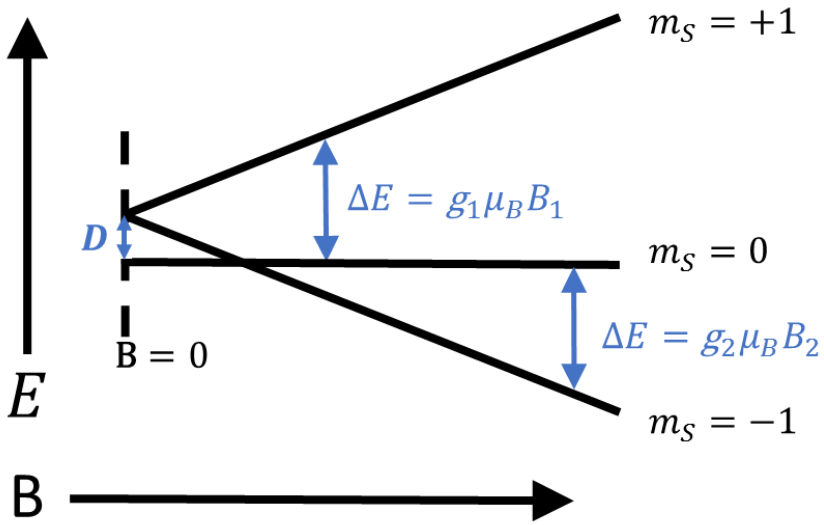

Figure 2.5. Simplified example of fine-structure splitting for a point defect with an unpaired electron with $S = 1$, isotropic g factor, D axially symmetric along its z-axis, and B along the fine structure matrix z-axis. D is the fine-structure splitting constant derived from the principal values of D. This approximation is valid to first order when $\mathcal{H}_{EZ} \gg \mathcal{H}_{FS}$.

an amount D, the fine-structure splitting constant. This effect is known as "zero-field splitting" [51].

2.2.2 Nuclear Zeeman Interaction.

Everything that has been said for the behavior of an unpaired electron in a magnetic field also applies to an unpaired nucleus with nuclear spin $I > 0$. This results in a nuclear Zeeman splitting of the nuclear energy levels in the same way as for the electron. However, the frequency associated with ΔE is on the order of MHz instead of GHz in similar magnetic fields since the magnetic moment of a nucleus is proportional to μ_n, and $\mu_n \approx \mu_B/1836$. Therefore, ΔE in equation 2.13 will be on the order of 1800 times smaller for a nucleus than for an electron.

2.2.3 Hyperfine Interaction.

The hyperfine interaction is the magnetic interaction between the magnetic moment of an unpaired electron and the magnetic moment of its central nucleus. For every Zeeman energy level an electron has in a magnetic field, the nucleus can assume any of its nuclear Zeeman levels. This results in a splitting of the electron Zeeman energy levels whenever the central nucleus has $I > 0$, as shown in Figure 2.6. In Figure 2.6, the single EPR transition that occurs when no hyperfine interaction is present has been split into three lines of equal intensity separated by a distance a_0, where a_0 is the hyperfine splitting constant. The number of hyperfine lines that are created is

$$2I + 1, \tag{2.21}$$

and the selection rules for hyperfine transitions are

$$\Delta m_S = \pm 1, \Delta m_I = 0, \tag{2.22}$$

where m_I is the nuclear magnetic quantum number. The sum of the intensities of the hyperfine-split EPR lines will equal the intensity of a single EPR transition with no

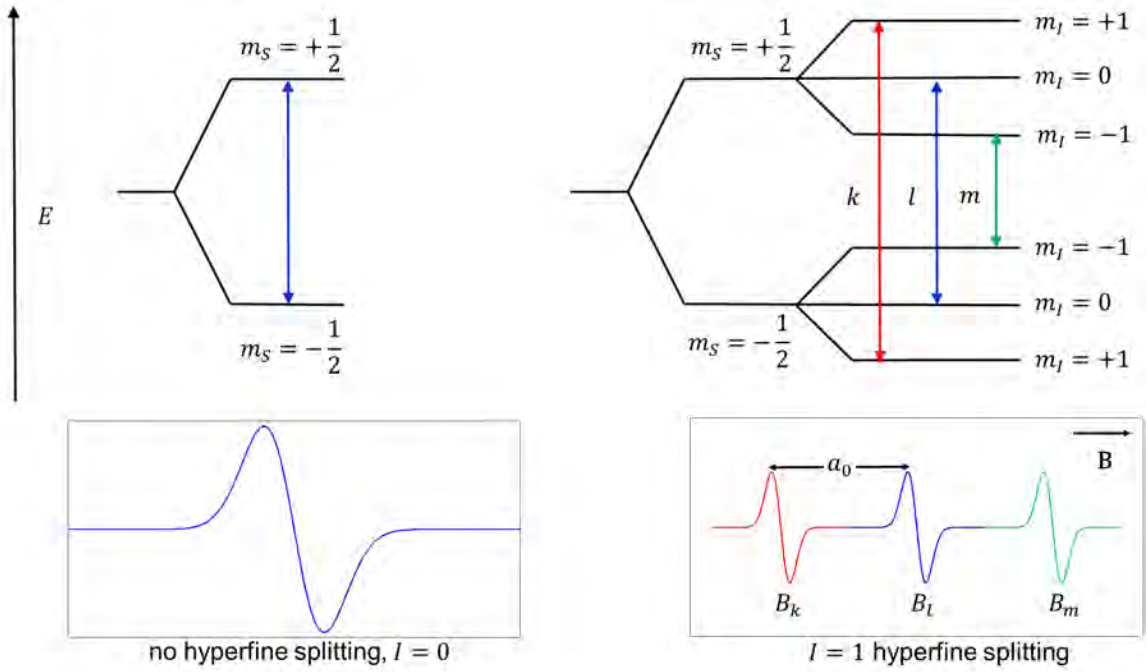

Figure 2.6. Energy level scheme of the deuterium atom with $S = 1/2$ and $I = 1$ at fixed B. a_0 is the hyperfine splitting constant and is the distance between the adjacent colored EPR transitions in magnetic field units.

hyperfine splitting.

2.2.4 Nuclear Quadrupole Interaction.

The nuclear quadrupole interaction occurs for many nuclei with $I > 1/2$ and it characterizes the electric charge distribution in the nucleus. It is generally not relevant for EPR transitions but can play a role in electron-nuclear double resonance (ENDOR) [52].

2.3 Optical Absorption

Optical absorption in this dissertation refers to the absorption of light by a solid having wavelengths between the ultraviolet and the infrared. This light absorption is caused by the transition of a bound electron from its ground state energy level to an excited state and is analogous to the microwave absorption in EPR but occurs at

significantly higher energies. The present study will be primarily concerned with three types of absorption phenomena: intracenter absorption associated with transition-metal impurities in ionic crystals, absorption due to charge-transfer processes between transition-metals and oxygen ions, and absorption caused by anion vacancies known as F^+ centers [53].

Transition-metal ions refer to those elements in the periodic table that have partially filled $3d$ shells. In the context of dopants or impurities, this will most often mean those ionized elements between scandium and zinc in row four of the periodic table, and less often those in row five. For a free ion, all of the electron $3d$ shell orbitals are degenerate, but when placed in a crystalline environment, the degeneracy of the d levels is lifted. This arises due to the fact that the positive transition-metal cation will be surrounded by negative anions in an ionic crystal that produce an electric field at the cation site, causing a perturbation of the energy levels known as the static crystal-field effect (same as the Stark effect for a free atom [54]). Figure 2.7

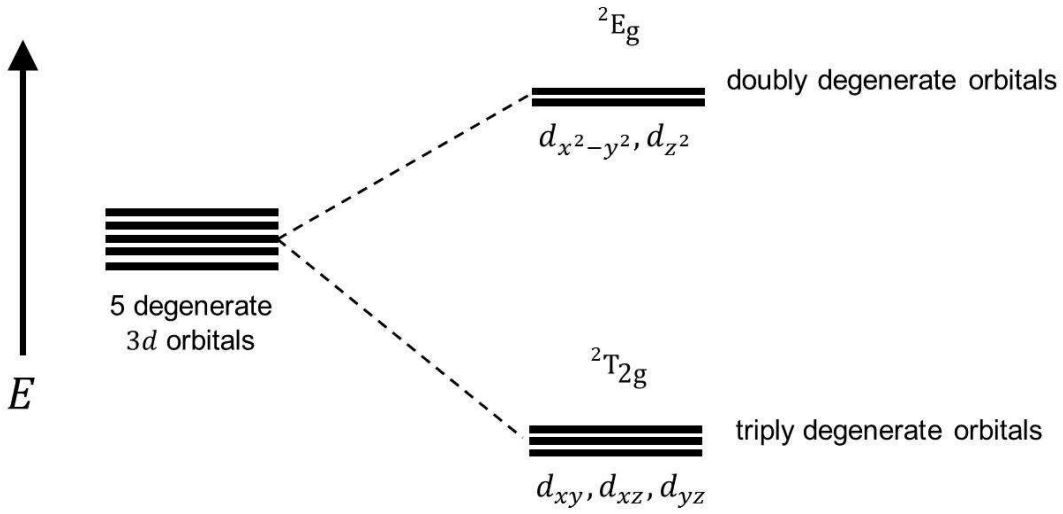

Figure 2.7. An example of the crystal-field effect for a Cu^{2+} ion in an tetrahedral environment. The five degenerate $3d$ levels of the free ion are split into a doublet state labeled ^2E_g and a triplet state labeled $^2T_{2g}$. A hole in the triplet state can absorb a photon and move to the doublet state.

shows what happens to the energy levels of Cu^{2+} which has a $3d^9$ electronic configuration, in a tetrahedral crystal environment where it is surrounded by four anions. The five degenerate $3d$ levels are now split into a triplet ground state $^2T_{2g}$, and a doublet excited state ^2E_g [55]. The superscript prefix refers to the spin multiplicity, and the letter subscript refers to the parity (g for *gerade*, the German word for even. u for *ungerade* or odd parity states). This configuration can be treated as a filled $3d$ shell with one hole [56]. The hole can move into the excited state after a photon is absorbed by the spin system. This type of transition is known as a $d \rightarrow d$ transition because the unpaired spin begins and ends in a d orbital. The energy level scheme will become more complicated if there are more unpaired d electrons or the anion coordination is changed.

There will also be an additional perturbation from the surrounding anions being displaced from their equilibrium positions, which alters the electric field experienced by the transition-metal cation. This is called the dynamic crystal-field effect and is produced by vibrations of the crystal lattice which couple to the electronic energy levels through electron-phonon interactions. Figure 2.8 depicts how the electron energy levels are affected by electron-phonon coupling. The discrete energy levels E_1 and E_2 now are comprised of a continuum of phonon modes that form vibrational bands. Each mode is separated from the previous mode by an energy $\hbar\Omega$, where Ω is the phonon angular frequency. The absorption of a photon by an electron in the ground state of E_1 moves the electron into an excited state and creates one or more phonons. Energy conservation requires that

$$\hbar\omega_a = (E_2 + n\hbar\Omega_2) - E_1 = (E_2 - E_1) + n\hbar\Omega_2, \tag{2.23}$$

where $\hbar\omega_a$ is the energy of the absorbed photon and n is an integer [58]. Equation (2.23) shows that the range of absorption energies is from $(E_2 - E_1)$ up to the

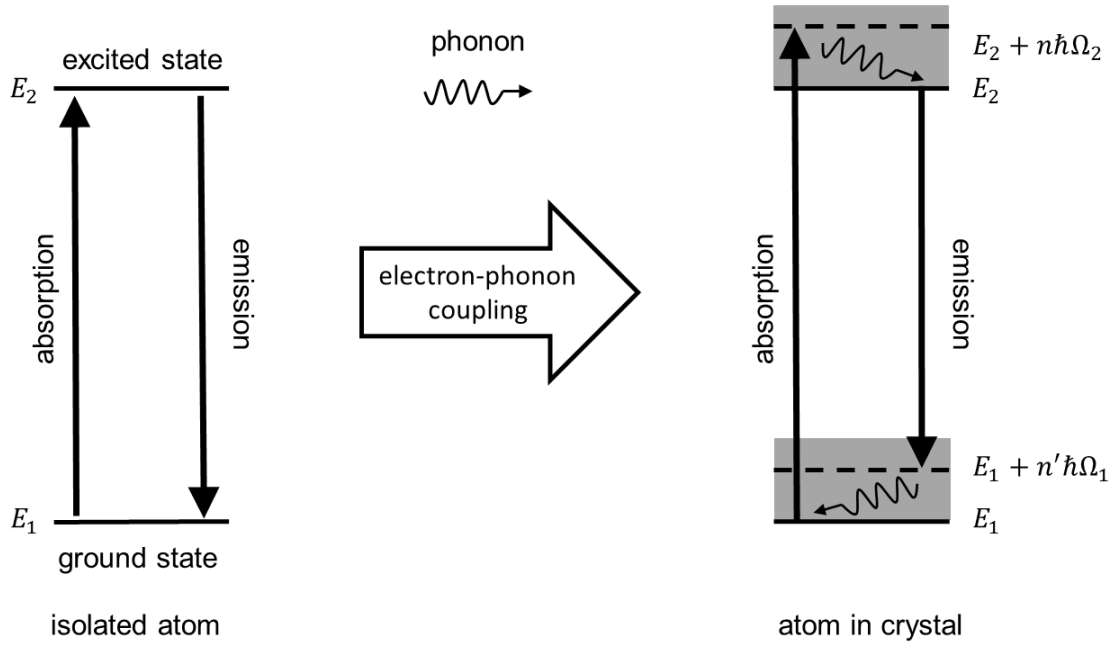

Figure 2.8. Electron-phonon coupling has the effect of turning the discrete energy levels into vibrational bands. n' and n are integers and Ω represents the phonon frequency. Adapted from [57].

maximum phonon energy allowed.

The description of the Cu^{2+} energy levels just described relied on static crystal field theory where the d orbitals were perturbed by the surrounding electric field, but did not interact with the anion orbitals. In reality, crystal field theory has been shown to be inadequate at predicting the correct energies for some measured absorption bands and has had to be modified with molecular orbital theory [59]. Molecular orbital theory predicts that the d orbitals of the transition-metal ion and the p orbitals of the oxygen ions mix and form new molecular orbitals. The formation of molecular orbitals permits an electron to move from an oxygen ion to a transition-metal ion that has excess charge for its lattice site. This is called a charge transfer transition and these transitions usually occur at greater energies and have intensities hundreds or thousands of times greater than $d \rightarrow d$ transitions [60]. The reason for this is because selection rules make $d \rightarrow d$ transitions forbidden in the free ion, but these rules are

broken when the ion is placed in a crystal field environment. The transition becomes allowed, but the probability is still low compared to the charge transfer transitions.

Anion vacancies in ionic crystals act as lattice sites deficient in negative charge that can trap one or more electrons. A neutral anion vacancy is called an F center, an anion vacancy with one unpaired electron is called an F^+ center. An electron trapped at an anion vacancy is in a bound state with energy levels characteristic of the particle in a box in the most simple model [61]. The energy levels for a trapped electron in a box with sides of length a are

$$E_{n_x n_y n_z} = \frac{\hbar^2 \pi^2}{2 m_e a^2} \left[n_x^2 + n_y^2 + n_z^2 \right] \qquad \text{[J]}, \tag{2.24}$$

where n_x, n_y, and n_z are integer only quantum numbers that specify the electronic states. All of the quantum numbers are equal to 1 for the ground state. For the first excited state, one of the quantum numbers must be equal to 2 while the others remain at 1. The lowest energy transition that corresponds to an absorption band is given by

$$E_{211} - E_{111} = \frac{3 \hbar^2 \pi^2}{2 m_e a^2}. \tag{2.25}$$

The energy levels of F^+ centers are also affected by crystal vibrations which displace neighboring ions from their equilibrium position thus altering the size of the box. This in turn alters the energy in equation (2.24) and turns the energy levels into vibronic bands just as for the transition-metal impurity. Figure 2.9 provides an example of what an absorption spectrum looks like using the F_2 center (two adjacent oxygen vacancies with four trapped electrons) in neutron-irradiated MgO.

Macroscopically, the absorption of light propagating in the z direction through a

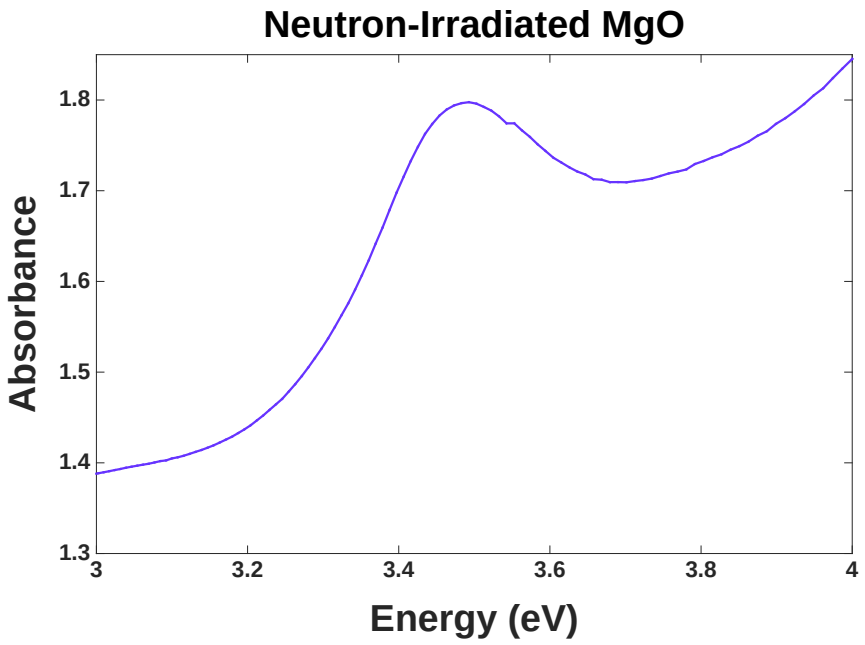

Figure 2.9. Example absorption curve from neutron-irradiated MgO. The 3.5 eV peak is due to two adjacent oxygen vacancies each with two trapped electrons, known as a neutral divacancy or F_2 center [62]. This spectrum was obtained at AFIT using a MgO crystal neutron irradiated in 1968.

medium is expressed in the form of Beer's Law as

$$I(z) = I_0 e^{-\alpha z} \qquad [\text{W m}^{-2}], \tag{2.26}$$

where $I(z)$ is the intensity of light at position z, I_0 is the incident intensity at $z = 0$, and α is the absorption coefficient [63]. The absorption coefficient is directly proportional to the concentration of absorbing species, so Beer's Law says that the fraction of power absorbed in a unit length of a sample is directly proportional to the concentration of absorbing species.

2.4 Thermoluminescence (TL)

The basic mechanisms behind thermoluminescence (TL) are similar to scintillation in that luminescence occurs from electron-hole recombination. Scintillation specifi-

cally refers to light emission that happens instantaneously upon excitation, which is also defined as fluorescence. In thermoluminescence, light emission occurs only upon heating the irradiated material above the irradiation temperature [64, 65]. Heating is required because the electrons and holes are trapped at energy levels within the band gap and require a sufficient thermal energy before they can be released from the energy level trap. These energy levels that trap electrons and holes can be the activator levels introduced by impurities, but they can also be energy levels from other types of point defects. Different types of point defects will create electron or hole traps that will have energy levels specific to the defect, and the traps can maintain trapped charge for times ranging from days to years when held below the critical release temperature. A simplified energy level scheme that depicts the basic processes in thermoluminescence is shown in Figure 2.10.

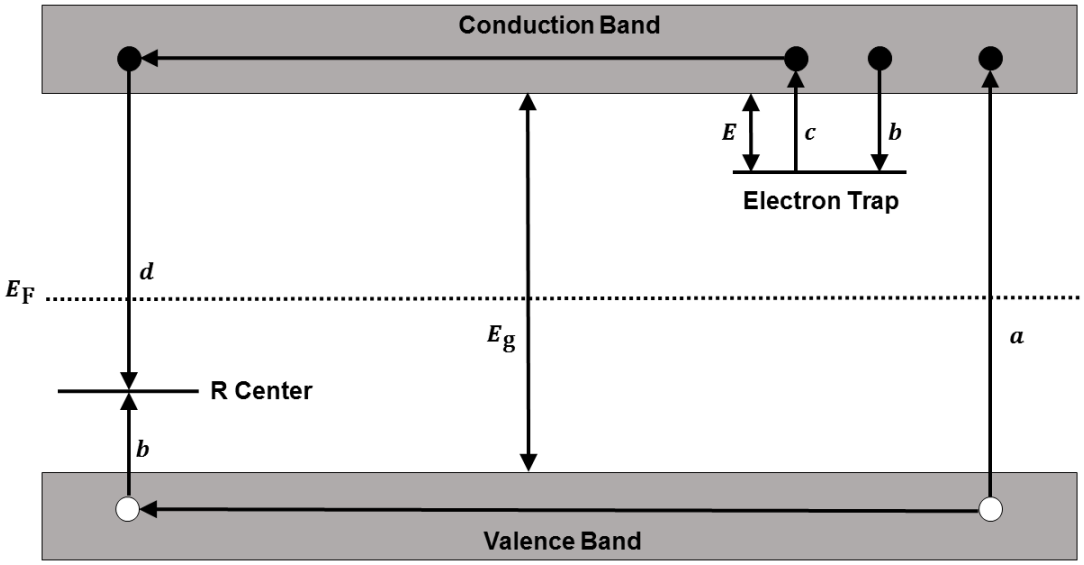

Figure 2.10. Simplified one trap-one recombination energy band model showing the electronic transitions in a TL material. (a) Electron-hole generation, (b) electron and hole trapping, (c) release of trapped electrons by heating, (d) and recombination. Solid circles are electrons and open circles are holes. R is for recombination, E_g is the band gap energy, E is the depth of the trap, and E_F is the Fermi level. Adapted from [66].

For simplicity, Figure 2.10 only assumes one electron trap and one recombination center (hole trap). The electron trap is situated near the bottom of the conduction

band and the recombination center is near the top of the valence band. E_{F} represents the Fermi level and E the energy required to free an electron from the trap, known as the trap depth or activation energy. When the TL material is subject to ionizing radiation, represented as transition a in the figure, an electron is excited into the conduction band leaving behind a hole in the valence band. The electrons and holes will move through their respective bands until they become trapped at their respective trapping sites, represented by transition b. The F^+ center is an example of an electron trap [67], and a cation vacancy would be a hole trap [68].

The trapped electrons and holes will remain at their trap locations until they have enough energy to leave the traps. The probability p, per unit time, that a trapped charge will escape the trap is given by the Arrhenius equation [65]

$$p = s \cdot \exp\left(-\frac{E}{k_B T}\right) \qquad [\mathrm{s}^{-1}], \tag{2.27}$$

where E is the activation energy in eV, k_B is Boltzmann's constant, T is the temperature, and s is the frequency factor in s^{-1}, which describes the number of "hits" against the potential wall the electron makes per second in trying to escape. If $E/k_B \gg T_0$, where T_0 is the temperature at irradiation, then electrons and holes will remain trapped for a long time after irradiation has ceased. Charges trapped in this manner can remain trapped for years, and is the reason why electron and hole traps are frequently referred to as metastable states.

Now if the TL material is subjected to increasing temperature, T will eventually approach and then exceed E/k_B, supplying enough energy to the trapped electrons to overcome the energy barrier of the traps, as shown in transition c. The released electron will migrate through the conduction band until it it recombines with a hole at the recombination site shown with transition d. In this simple model, the recombination center is a luminescent center in an excited state, which then emits light as it

returns to the ground state. The number of traps released by increasing temperature is directly proportional to the amount of light emitted from recombination, therefore the emitted light provides a direct measurement of the amount of radiation dose. If the intensity of the emitted light is plotted against temperature, a plot known as a glow curve will be produced as shown in Figure 2.11.

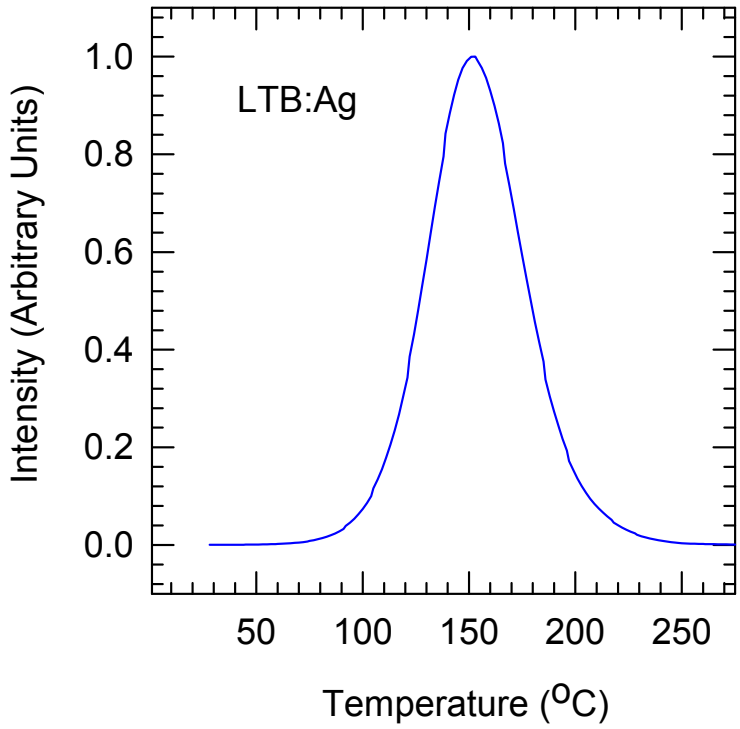

Figure 2.11. Example glow curve from silver-doped lithium tetraborate ($Li_2B_4O_7$) that has been irradiated with x-rays.

It may seem from Figure 2.11 that the temperature where the TL peak occurs, T_m, is related to the activation energy by

$$T_m = E/k_{\mathrm{B}} \tag{2.28}$$

but this is not the case! Equation 2.27 is a simplified model that ignores other important processes occurring at the same time. The electron can be retrapped again

before recombination, there can be more than one electron trap or hole trap at different depths within the band gap, or the electron can radiatively or non-radiatively recombine in the valence band. Figure 2.10 shows electrons being released and recombining at the hole trap, but recombination can also occur from released holes recombining at trapped electron sites. Finally, the position of T_m depends on the heating rate β at which the TL peak is obtained and s [69]. All of these factors combine to give complex relationships between β, T_m, E and s and are important to remember when attempting to interpret thermoluminescence glow curves.

2.5 Optically Stimulated Luminescence (OSL)

OSL dosimetry is very closely related to thermoluminescence dosimetry. OSL relies on similar types of ionizing radiation, trapping, and radiative recombination processes that are involved in TL . The materials involved are wide-band-gap, crystalline insulators that have had appropriate defect energy levels introduced into the band gap by impurities. For both OSL and TL materials, electrons and holes become trapped at defect sites through ionizing radiation where they can be stable for years [70]. The same electron-hole recombination scheme depicted in Figure 2.10 applies to both TL and OSL. The difference between TL and OSL is in how the trapped charge is stimulated to recombine. For thermoluminescence, the material is heated in order to stimulate recombination, for OSL, excitation light is used. In Figure 2.10, transition c would now be due to OSL stimulation light instead of heat. It is important to point out, however, that materials optimal for TL may not be the same materials optimal for OSL. For example, LiF:Mg,Ti thermoluminescent dosimeters can detect radiation doses on the order of μGy but the minimum measurable dose for observation of OSL in LiF:Mg,Ti has been found to be on the order of 1 Gy [71]. This would seem to indicate, but remains unclear, that the same defect centers are

not involved in both processes for any one material [72].

For OSL, the key parameter is the rate of optical stimulation given by

$$p = \sigma\phi \qquad [\mathrm{s}^{-1}], \tag{2.29}$$

where σ is the photoionization cross section (in cm^2) for the trapping centers and ϕ is the intensity of the stimulating light (in $\frac{\mathrm{photons}}{\mathrm{cm}^2\mathrm{s}}$). OSL is generally produced using a constant stimulation intensity. The resulting signal is referred to as continuous-wave-OSL or CW-OSL, and it takes the form of an exponential-like luminescence decay curve. Assuming the ideal case of one trapping center and one luminescent center, the decay curve is best represented as

$$I = I_0 \cdot \exp\left(-pt\right) \qquad [\mathrm{W\ m}^{-2}], \tag{2.30}$$

where I is the OSL intensity and I_0 is the initial intensity at time $t = 0$. The time scale over which the OSL signal decays as charge traps are continuously emptied depends on both the material and the exciting light intensity. In most materials there will be multiple trapping and luminescent centers which usually results in non-exponential decay.

Some OSL processes don't involve ionization of the trapped charge as shown in Figure 2.10, but rather excitation of the trapped charge to a higher energy state within the trap. The excited electron then falls back to the ground state of the trap and emits OSL light. This procedure has the added advantage over TL in that multiple readings of the dose could be carried out [72]. The fact that the dose information is read using optical techniques instead of heating the material is in itself an advantage because it is generally less destructive to the luminescent material.

III. Instrumentation

3.1 The EPR Spectrometer: An Overview

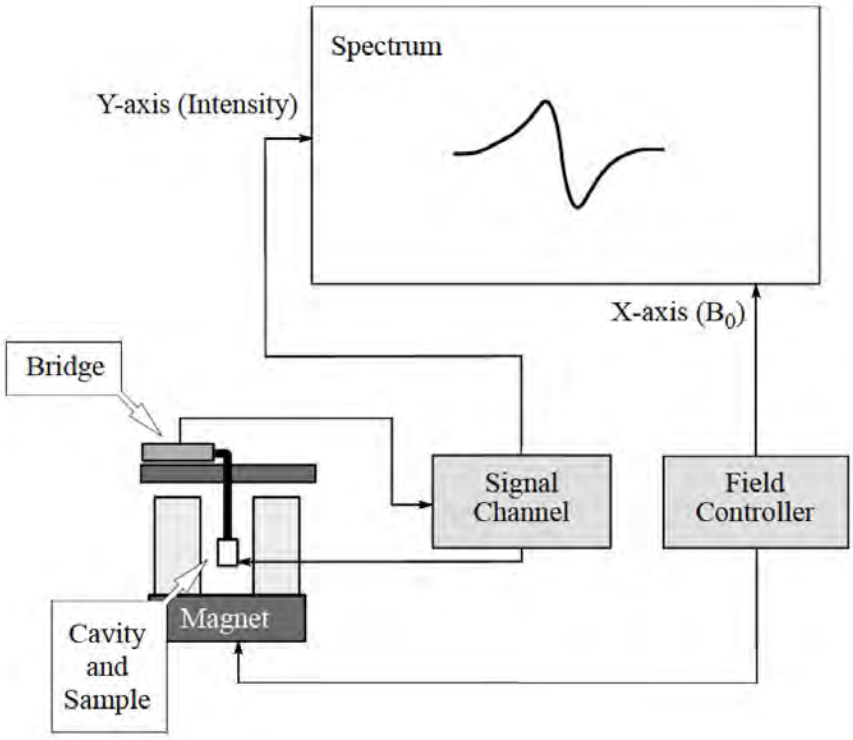

Figure 3.1. Block diagram of an EPR spectrometer. Reprinted with permission from [73].

Figure 3.1 shows a generalized block diagram of an EPR spectrometer. Any EPR spectrometer at the most basic level consists of a source of electromagnetic radiation, a chamber for holding the sample, a static magnetic field, and a detector. In Figure 3.1, the microwave bridge is the radiation source, the sample sits in a cavity called a resonator, the block labeled "Signal Channel" contains electronics that enhance the sensitivity of the spectrometer through a technique known as phase sensitive detection, and the block labeled "Field Controller" controls the magnetic field. A Bruker EMX EPR spectrometer was used in this dissertation. The function of each major component is explained below.

3.1.1 Microwave Bridge.

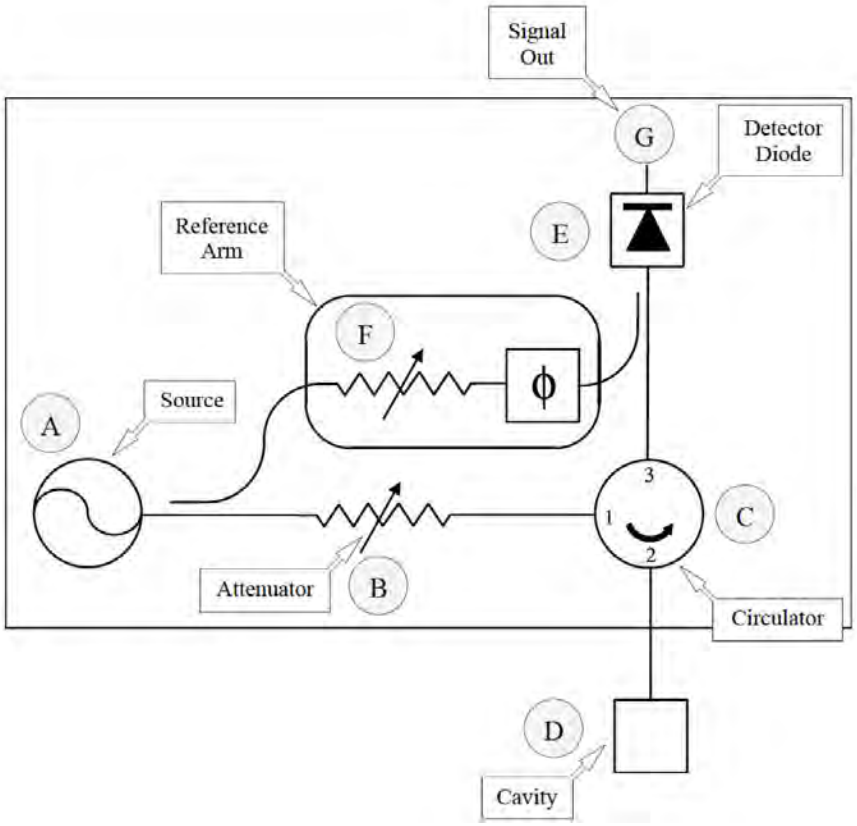

Figure 3.2. Block diagram of a microwave bridge. Reprinted with permission from [73].

Figure 3.2 depicts a simplified block diagram of the microwave bridge. Point A is the source, which generates the microwave electromagnetic radiation. The microwave source is normally a Gunn diode [74, 75]. As the microwave energy leaves the source and is directed to the cavity, it first passes through an attenuator at point B, which allows precise and accurate control of the microwave power that is incident on the sample by absorbing a portion of the microwave radiation. After passing through point B the microwave radiation enters the circulator at point C. The circulator allows the microwave energy to enter through port 1, travel towards the sample cavity through port 2, and then directs the reflected microwave energy from the sample to travel out through port 3 towards the detector instead of traveling back towards the

attenuator and the source. A portion of the microwave power also travels through the reference arm at point F as it leaves the source and ultimately combines with the reflected microwave energy from the sample cavity. The microwave energy through the reference arm serves as a bias on the detector diode, which is why it passes through an attenuator that allows the microwave power to be varied. There is also a phase shifter in the reference arm which ensures the reference microwaves and the reflected microwaves are in phase when they recombine. The most common detector is a Schottky barrier diode [76] operating in the linear region that converts the microwave power to an electrical current that will result in an EPR spectrum after processing in the signal channel.

3.1.2 EPR Cavity.

The EPR cavity is a metal box, usually rectangular but sometimes cylindrical, that has appropriate dimensions such that microwaves will resonate when they enter the cavity. This means that the microwaves will form standing waves within the cavity when critically coupled and no microwaves will be reflected back, but will remain inside the cavity. For the rectangular cavity, the dimensions are on the order of one-half the wavelength of the microwaves. The resonant frequency is the unique size-dependent frequency that allows the microwaves to resonate within a given cavity. A measure of the effectiveness of resonant cavities is given by their Q factor, or quality factor, which characterizes how efficiently the cavity stores microwave energy. The Q factor is defined as the energy stored divided by the energy dissipated per microwave period and is usually expressed as

$$Q = \frac{\nu_{\text{res}}}{\Delta\nu}, \tag{3.1}$$

where ν_{res} is the resonant frequency and $\Delta\nu$ is the full width at half max of the resonance power.

Standing electromagnetic waves have their electric and magnetic field components exactly out of phase, so the electric field is at a maximum when the magnetic field is at a minimum and vice versa. Figure 3.3 depicts an example of the standing

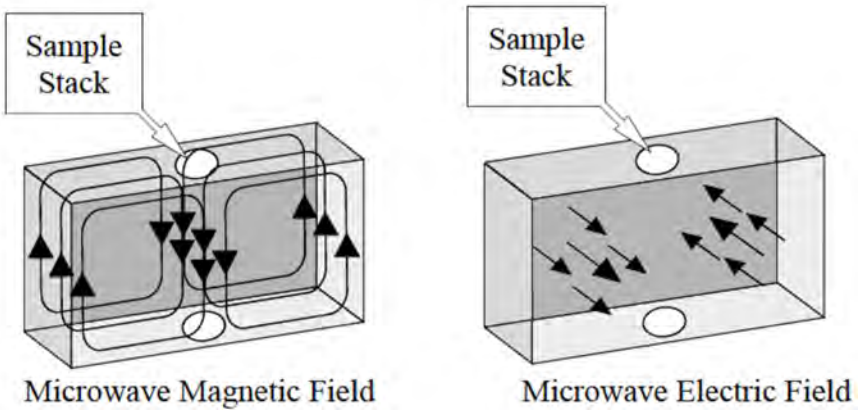

Figure 3.3. The magnetic and electric field patterns in a standard rectangular EPR cavity. Reprinted with permission from [73].

wave patterns for a rectangular cavity. As shown in the figure, the sample stack, which holds the sample, is positioned at maximum magnetic field and minimum electric field. This positioning serves two purposes; the non-resonant absorption of the microwaves caused by the electric field which degrades Q will be minimized, and the EPR absorption that is driven by the microwave magnetic field $\mathbf{B}_1$ will be maximized. EPR cavities with this optimum sample positioning provide the largest EPR signals and the highest sensitivities.

The microwaves travel towards the cavity through a metal waveguide designed to minimizes losses through its walls. The microwaves in the waveguide are then impedance matched to the cavity via a hole called an iris as depicted in Figure 3.4. The size of the iris controls the amount of microwaves reflected back and allowed to enter the cavity. This is done by means of a metal-tipped Teflon screw called an iris screw, and when no microwaves are reflected back, the microwaves in the

waveguide and the cavity are considered to be "critically coupled". The cavities are designed such that the electromagnetic wave magnetic field $\mathbf{B}_1$ is perpendicular to the external magnetic field $\mathbf{B}$. It is the field $\mathbf{B}_1$, oscillating at ν_{res}, which induces the EPR transitions between the Zeeman energy levels. When the sample absorbs the microwave energy, the Q is lowered due to increased losses and the waveguide and cavity are no longer impedance matched. The loss of critical coupling means that microwaves will be reflected back along the waveguide towards the microwave bridge and into the detector giving rise to an EPR signal.

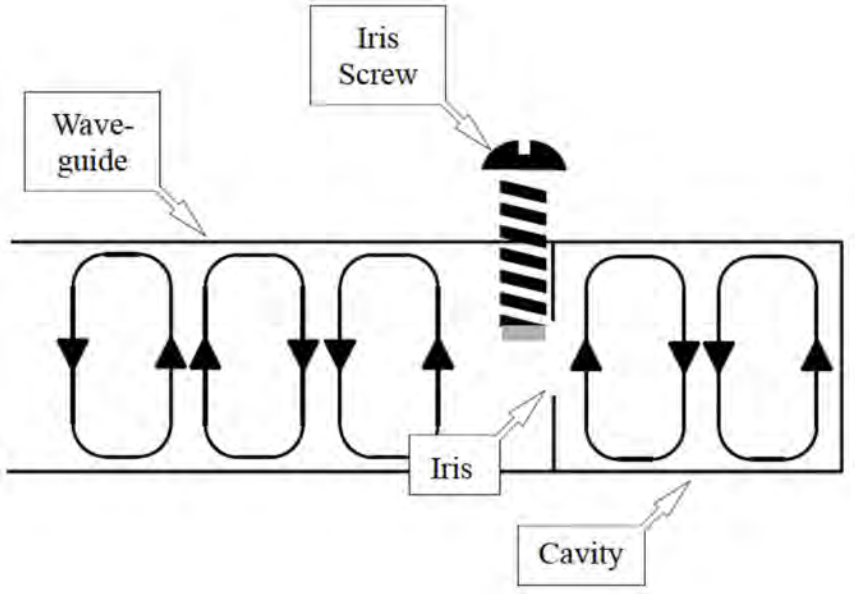

Figure 3.4. The microwaves in the waveguide and the cavity are impedance matched to eliminate reflections. This process is referred to as "critically coupling". Reprinted with permission from [73].

3.1.3 Signal Channel.

The signal channel contains electronics for enhancing the sensitivity of the spectrometer. The usual technique is to employ a lock-in amplifier, also known as a phase sensitive detector. This provides the advantages of eliminating most of the noise contributing components and amplifying the EPR signal. A 100 kHz small amplitude

modulation of the static magnetic field ($\mathbf{B}_{\text{mod}}$) is superimposed over $\mathbf{B}$. This field modulation sweeps through part of the absorption signal and the microwaves reflected from the cavity are amplitude modulated at the same frequency. The absorption signal will be transformed into a sine wave with an amplitude proportional to the slope of the absorption signal, if the absorption signal is approximately linear through the modulation amplitude range. The phase sensitive detector has a reference signal with the same frequency and phase as the modulation field. It combines the reference signal and the EPR signal and creates a DC current proportional to the amplitude of the modulated EPR signal. Any signals with different frequencies and phases will be eliminated from the DC current. Since the output polarity of the modulated EPR signal from the phase-sensitive detector is proportional to the slope of the absorption signal, the modulated EPR signal appears as the first derivative of the absorption signal. This is shown in Figure 3.5.

The modulation field is produced by a pair of Helmholtz coils embedded in the walls of the microwave cavity. The choice of 100 kHz for the modulation frequency is the result of a tradeoff between minimizing the "$1/f$ noise" at the detector diode, and maximizing the penetration of the modulation field through the inter-wall of the cavity (i.e., the skin-depth problem) [78]. Thus, this modulation field is critical in eliminating noise in the spectra, and enhancing the EPR signal through application of lock-in amplifier techniques.

For the EPR spectrometer used in this dissertation the minimum number of unpaired spins that can be detected at 10 K is approximately $5 \times 10^{10}\,\text{cm}^{-3}$. Using this as a sensitivity reference, the concentration of unpaired spins in a sample can be estimated from the EPR signal using [79]

$$\left(5 \times 10^{10}\right) (\Delta B)^2 \left(\frac{S}{N}\right) (L) \left(\frac{T}{10}\right) \left(V^{-1}\right) \qquad [\text{cm}^{-3}], \tag{3.2}$$

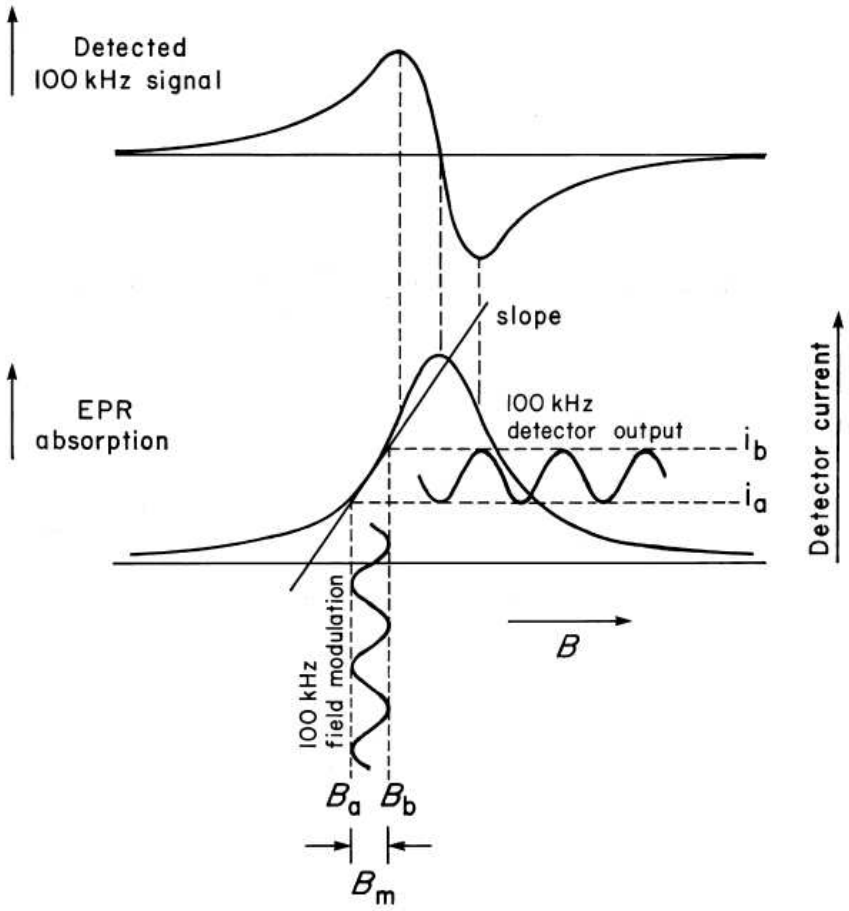

Figure 3.5. Effect of small-amplitude 100 KHz field modulation on the detector output current. The static external magnetic field B is modulated between the limits B_a and B_b while the detector current will vary between i_a and i_b. Reprinted with permission from [77].

where ΔB is the horizontal line-width in Gauss between the maximum and minimum peak of the first derivative in the EPR spectrum, (S/N) is the signal to noise ratio, L is the number of hyperfine lines, T is the temperature in Kelvin, and V is the sample volume in cm^{-3}.

3.2 Spectrophotometer

Figure 3.6 shows a simplified block diagram of the spectrophotometer used to make optical absorption measurements in this dissertation. In order to measure the

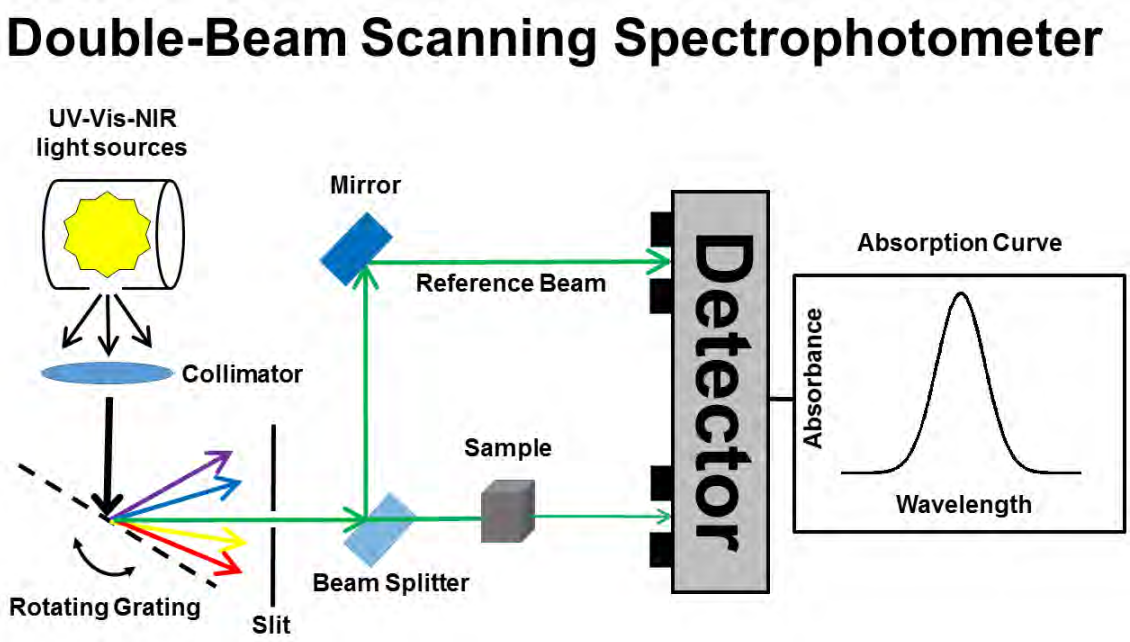

Figure 3.6. Block diagram of a double beam scanning spectrophotometer. The diagram shows the basic principles of the Cary 5000 UV-VIS-NIR spectrophotometer used in this dissertation.

absorption of light from the ultraviolet (UV), through the visible (VIS), and to the near infrared (NIR), more than one light source is needed. For the UV light source, typically a deuterium (D_2) arc lamp is used because it emits a continuous spectrum of wavelengths from 180 to 400 nm [80]. For wavelengths from about 350 nm to the NIR, an incandescent light source such as a tungsten-halogen lamp is commonly used. Since the light rays from the source are spherically diverging when emitted, a collimator is used to create parallel rays. When the parallel light rays strike the diffraction grating, light rays with different wavelengths will reflect from the diffraction grating at different angles. As shown in Figure 3.6, a beam of light is split into the various wavelengths of visible light after striking the grating, but only one beam of light representing one wavelength is allowed to pass through the slit. The grating can rotate which allows each wavelength of light to be projected through the slit. By rotating the diffraction grating and changing the light source, all wavelengths from

the UV to the NIR can be passed through the slit. This process is normally referred to as "scanning" and for the Cary-5000 unit used in this dissertation, the scanning range is from $175 - 3300\,\text{nm}$

Once the single wavelength beam passes through the slit, it is incident on a beam splitter, which splits the beam into a reflected reference beam and an un-reflected sample beam. After passing through the sample, the sample beam is attenuated due to the absorption of light by the sample, while the reference beam remains unattenuated. The sample beam and the reference beam are measured by a detector and converted into an electrical signal. Absorption is quantified in terms of the absorbance, or optical density, defined as [81]

$$\text{O.D.} = -\log_{10}\left(\frac{I(z)}{I_0}\right), \tag{3.3}$$

where $I(z)$ is the intensity of the sample beam after being attenuated by the sample, and I_0 is the intensity of light before passing through the sample, or the intensity of the reference beam. The optical density is related to the absorption coefficient from equation (2.26) by

$$\text{O.D.} = -\log_{10}\left(e^{-\alpha z}\right) = 0.434\alpha z. \tag{3.4}$$

3.3 Thermoluminescence Dosimeter Reader

Figure 3.7 displays a block diagram of the type of instrument used to measure thermoluminescence. The sample rests on a resistive heating element connected to a power supply. When the sample is heated, light emitted from the sample is directed into the photomultiplier tube (PMT). Light that enters the PMT creates electrons at the photocathode, which then leave the photocathode and are accelerated and multiplied across the dynodes, collected at the anode, and then converted into a

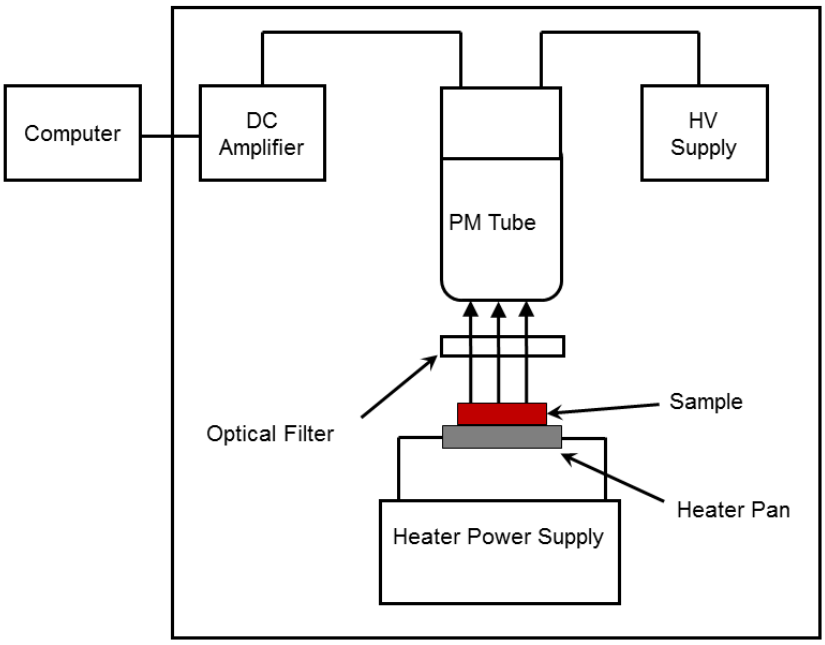

Figure 3.7. Block diagram of a thermoluminescence dosimeter reader. A Harshaw 3500 TLD Reader was used to measure thermoluminescence in this dissertation.

current [82]. This current is amplified and then measured. The measured current will be proportional to the amount of light emitted by the sample which in turn is proportional to the amount of radiation absorbed by the sample. Although a PMT can be operated with either a positive or negative high-voltage, a negative high-voltage at the cathode with the anode grounded has the advantage that generated signals can be directly sent to low-voltage measuring electronics. The PMT is housed in an enclosure that shields it from ambient light as this can cause damage to the PMT through over-excitation of the photocathode. An optical filter is also placed between the PMT and the sample to reduce the intensity of incident light on the PMT.

3.4 Spectrofluorometer

Figure 3.8 depicts a simplified block diagram of a fluorescence spectrometer, known as a spectrofluorometer. This device is used to find the excitation and emission wavelengths for a material. Electrons absorb photons and are excited into the conduction band or an excited state as discussed in Sections 1.1 and 2.3, through the process of optical excitation. Electrons recombine with holes and emit light through the process of optical emission. For a spectrofluorometer, the excitation light is generated by a xenon lamp that emits a continuous range of light from the ultraviolet to the near-infrared. The xenon lamp is used because it is more efficient than the tungsten-halogen lamp in the Cary-5000 at emitting intense UV light, which isn't necessary for absorption measurements but required to observe luminescence in some materials. The light enters the excitation monochromator, which operates in a manner similar to the diffraction grating discussed in Section 3.2, selecting single wavelengths of light from the spectrum. In this manner the spectrofluorometer can scan an entire range of wavelengths similarly to the optical absorption spectrophotometer, however, the Fluorolog-3 spectrofluorometer used in this dissertation can only scan from $200 - 800\,\text{nm}$ because of limitations imposed by the PMT.

When excitation light of the appropriate wavelength interacts with the sample, the sample will begin to fluoresce, emitting light from the excited electrons de-exciting to the ground state. The light emitted from the sample will enter the emission monochromator, which can allow single wavelengths of light to pass through and enter the photomultiplier tube. The output from the spectrofluorometer is intensity or PMT counts per second versus wavelength.

The Fluorolog has three modes that were used in this dissertation. The first mode is the emission scanning mode, where the excitation light is fixed at one wavelength and the emission monochromator can scan anywhere in the $200 - 800\,\text{nm}$ range. If a

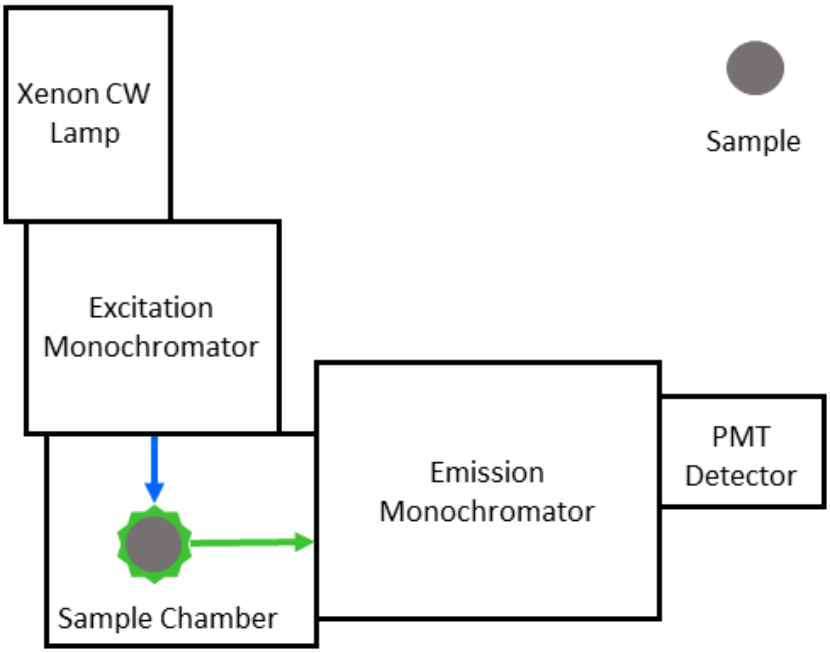

Figure 3.8. Block diagram of a fluorescence spectrometer. A Fluorolog-3 by Horiba Scientific was used to measure excitation and emission in this dissertation.

sample has emission in this range, then the measured intensity will start to increase, reach a peak, and then decrease as the monochromator moves through the emission wavelength range. The resulting intensity versus wavelength plot is known as an emission or photoluminescence (PL) peak. The excitation mode does the inverse of the emission mode, the emission monochromator is held at a fixed monitoring wavelength, and the excitation monochromator is scanned anywhere in the $200-800$ nm range. As the excitation monochromator approaches the ideal wavelength that induces electrons in a sample to excite to higher levels and emit light at the monitored wavelength, the emission intensity will begin to increase. The emission intensity will reach a plateau as the ideal excitation wavelength is reached, and then start to decrease as the excitation monochromator passes through the ideal excitation wavelength. The resulting intensity versus wavelength plot is a photoluminescence excitation (PLE) peak. The third mode used to obtain data is the kinetics mode, where the excitation and emission monochromators are held at fixed wavelengths, and the emission is

monitored as a function of time. Emission can be time dependent if the excitation light causes charge-trapping defects to release their charges over time. In that situation, the emission light would start off at its most intense, and then become weaker with time. This mode is how OSL was measured in this dissertation.

IV. Characterization of the Intrinsic Hole Center in $LiAlO_2$

4.1 Introduction

When developing a material for radiation-detector applications, it is important to identify all of the primary intrinsic and extrinsic point defects that may be present. In $LiAlO_2$, and also in other light-emitting materials, point defects may serve as transient or long-lived electron and hole traps and have a major effect on any device performance. Some defects may provide efficient radiative recombination pathways that enhance emission, a desirable outcome, while other defects may introduce non-radiative recombination pathways that limit the amount of emitted light. The thermal stability of these electrically and optically active traps are also important for device operation. Electron paramagnetic resonance, optical absorption, and luminescence experiments are often combined to provide a comprehensive approach to identification and characterization of point defects in non-metallic crystals.

In this chapter, an optical and magnetic resonance study of the effects of ionizing radiation on commercially available single crystals of $LiAlO_2$ is described. An intense 11-line EPR spectrum is created when a crystal is irradiated at room temperature with x rays. Auvray-Gely *et al.* first reported this $S = 1/2$ spectrum with multiple hyperfine lines in 1988, but the responsible defect was not identified at the time [24]. This EPR spectrum was produced in recently grown $LiAlO_2$ samples and is identified for the first time as a hole trapped at an oxygen ion adjacent to a lithium vacancy. In general, a trapped-hole defect of this type is an example of an acceptor-bound small polaron in an oxide crystal [83]. Correlation of the thermoluminescence glow curve with an anneal of the EPR signal reveals that the trapped holes become thermally unstable at 105 °C, are released and migrate to the trapped electrons where radiative recombination occurs.

4.2 Electron Paramagnetic Resonance Results

For this study, undoped lithium aluminate samples obtained from the MTI Corporation in Richmond, CA were used [84]. They were grown by the Czochralski technique. Several samples were purchased as 10 mm × 10 mm × 0.5 mm substrates, that had either c or a-plate orientations, and were subsequently cut into EPR sized samples. An as-grown $LiAlO_2$ crystal has essentially no paramagnetic defects. At approximately 5 K some very weak EPR signals became visible close to the free electron g value that are most likely due to impurities. These signals were not further investigated. After irradiating a sample with x rays generated with 60 kV and 30 mA for 1 minute, an EPR spectrum was obtained with the **B** field parallel to the [001] direction (parallel to the c-axis) that contained eleven equally spaced hyperfine lines separated by 0.87 mT, with average linewidths of 0.41 mT and centered around 332 mT, as shown in Figure 4.1. The number of spins represented by the spectrum in Figure 4.1 was estimated to be $4.3 \times 10^{17}\,\mathrm{cm}^{-3}$ from equation (3.2), where the S used is the intensity of one of the outermost lines, and $L = 36$. The number 36 comes from the fact that the relative intensity of the lines are represented by the sequence 1:2:3:4:5:6:5:4:3:2:1, with 36 being the sum of the relative intensities. Since there are eleven hyperfine lines in Figure 4.1, this indicates from equation (2.21) the hyperfine pattern is from either an $I = 5$ nucleus or nuclei that effectively act as an $I = 5$ nuclei. The 1:2:3:4:5:6:5:4:3:2:1 intensity ratios of the hyperfine lines, shown by the upper red stick diagram in Figure 4.1, indicate the spectrum is the result of two equivalent $I = 5/2$ nuclei. If the hyperfine pattern were caused by a single $I = 5$ nucleus, the spectrum would have 11 lines of equal intensity as the example in Figure 2.6(b) illustrates for an $I = 1$ nucleus.

There are only two $I = 5/2$ nuclei in $LiAlO_2$ in sufficient quantity that could create the 11-line spectrum; ^{27}Al and ^{17}O. ^{17}O is 2600 times less abundant than ^{16}O,

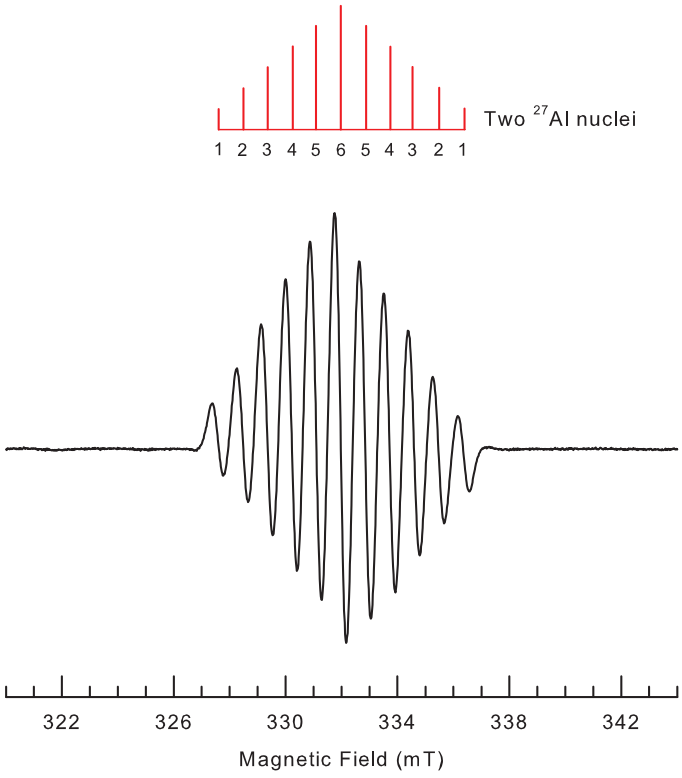

Figure 4.1. Eleven line hyperfine spectrum of $LiAlO_2$ after irradiation with x rays with B parallel to [001]. The frequency is 9.401 GHz and the temperature is 30 K. This pattern is obtained from an unpaired electron having an interaction with two equivalent ^{27}Al nuclei. The red stick figure represents the ratio of the peak intensities.

the isotope that comprises 99% of natural oxygen. Since ^{16}O is an $I = 0$ nucleus, this means that if the 11-line spectrum were caused by ^{17}O, there would be a single EPR line from the electron interacting with ^{16}O that would be superimposed over the 11-line spectrum and 2600 times more intense. Since this is not observed, the only conclusion left is that the eleven line spectrum in Figure 4.1 is generated by an electron interacting with two equivalent ^{27}Al ions.

Figure 4.2 shows the EPR spectra for the magnetic field along the [110] and [100] directions. Two sets of EPR signals can clearly be resolved for each direction of the crystal. The fact that there are two 11-line EPR signals for these directions is in keeping with the tetragonal crystal symmetry. This can be understood as follows: if

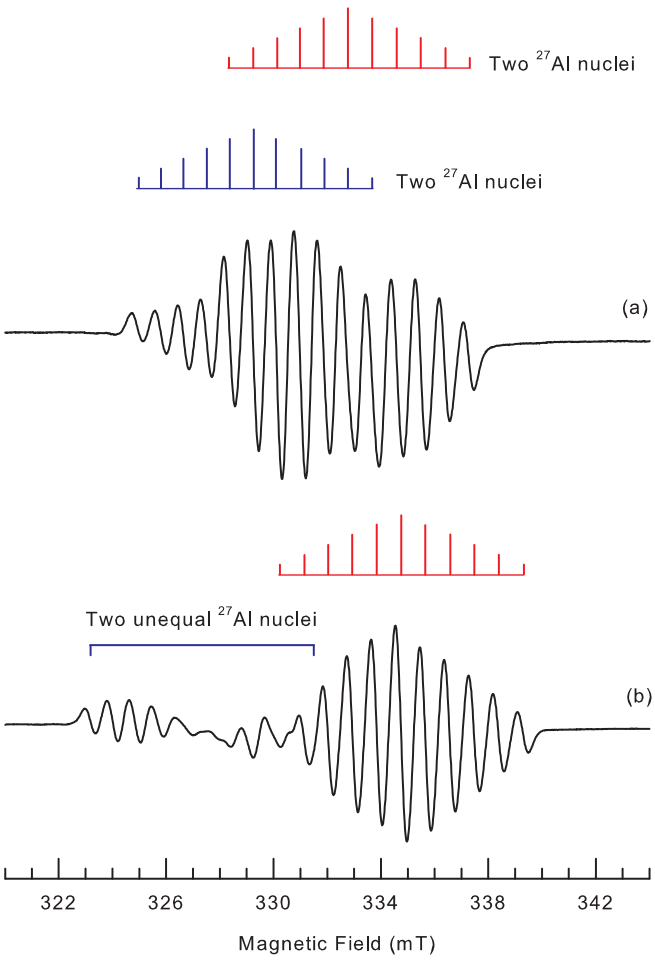

Figure 4.2. Hyperfine spectra of $LiAlO_2$ after irradiation with x rays at 30 K and with a frequency of 9.401 GHz. The inequivalence of the defect sites are resolved for different orientations of the crystal. (a) The magnetic field is along the [110] direction. (b) The magnetic field is along the [100] direction.

we represent the defect as a randomly oriented vector in the crystal-axes coordinate system, then from the symmetry of the crystal the vector will have eight orientations (sites) in the crystal, one in each +[001] quadrant and one in each −[001] quadrant. If the external static magnetic field is along [001], then all eight vectors will make the same angle with respect to the magnetic field, making them magnetically equivalent; this means the EPR signal from each orientation of the defect will be the same. This is what is observed in Figure 4.1, where all orientations of the defect are magnetically equivalent yielding the one 11-line EPR signal. If the magnetic field is along the [100]

or [110] direction, then the vectors in the ±[001] second and fourth quadrants will be magnetically equivalent, and the vectors in the ±[001] first and third quadrants will be magnetically equivalent. This will create two 11-line EPR signals that are each quadruply degenerate; i.e., each signal represents four identical orientations. The reason why the low-magnetic-field set of lines in Figure 4.2(b) are distorted is because the hyperfine interaction matrices between the defect and each of the two closest aluminum nuclei are inequivalent for this direction of magnetic field.

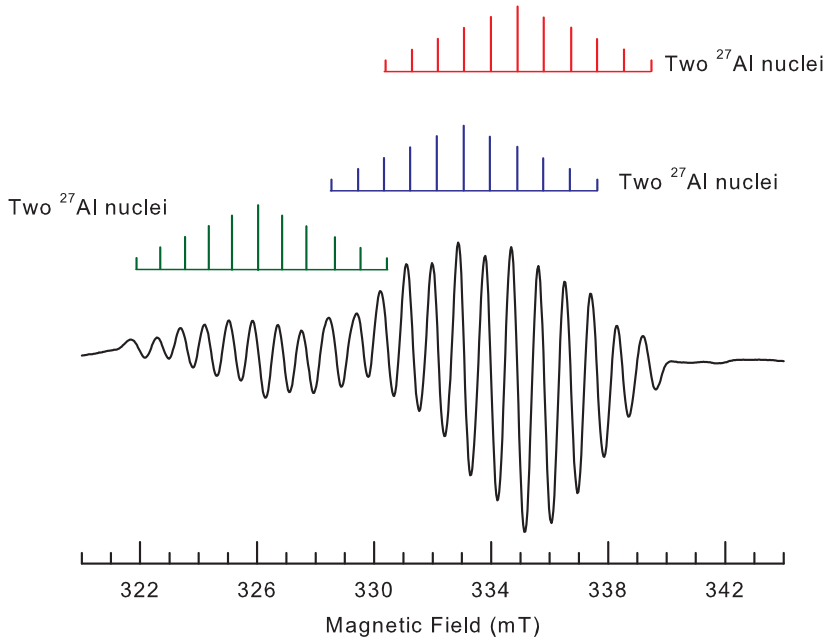

Figure 4.3. Hyperfine spectra of $LiAlO_2$ after irradiation with x rays at 30 K and with a frequency of 9.401 GHz. There are three inequivalent defect sites with resolved spectra for this orientation of the crystal. The magnetic field is along the [101] direction.

In Figure 4.3 we can see the EPR spectrum with the magnetic field along the [101] direction, i.e., the midpoint between the c and a axes in the $c-a$ plane. Along this direction, three sets of 11-line signals are clearly resolved. From the intensities of the signals, the highest field 11-line signal represents four sites while the two lower field signals represent two sites each. Three distinct 11-line signals were the most that could be resolved for the magnetic field orientations that could be easily obtained

with the spectrometer.

When an EPR signal has hyperfine lines that arise from more than one nucleus it is known as superhyperfine and it is caused by an additional splitting of the first hyperfine energy levels by subsequent nuclei [85]. Figure 4.4 shows the energy level splitting caused by the superhyperfine interaction of an $S = 1/2$ electron and two ^{27}Al $I = 5/2$ nuclei. Figure 4.5 shows the final set of energy levels that result from the superhyperfine splitting of the Zeeman levels.

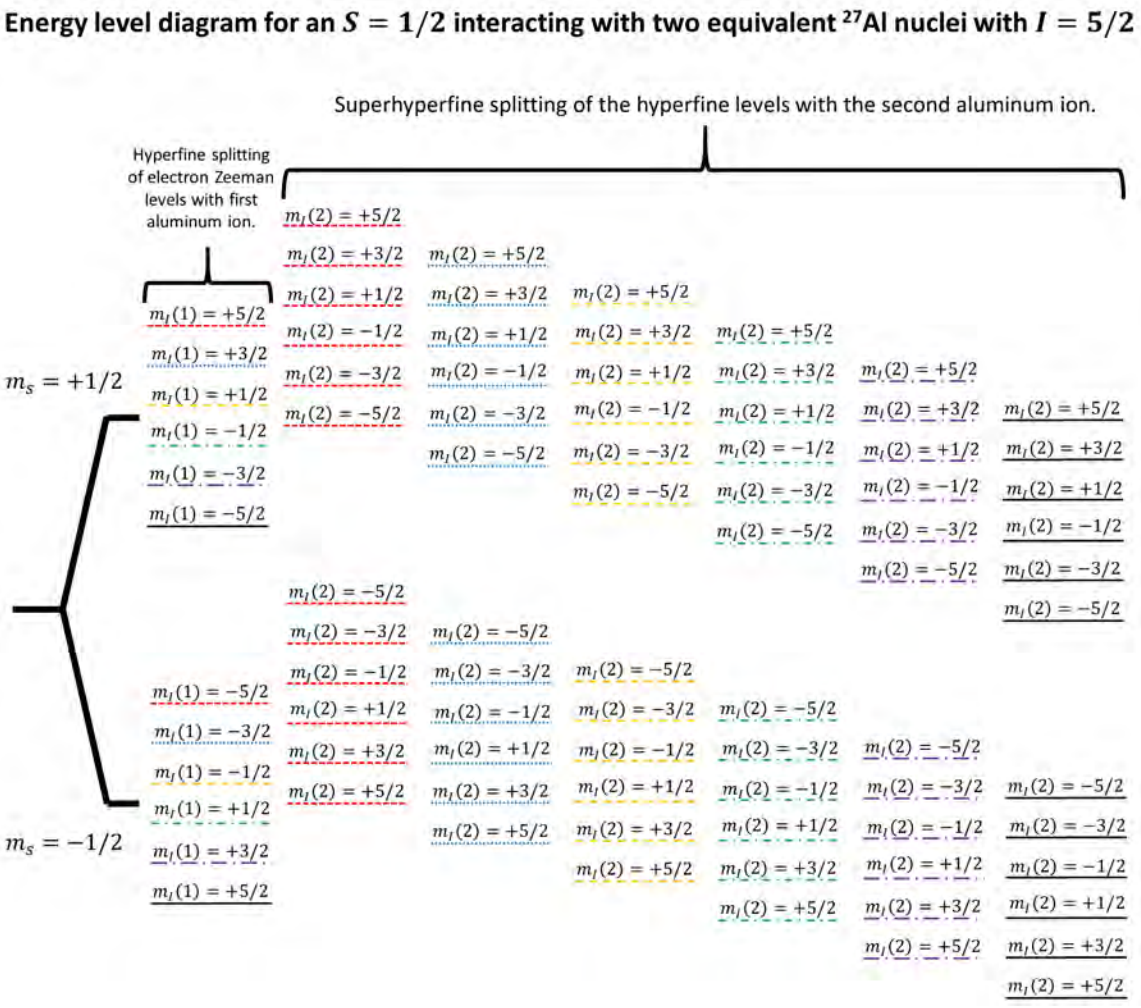

Figure 4.4. Energy level diagram for an $S = 1/2$ electron interacting with two equivalent ^{27}Al nuclei with $I = 5/2$.

First the Zeeman effect lifts the degeneracy of the electron spin energy levels into

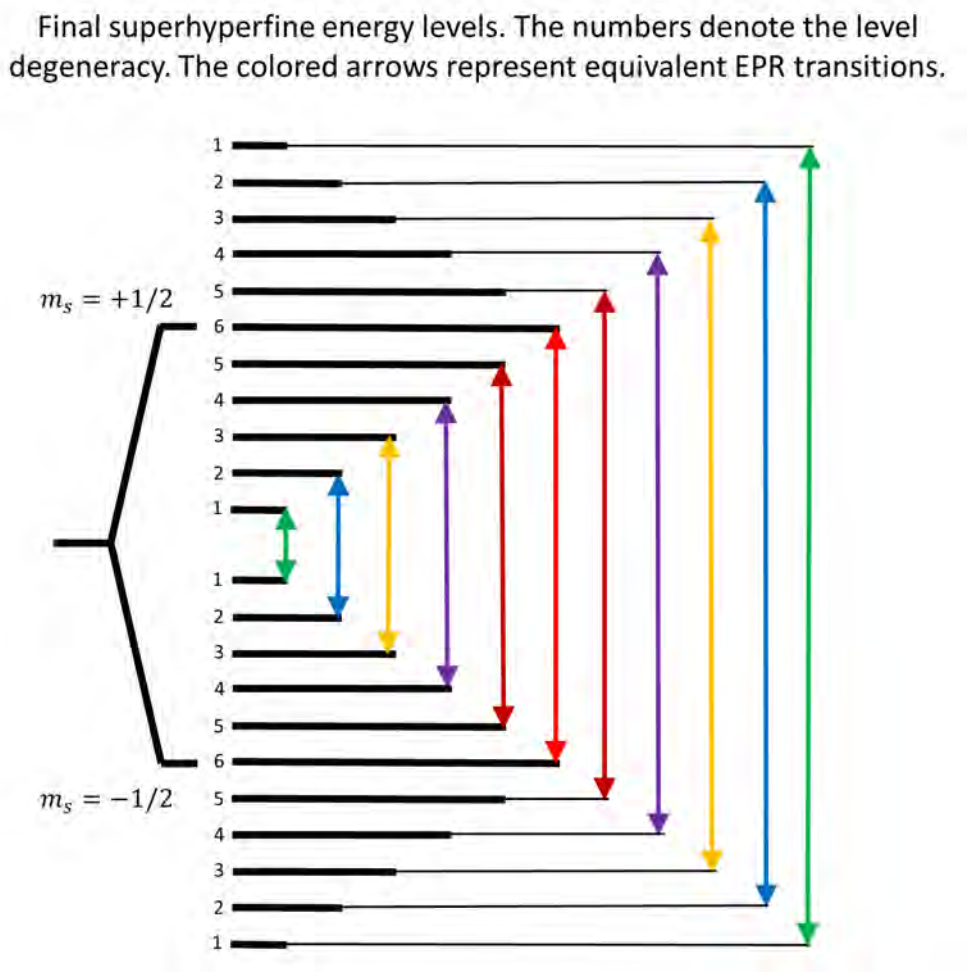

Figure 4.5. The final EPR energy levels and their degeneracies after the superhyperfine splitting. The colored arrows represent equivalent EPR transitions in a fixed frequency EPR spectrometer with scanning B field. The degeneracies of the energy levels creates the symmetry of the 11-line EPR spectrum shown in Figure 4.1.

$m_s = \pm 1/2$, with $m_s = +1/2$ indicating the z component of the electron spin is parallel with $\mathbf{B}$. The magnetic moment of the electron is anti-parallel to its spin, therefore $m_s = +1/2$ is at a higher energy because its magnetic moment is anti-parallel to $\mathbf{B}$ (the magnetic moment parallel to $\mathbf{B}$ being the state of lowest energy). The hyperfine interaction with the first ^{27}Al splits each Zeeman level into the six levels labeled $m_I(1)$. The magnetic moment and the spin of positive nuclei are parallel, so $m_I(1) = +5/2$ in Figure 4.4 implies the spin and magnetic moment are parallel to $\mathbf{B}$. For $m_s = +1/2$ and $m_I(1) = +5/2$, we would have the electron magnetic moment

pointing in the opposite direction as **B**, while the ^{27}Al magnetic moment points in the same direction as **B** and opposite the electron magnetic moment, making $m_I(1) = +5/2$ the highest energy state relative to the electron $m_s = +1/2$ level. The second ^{27}Al then splits each of the first six hyperfine levels into six more superhyperfine levels labeled with $m_I(2)$. The scheme we use to identify a particular level then becomes

$$E(m_s, m_I(1), m_I(2)),$$

Many of the levels are degenerate such as E(+1/2, +5/2/, +3/2) and E(+1/2, +3/2, +5/2), so the final count of energy levels are eleven each for $m_s = +1/2$ and $m_s = -1/2$, which results in eleven EPR transitions with intensities that correspond to the degeneracy of the levels as seen in Figure 4.1.

4.3 Spin Hamiltonian Analysis

The spin Hamiltonian that describes the EPR spectra from the 11-line trapped hole center in $LiAlO_2$ is given by

$$\mathcal{H} = \mu_B \hat{\mathbf{S}} \cdot \mathbf{g} \cdot \mathbf{B} + \hat{\mathbf{S}} \cdot \mathbf{A}_1 \cdot \hat{\mathbf{I}}_1 + \hat{\mathbf{S}} \cdot \mathbf{A}_2 \cdot \hat{\mathbf{I}}_2 - g_n \mu_n \hat{\mathbf{I}}_1 \cdot \mathbf{B} - g_n \mu_n \hat{\mathbf{I}}_2 \cdot \mathbf{B}, \qquad (4.1)$$

where the subscripts refer to the two ^{27}Al nuclei that give rise to the resolved hyperfine patterns observed in the EPR spectra. In this dissertation only the **g** matrix in the Zeeman term is determined. An objective of future work would be to determine the hyperfine matrices $\mathbf{A}_1$ and $\mathbf{A}_2$ as well as a hyperfine matrix for the neighboring lithium ion.

The **g** matrix describes the orientation of the defect relative to the crystal axes and it can be obtained from the EPR spectra by rotating a sample through various planes. In the defect coordinate system the **g** matrix is diagonal and is usually

expressed as [86]

$$\mathbf{g} = \begin{bmatrix} g_x & 0 & 0 \\ 0 & g_y & 0 \\ 0 & 0 & g_z \end{bmatrix} \tag{4.2}$$

In order to calculate the **g** matrix, magnetic field values corresponding to the centers of the aluminum-split hyperfine lines at different orientations of **B** were collected from the EPR spectra, along with their corresponding microwave frequencies, and used as input data for a least-squares fitting program in MATLAB similar to the one used in [87]. The data used is shown in Table 4.1.

Table 4.1. Magnetic field values used in a least-squares fitting program to determine the g matrix of the trapped-hole center.

Direction of **B**	**B** (mT)
[001]	331.795
[101]	325.839
	332.993
	334.893
[100]	327.214
	334.624
[110]	329.116
	332.629

During the fitting routine, the 2×2 spin Hamiltonian matrix ($S = 1/2$) from equation (2.16) was repeatedly diagonalized as the parameters of the **g** matrix were systematically varied. Initially two sets of parameters were found that gave good fits to the data. In order to determine which set of parameters were correct, another set of magnetic field input values was obtained with **B** halfway between the [001] and [110] directions. The final set of **g** matrix parameters, the principal values and principal directions, are displayed in Table 4.2. The Euler angles which describe the directions of the principal axes with respect to the crystal coordinate system have been

Table 4.2. g matrix parameters for the trapped-hole center in $LiAlO_2$ crystals. Estimated error limits are ± 0.0006 for the principal values and $\pm 2^\circ$ for the angles.

	Principal Value	Principal-Axis Direction (θ, ϕ)
g_x	2.0130	(39.2°, 302.6°)
g_y	2.0675	(61.3°, 74.8°)
g_z	2.0015	(65.8°, 179.1°)

converted into (θ,ϕ) pairs. θ is the polar angle defined relative to the [001] direction and ϕ is the azimuthal angle relative to the [100] direction. The values given in Table 4.2 correspond to one of the eight crystallographically equivalent orientations of the trapped-hole center in $LiAlO_2$. The directions for the other seven can be obtained by applying the symmetry operations of the crystal to the values in Table 4.2. Figure 4.6 illustrates the angular dependence of the 11-line spectrum that was computer generated using the parameters in Table 4.2. Each line in the figure corresponds

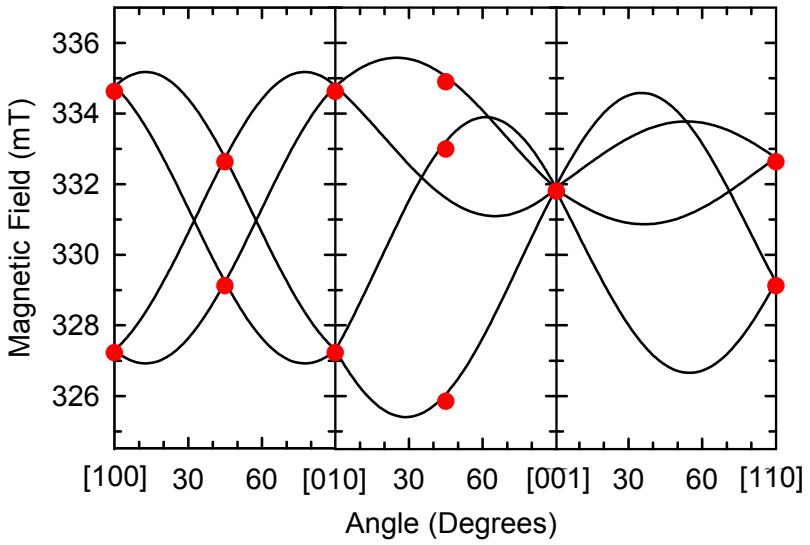

Figure 4.6. Angular dependence of the g matrix for the trapped-hole center in $LiAlO_2$. Midpoints of the ^{27}Al hyperfine spectra are plotted as a function of magnetic field direction for the three high symmetry planes in the crystal. The microwave frequency is 9.401 GHz and the red circles are the data points from Table 4.1.

to the center of an 11-line hyperfine pattern and one of the eight crystallographic orientations. Only four lines are shown for each rotation because the +[001] quadrant

sites are pairwise degenerate with the -[001] quadrant sites.

4.4 Trapped-Hole Center Discussion

Lithium vacancies are present during growth and are created as charge compensators for transition-metal impurities such as iron. Under ionizing radiation, as electrons and holes move through the crystal, the holes can become trapped on doubly negative oxygen ions if one of the adjacent cations is missing or has been replaced by an impurity cation deficient in charge. This is a known and documented phenomena in many simple oxides such as MgO [68], Al_2O_3 [88], SiO_2 [89] and ZnO [90]. A more recent example in a ternary oxide is lithium tetraborate ($Li_2B_4O_7$), where a hole becomes trapped on an oxygen ion adjacent to a lithium vacancy and has an equal hyperfine interaction with two neighboring $I = 3/2$ boron neighbors that generates a seven line EPR spectrum [91].

The trapped hole in $LiAlO_2$ is stabilized by the lithium vacancy and the hole-lattice coupling favors the hole remaining trapped at one oxygen ion instead of spread out among several. This trapped hole localized on an oxygen ion creates an O^- small bound polaron [83]. Analysis of the g matrix anisotropy and the resolved hyperfine lines support this model of an acceptor bound polaron as will be shown in the following discussion.

O^- is a ^2P state ion ($L = 1$, $S = 1/2$) with an electronic configuration given by $(1s^2 2s^2 2p_x^2 2p_y^2 2p_z)$. In the free ion these orbitals are all degenerate but under the influence of the crystal electric field the degeneracy is broken into three discrete energy levels E_1, E_2, and E_3. E_1 represents the ground state energy with the hole in the p_z orbital while E_2 and E_3 represent the hole occupying the p_y and p_x orbitals respectively. Spin-orbit interactions mix the excited states with the ground state causing a change in the effective g factor. To first order, the principal values can be

represented by [92]

$$g_x = g_e - \frac{2\lambda}{E_3 - E_1}, \qquad g_y = g_e - \frac{2\lambda}{E_2 - E_1}, \qquad g_z = g_e = 2.0023, \tag{4.3}$$

where λ is the spin-orbit coupling constant. Section 4.5 expounds upon the significance of the energy denominators in equation (4.3) as they relate to the trapped hole.

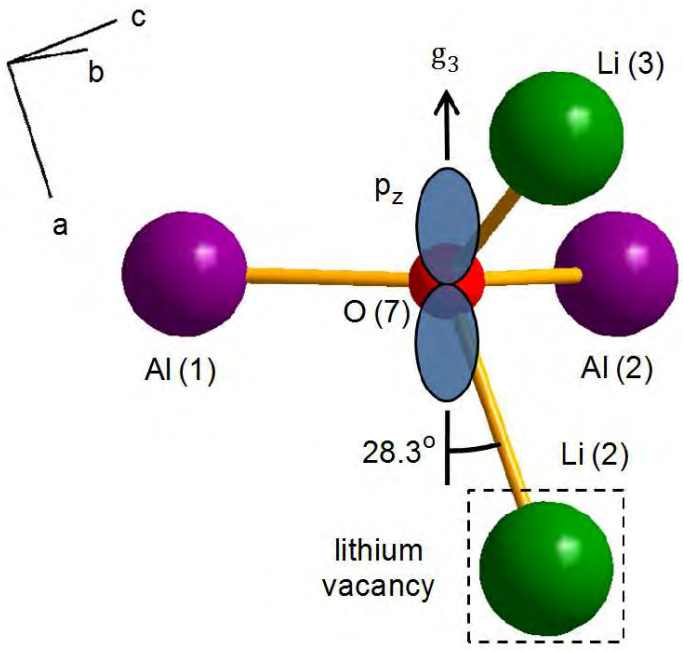

Figure 4.7. Model of one of the eight possible orientations of the trapped-hole center in $LiAlO_2$. The labels from Table 1.2 and Figure 1.4 have been used.

As shown in Table 4.2, g_z is very close to the free electron value differing by only 0.04%. According to Bartram *et al* [93], λ for an O^- ion is $-135\,\mathrm{cm}^{-1}$, which would cause positive g shifts from the free electron value for g_x and g_y, exactly as observed in Table 4.2. The principal values in Table 4.2 conform to theory for a hole trapped on an oxygen ion. The principal-axis directions were used to determine the orientation of the trapped hole with respect to the crystal axes and the result is shown in Figure

4.7.

In Figure 4.7 we have a trapped hole localized on O(7), with Al(1) and Al(2) being the closest aluminum neighbors and Li(2) and Li(3) the closest lithium neighbors. The orbital containing the hole, p_z, is oriented nearly perpendicular to the Al(1)-O(7)-Al(2) plane because this allows the hole to minimize to the greatest extent possible its interaction energy with the surrounding cations. p_x (not shown) is in the Al(1)-O(7)-Al(2) plane and perpendicular to p_z. p_y (not shown) is nearly parallel to a line from Al(1) to Al(2) and perpendicular to p_z and p_x. These crystallographic directions relative to O(7) are given in (θ, ϕ) pairs in Table 4.3. Comparing the

Table 4.3. Crystallographic directions associated with the trapped hole on the oxygen-centered tetrahedron shown in Figure 4.7. These directions pass through the oxygen ion and form a right-hand coordinate system that can be compared to the g matrix principal-axis directions in Table 4.2. The labels are consistent with Table 1.2 and Figures 1.4 and 4.7.

	Direction	(θ,ϕ)
p_x	In the Al(1)-O(7)-Al(2) plane perpendicular to the Al(1)-Al(2) line	(37.8°,295.0°)
p_y	Along the Al(1)-Al(2) line	(59.8°,73.5°)
p_z	Normal to the Al(1)-O(7)-Al(2) plane	(69.5°,176.1°)

principal directions given in Table 4.2 with those in Table 4.3 shows extremely good agreement with p_x, p_y, and p_z corresponding to g_x, g_y, and g_z. Some disagreement with the g-values is to be expected as the angles associated with the p-orbitals were calculated without taking into account the relaxation of the crystal lattice that would occur with a missing lithium ion. The **g** matrix parameters in Table 4.2 and the directions in Table 4.3 validate the model of a trapped hole on an oxygen as shown in Figure 4.7. Since the trapped-hole center can be induced with room temperature x ray irradiation, the defect is stable at room temperature which is consistent with the hole being immediately adjacent to the lithium vacancy (An $O^-$with no immediately

adjacent lithium vacancy is more likely to see the hole hop to other oxygen ions and ultimately recombine). Because p_z is at an angle of 28.3° with the O(7)-Li(2) direction and an angle of 52.9° with the O(7)-Li(3) direction, the lobe of the p_z orbital is closest to Li(2). From a minimization of electrostatic energy standpoint, Li(2) must contain the lithium vacancy.

4.5 Optical Absorption Results

There has been a significant amount of research conducted on the optical properties of $LiAlO_2$ in the undoped state [6–8, 94, 95], as well as doped with Cr [26], Cr co-doped with Mg [96], Cu [6], Fe [97–99], Mn [100, 101], Ce and Tb [100], Eu [102], and Ti [5]. Unlike with EPR, optical studies alone cannot reveal any information about what type of defect may be contributing to the observed optical effects. In conjunction with EPR however, optical measurements can be a very useful tool in understanding the fundamental properties of a material.

The optical absorption spectrum of the 0.5 mm thick sample used to obtain the EPR spectra in this chapter was measured before and after ten minutes of irradiation with 60 kV, 30 mA x rays at room temperature. Figure 4.8 shows the absorption spectra before and after irradiation, and the difference between the two. The crystal had both of its faces polished and was mounted in the spectrometer such that light propagated along the [001] direction. The data has been corrected for reflective losses using [103]

$$\alpha = \frac{1}{z \log_{10}(e)} [\text{O.D.} + 2 \log_{10}(1 - R)] \qquad [\text{cm}^{-1}], \tag{4.4}$$

where z is the sample thickness and assumed to be much larger than the coherence length of the transmitted light, R is the reflectivity, e is Euler's number, and $2 \log_{10}(1-$

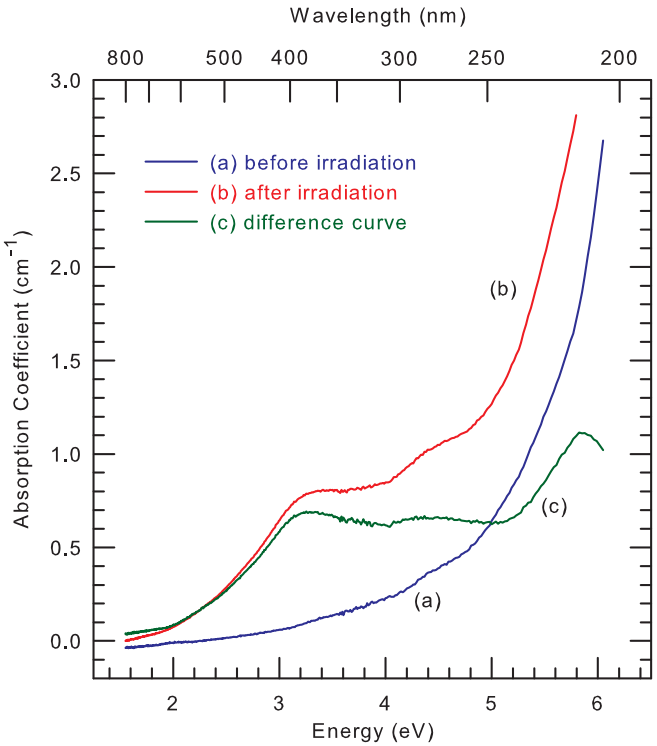

Figure 4.8. Optical absorption spectra from $LiAlO_2$ taken at room temperature with unpolarized light propagating along the [001] direction. (a) Before x ray irradiation. (b) After irradiation with x rays generated with 60 kV at 30 mA. (c) Difference between the before and after spectra, also known as a radiation-induced spectrum.

R) is the term that accounts for reflective losses. The reflectivity is given by

$$R = \left(\frac{n-1}{n+1}\right)^2, \tag{4.5}$$

where n is the index of refraction. Ideally, one would need the values of the index of refraction for every wavelength in the region measured. However, only seven values of the refractive indices of $LiAlO_2$ within the $460 - 660$ nm region have been published [37]. Since wavelength dependent corrections could not be made, the ordinary refractive index of 1.6345 at 460 nm as reported in [37] was applied across the entire $200 - 800$ nm measurement range in Figure 4.8. Since the index of refraction has an inverse relationship with wavelength in what is known as dispersion [104], there

will be an upward trend at wavelengths shorter than 460 nm in Figure 4.8 due to the increasing refractive index that will remain uncorrected. This makes it difficult to determine if any low-intensity broad ultraviolet absorption bands are present in the as-grown crystal.

As shown in Figure 4.8, x rays produce broad overlapping absorption bands in the visible and ultraviolet regions with peaks appearing near 3.27, 4.46, and 5.87 eV (379, 278, and 211 nm, respectively). These peaks are most likely charge-transfer bands associated with transition-metal impurities unintentionally introduced during crystal growth. In several x ray irradiated lithium aluminate samples, EPR signals from Cr^{3+} have been observed [26], and it will be shown in Chapter 5 that Fe^{2+} acts as a major electron trap in this material. Absorption bands associated with these transition-metal impurity charge states should be associated with the EPR signals, and it is established in Chapter 6 that the 379 nm peak is related to the Fe^{+} charge state. In order to establish precisely which absorption bands correlate with which impurities will require several samples doped with different concentrations of transition-metal ions utilized in a combined optical and EPR study. Such samples are unavailable for this dissertation, but could be a focus of future research.

Returning to equation (4.3), the denominators represent transitions between the energy levels or p orbitals of the O^{-} ion. The values of these transitions allow a prediction of where optical absorption peaks might be expected to appear. Substituting the g values from Table 4.2 and $\lambda = -135\,\mathrm{cm}^{-1}$ for the spin-orbit coupling constant into equation (4.3) gives

$$E_3 - E_1 = 25324\,\mathrm{cm}^{-1} \text{ or } 396\,\mathrm{nm} \tag{4.6}$$

$$E_2 - E_1 = 4141\,\mathrm{cm}^{-1} \text{ or } 2.41\,\mu\mathrm{m}. \tag{4.7}$$

Equation (4.6) indicates that we can expect an absorption band near 396 nm, which

is close to the observed band near 379 nm in Figure 4.8. However, during a thermal annealing experiment, the EPR signal in Figure 4.1 was seen to decay away while the 379 nm absorption band remained. The absorption bands from a small bound polaron should be wide and lie in the visible range or close to it, but the values of the $E_3 - E_1$ and $E_2 - E_1$ crystal field excitations may not be good predictors of the positions of the absorption bands according to Schirmer [83, 105]. In the crystal field model, the ground state of our trapped-hole center has the hole localized on only one oxygen ion, and excitations involve transitions to higher excited states on the same oxygen ion. These are intra-polaron transitions, but as Schirmer explains, small bound polaron absorption often involves inter-polaron transitions, where the hole moves from the O^- to one or more of the surrounding O^{2-} ions. These inter-polaron charge-transfer transitions would have different absorption band positions and oscillator strengths than that predicted by the crystal field splitting model. In any event, even if the precise location of the absorption bands due to the trapped-hole was known, it's possible they still wouldn't be visible due to the broad charge-transfer absorption bands from the transition-metal impurities.

An intense optical absorption band centered near 5.25 eV (236 nm) has been reported in $LiAlO_2$ irradiated with 2 MeV He^+ ions and 2.5 MeV electrons [25, 94] and 10 keV deuterons (D_2^+) [106]. Both groups speculate this band is due to oxygen vacancies (i.e., F^+ centers) formed by knock-on damage from high-energy charged particles. The absence of this absorption band in Figure 4.8 suggests that as-grown $LiAlO_2$ crystals do not contain any significant concentrations of oxygen vacancies.

4.6 Thermoluminescence Results

The radiation-induced trapped-hole center was further characterized by measuring its thermal stability during isochronal thermal annealing experiments. The sample

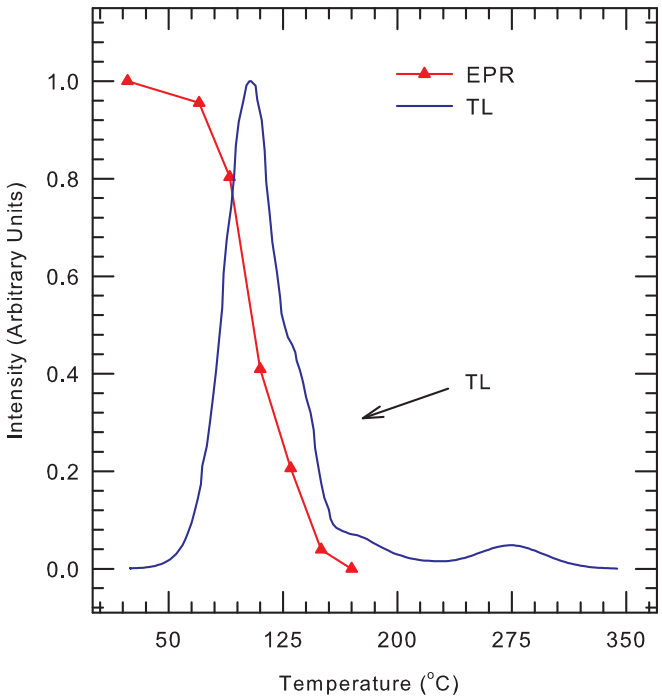

Figure 4.9. Comparison of thermoluminescence data (blue curve) and EPR thermal anneal data (red curve). These results indicate that the 11-line EPR trapped-hole center directly participates in the 105 °C peak.

was first annealed at 400 °C for 15 minutes in a bench-top furnace to remove the effects of previous radiation exposures. The sample was then irradiated for 10 minutes at room temperature with 60 kV, 30 mA generated x rays and placed inside the microwave cavity where an EPR spectrum was taken at 30 K. The sample was placed in the furnace again where it was annealed for 25 s at 70 °C, after which it was put back into the microwave cavity and another EPR spectrum taken at 30 K. This procedure was repeated at 90 °C with a 25 s holding time and continued in 20 °C increments until the 11-line EPR signal monitored at 30 K was completely gone. The signal intensity was monitored by measuring the vertical distance between the turning points of the center line in Figure 4.1. The equivalent constant heating rate from this procedure was approximately 0.80 °C/s. After the EPR annealing data were obtained, the

sample was again initially heated to 400 °C for 15 minutes and then irradiated for 10 minutes at room temperatures with x rays. A TL glow curve was obtained from the sample using the Harshaw 3500 taken with a constant heating rate of 1 °C. Figure 4.9 shows the EPR thermal anneal data along with the thermoluminescence glow curve.

Figure 4.9 shows that there is one intense peak near 105 °C and three smaller peaks near 138, 176, and 278 °C. The peak near 105 °C clearly coincides with the thermal decay of the 11-line EPR signal and provides the first explanation for what causes this first order glow peak. Previous research groups had reported a TL glow peak near 100 °C but did not identify the defects responsible [7,9]. Other EPR signals were also measured during this thermal annealing experiment, specifically those believed to arise from transition-metal ions. These signals decay throughout the 90 to 300 °C region but unlike the trapped-hole center, none of the monitored signals lost 100% of their radiation-induced intensities in a single step near 105 °C. This would seem to indicate that it is the trapped-hole that becomes unstable and is released near 105 °C. Upon release, the holes migrate though the crystal and recombination occurs at one or more of the trapped-electron sites (i.e., transition-metal-ion impurities that trapped an electron during the initial irradiation at room temperature). In order to make definitive assignments on the nature of the recombination sites associated with the 105 °C TL peak in $LiAlO_2$, more information about the emitted light such as spectral dependence and lifetimes are needed.

V. Characterization of an Extrinsic Electron Center in $LiAlO_2$

5.1 Introduction

In the previous chapter the major hole trap in $LiAlO_2$ single crystals was described and characterized. Since the net charge in a solid must always be zero, whenever there is a trapped-hole, there must also be a compensating trapped-electron in the crystal. The point defect that acts as the primary electron trap is caused by iron impurities that are inadvertently introduced into the crystal during growth. Fe^{2+} ions replace Li^+ ions in the as-grown crystal, and trap electrons under ionizing radiation thereby converting to the Fe^+ charge state. In this chapter the primary electron trap caused by iron impurities is characterized and analyzed (primary is defined in terms of largest relative signal intensity).

5.2 Electron Paramagnetic Resonance Results

As stated in the previous chapter there are essentially no EPR signals in an as-grown lithium aluminate crystal except for very weak signals visible at low temperatures. After irradiation with 60 kV 30 mA generated x rays, along with the appearance of the 11-line trapped-hole center, several weak single line EPR signals can also be seen at 30 K with **B** along [001]. Figures 5.1(a) and (b) show EPR spectra taken at 30 and 13 K after x ray irradiation using a 3 mm × 5 mm × 0.5 mm sample.

In Figure 5.1(a) the 11-line spectrum is clearly present along with small single line EPR signals. These are the only signals visible along the entire measurable magnetic field range of 1.3 T. If the temperature is raised from 30 K, all of the signals visible in Figure 5.1(a) are reduced and eventually only a few very weak peaks from the 11-line signal are visible at room temperature. Figure 5.1(b) is a spectrum of the

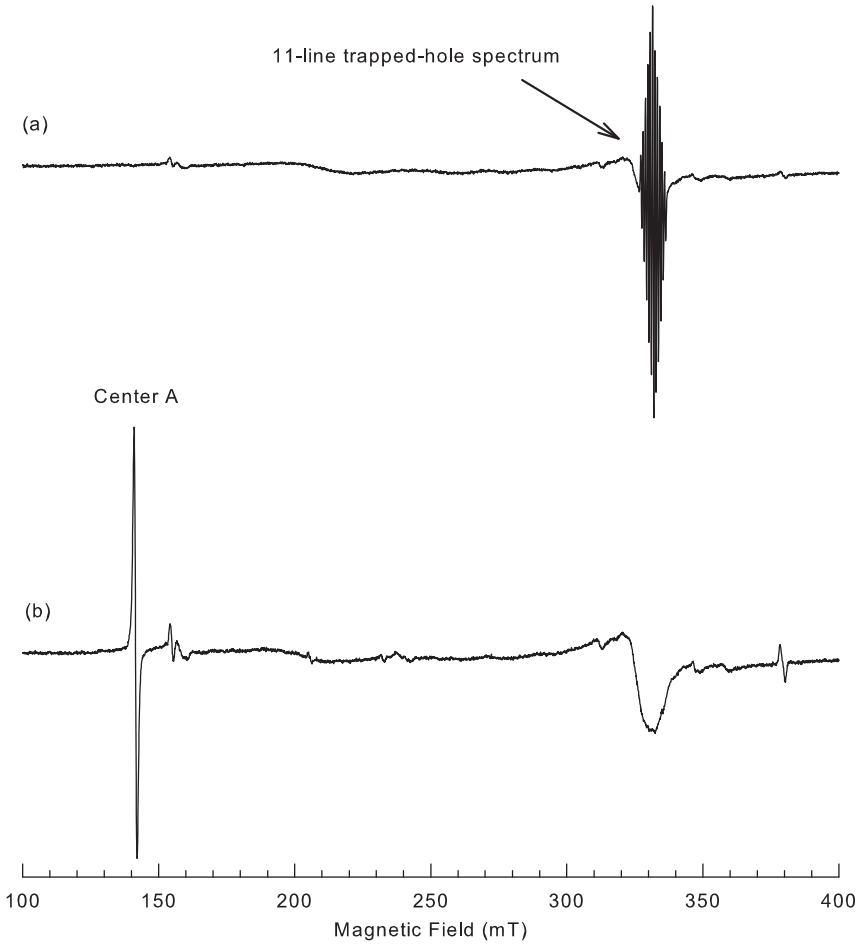

Figure 5.1. $0.3\,\mathbf{T}$ **wide EPR spectrum of a** $\mathbf{LiAlO_2}$ **single crystal recorded after x ray irradiation. The frequency is** $9.401\,\mathbf{GHz}$ **and the magnetic field is along the [001] direction. (a) At** $30\,\mathbf{K}$ **the 11-line trapped-hole spectrum discussed in Chapter 4 is the only significant EPR signal. (b) At** $13\,\mathbf{K}$ **the 11-line signal has disappeared due to spin-lattice relaxation effects and a single EPR line at** $141.5\,\mathbf{mT}$ **has become visible.**

same crystal, at the same orientation, and over the same magnetic field sweep but at 13 K. The EPR line at 141.5 mT, labeled Center A, begins to be visible below 20 K. The 11-line signal and the other weak EPR signals are no longer visible at this temperature but some new weak signals have appeared. The 11-line signal disappears and Center A appears at lower temperatures due to spin-lattice relaxation effects.

If N_u and N_l represent the occupancy numbers of an upper and lower Zeeman level, respectively, then a thermodynamic parameter known as the spin temperature

T_s can be defined as

$$\frac{N_u}{N_l} = \exp\left(-\frac{\Delta U}{k_B T_s}\right), \tag{5.1}$$

where ΔU represents the energy difference per spin [107]. Although electrons and protons obey Fermi-Dirac statistics, Maxwell-Boltzmann statistics can be used to first order as long as the interaction between spins is sufficiently weak. However, the interaction between spins must be strong enough to maintain thermal equilibrium within the spin system or T_s will have no meaning. In general, there will be more spins in the lower energy state than in the upper energy state. When a photon is absorbed that possesses an energy ΔU, a spin will gain sufficient energy to move from N_l to N_u. Since the spin system has gained energy, it can be considered at a higher temperature than its surroundings, and this is the meaning of the spin temperature. The spin system will interact with its surroundings and lose energy until T_s equals the temperature of the surroundings T.

The energy absorbed will decay exponentially according to

$$\delta U = \delta U_0 \exp\left(-\frac{t - t_0}{\tau_1}\right), \tag{5.2}$$

where δU_0 is the excess energy at time $t = t_0$, and τ_1 is the characteristic time that it takes for energy to decay to $1/e$ of its initial value known as the spin-lattice relaxation time. In general, τ_1 is proportional to T^{-n}, where n is an integer that can be 1 or vary from 5 to 9 [108]. As a result, τ_1 will become smaller as T increases and larger as T decreases. The reason why Center A is not visible above 20 K is because τ_1 for Center A has become too small. As τ_1 approaches zero, the spin temperature approaches the temperature of its surroundings, decreasing the absorbed energy and broadening the EPR signal. The 11-line signal isn't visible at 13 K due to a related effect known as power saturation. If the radiation density of the absorbed microwave energy becomes

too large, the probability of absorption between levels becomes equal, and no net absorption occurs extinguishing the EPR signal. It is important to keep in mind that both of the defects responsible for Center A and the 11-line spectrum still exist and are not being created or destroyed at lower temperatures, they just cannot be seen with EPR unless the spectrum is taken at the appropriate temperature.

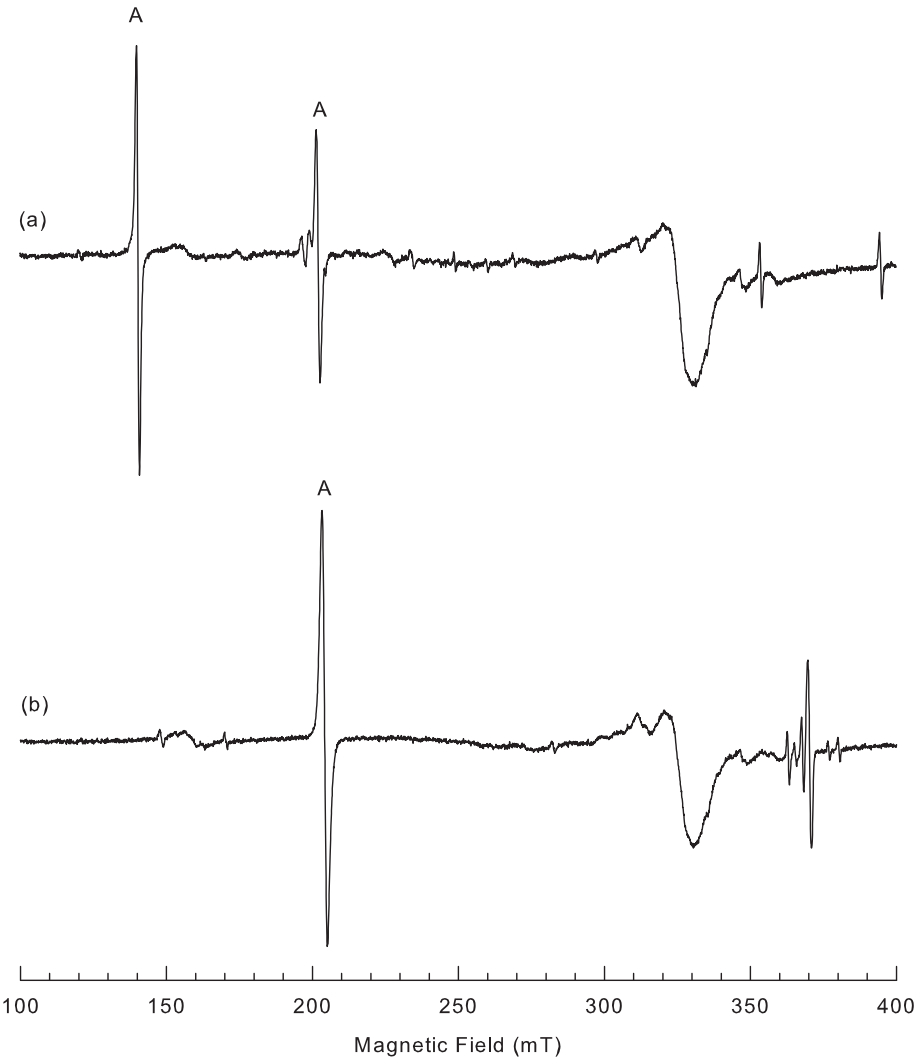

Figure 5.2. EPR spectra of $LiAlO_2$ after irradiation with x rays recorded at 13 K with a frequency of 9.401 GHz. (a) The magnetic field direction is along the [101] direction. (b) [100] direction

Returning to Figure 5.1, the small signals in the EPR spectrum are mostly due to

transition-metal impurities that were inadvertently introduced into the crystal during growth. They can be either electron traps or hole traps depending on the charge state of the impurity; all of them may contribute to the absorption, luminescence, or other effects that arise from point defects. However, it is beyond the scope of this dissertation to analyze every EPR signal that appears in the spectrum, and therefore the rest of this chapter will focus on Center A, since it is the largest signal aside from the trapped-hole and therefore will contribute the most to charge trapping processes.

Center A has a linewidth of 1.1 mT and, using equation (3.2), represents $1.92 \times 10^{17}\,\mathrm{cm}^{-3}$ spins. The fact that the spin density of Center A is about half that of the 11-line spectrum indicates that there are other electron trapping defects (possibly non-paramagnetic) that remain unidentified because there must be an equal number of electron and hole traps. Figure 5.2 shows Center A along the [101] and [100] directions. As the magnetic field is varied from [001] to [100], Center A splits into two separate signals, each representing four distinct orientations of the point defect. These signals both move to higher magnetic field and separate further, until reaching the [100] orientation where both signals come together again at 204.3 mT. This large observed g-shift as the magnetic field is rotated from [001] to [100] is indicative of a $3d^7$ ion with an effective $S' = 1/2$ spin which is elaborated upon in the next section.

5.3 Spin Hamiltonian Analysis

Fe^+ is a $3d^7$, $S = 3/2$ ion, and the spin Hamiltonian for a $3d^7$ ion on a site with tetrahedral symmetry is [109, 110]

$$\mathcal{H} = \mu_B \hat{\mathbf{S}} \cdot \mathbf{g} \cdot \mathbf{B} + \hat{\mathbf{S}} \cdot \mathbf{D} \cdot \hat{\mathbf{S}} + u\mu_B \left\{ \hat{S_x}^3 B_x + \hat{S_y}^3 B_y + \hat{S_z}^3 B_z - \frac{1}{5}\left(\hat{\mathbf{S}} \cdot \mathbf{B}\right)\left[3S(S+1) - 1\right] \right\}, \quad (5.3)$$

where u is a unitless "g" like parameter and the terms in brackets arise from perturbation theory. The higher order terms in $\hat{\mathbf{S}}$, shown in brackets in equation (5.3), are added when dealing with $S \geq 3/2$ magnetic species [111]. In general, the higher order terms are small and can be neglected. For example, Co^{2+} in ZnS is another tetrahedrally coordinated $3d^7$ ion, and $u = -0.0048$ for that impurity [112]. Although these higher order terms should exist for the Fe^{+} ion in $LiAlO_2$, they are assumed to be small enough to ignore.

A characteristic of many transition-metal ions in a crystalline field is a high zero-field splitting. Figure 5.3 shows what happens to the Zeeman levels when the splitting is greater than the EPR transition energy ΔU. In Figure 5.3, the zero-field splitting

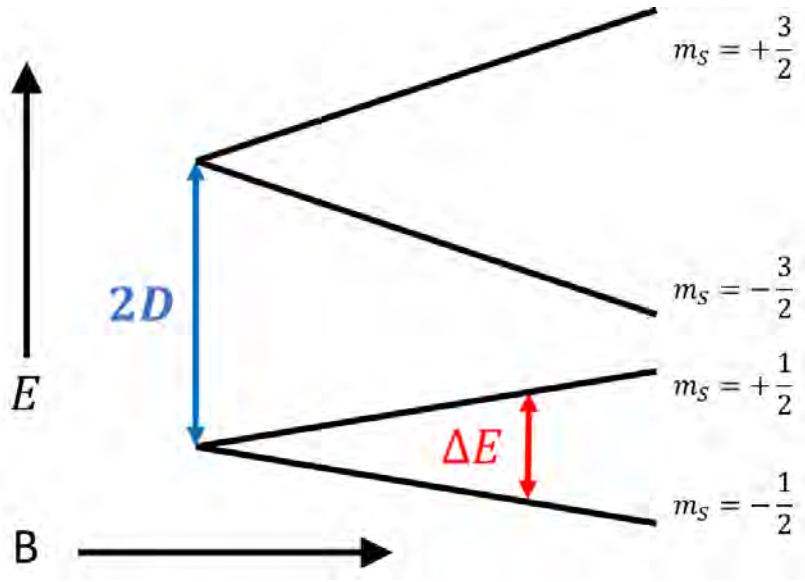

Figure 5.3. Fine-structure splitting for a $S = 3/2$ system. ΔE is the EPR transition energy that can be measured using $\nu = 9.401\,\text{GHz}$. The zero-field splitting is so large that $|2D| \gg \Delta E = h\nu$.

is so large that it is greater than the EPR transition energy that can be measured at $\nu = 9.401\,\text{GHz}$. In this situation, the $m_S = +3/2$ to $+1/2$ and $m_S = -3/2$ to$-1/2$ EPR transitions are inaccessible for EPR spectrometers operating at X-band frequencies. Depending on the size of the zero-field splitting, higher frequency spectrometers operating at the $\nu \approx 36\,\text{GHz}$ "Q-band" may be able to access all of the

EPR transitions which would result in a three line ($2S$) spectrum from an $S = 3/2$ ion.

Since the $m_S = +1/2$ to -1/2 EPR transition is the only one accessible for the X-band spectrometer, transition-metal ions with high zero-field splittings can be viewed as having an effective $S' = 1/2$ (the $\mathbf{S} \cdot \mathbf{D} \cdot \mathbf{S}$ term is contained within the effective electron Zeeman term). This means of course that the EPR spectrum when viewed along a high symmetry direction of the defect will appear as a single line, just like Center A. Now that Fe^+ can be treated as an $S = 1/2$ ion and the higher order terms can be neglected, the spin Hamiltonian for Fe^+ in tetrahedral symmetry reduces to the Zeeman term. This effective Zeeman term can be written as

$$\mathcal{H} = \mu_B \left[g'_{\shortparallel} \hat{S}'_z B_z + g'_{\perp} \left(\hat{S}'_x B_x + \hat{S}'_y B_y \right) \right], \tag{5.4}$$

where $g'_{\shortparallel}$ and $g'_{\perp}$ are the observed effective g factors when the magnetic field is parallel or perpendicular to the z-axis of the defect coordinate system. $g'_{\shortparallel}$ and $g'_{\perp}$ can be calculated for Center A using its linepositions for the [001] and [100] directions, respectively

$$g'_{\perp} = \frac{h\nu}{\mu_B B_{\perp}} = \frac{6.626 \times 10^{-34}\,\mathrm{J{\cdot}s} \times 9.401 \times 10^{9}\,\mathrm{s^{-1}}}{9.27401 \times 10^{-24}\,\mathrm{J\ T^{-1}} \times 0.2043\,\mathrm{T}} = 3.2877 \tag{5.5}$$

$$g'_{\shortparallel} = \frac{h\nu}{\mu_B (0.1415\,\mathrm{T})} = 4.7468. \tag{5.6}$$

It is important to keep in mind that these are not the real g principal values but parameters that can be useful when comparing the observed linepositions in EPR spectra.

The actual $\mathbf{g}$ matrix for Center A with $S' = 1/2$ was solved in the same manner as the trapped-hole in Section 4.3 using the magnetic field values of the linepositions as the sample was rotated through various planes. The principal values and directions

of the g-values are shown in Table 5.1. Figure 5.4 shows the computer-generated

Table 5.1. g matrix parameters for the trapped-electron center in $LiAlO_2$ crystals. Estimated error limits are ± 0.0006 for the principal values and $\pm 2^\circ$ for the angles.

	Principal Value	Principal-Axis Direction (θ, ϕ)
g_x	3.6301	(89.89°, 224.96°)
g_y	2.1232	(64.99°, 134.91°)
g_z	5.1401	(25.00°, 315.19°)

angular dependence prediction of the Center A lineposition plotted along side the data points used in calculating the **g** matrix parameters. Since the crystal structure

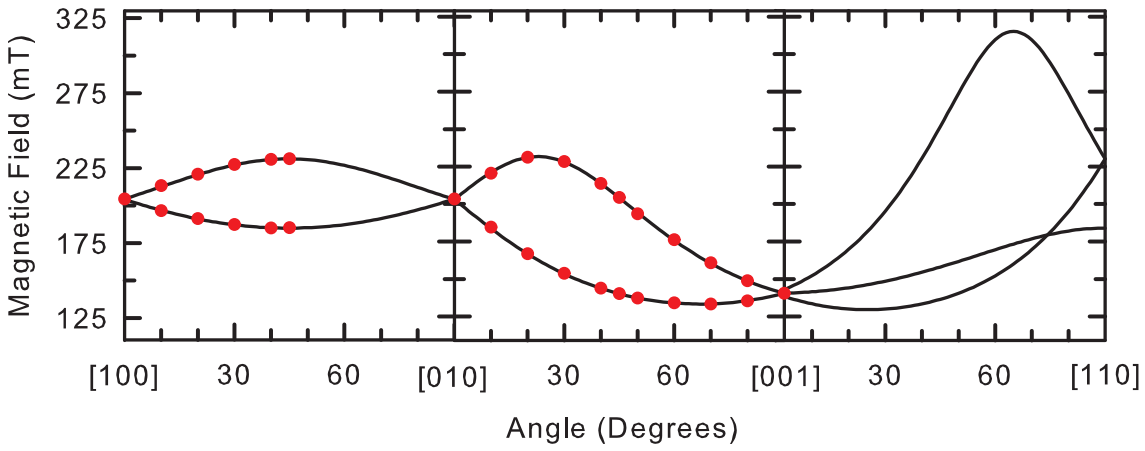

Figure 5.4. Angular dependence of the g matrix for the trapped-electron center in $LiAlO_2$. Center A magnetic field positions are plotted as a function of magnetic field direction for the three high symmetry planes in the crystal. The microwave frequency is 9.401 GHz.The red circles are the data points from Table 5.2.

of lithium aluminate is tetragonal, if the x, y, and z axes of the defect aligned with the crystal axes, then $g_x = g_y$ should have been obtained. The fact that $g_x \neq g_y$ in Table 5.1 indicates the defect axes are not aligned with the crystal axes. Table 5.2 shows the magnetic field values used in the least-squares MATLAB program to obtain the results in Table 5.1 and Figure 5.4.

Table 5.2. Magnetic field values used in a least-squares fitting program to determine the g matrix of the trapped-electron center.

Direction of **B**	**B** (mT)	Direction of **B**	**B** (mT)	Direction of **B**	**B** (mT)
[001] to [100]				[100] to [010]	
[001]	141.380	+45°	205.330	[100]	204.340
+10°	136.302	+50°	144.865	+10°	196.508
+10°	149.726	+50°	214.647	+10°	213.258
+20°	134.260	+60°	154.691	+20°	191.196
+20°	161.729	+60°	229.288	+20°	220.817
+30°	135.052	+70°	167.840	+30°	187.286
+30°	177.144	+70°	232.179	+30°	227.287
+40°	138.190	+80°	185.519	+40°	184.940
+40°	194.448	+80°	221.444	+40°	230.765
+45°	141.240	[100]	204.340	+45°	185.177
				+45°	231.151

5.4 Trapped-Electron Center Discussion

Previous EPR spectroscopy results have shown that iron impurities in nominally pure compounds can exist in paramagnetic charge states [113–116], and Auvray-Gely *et al* specifically reported iron as the largest trace impurity in their $LiAlO_2$ samples [25]. Iron enters a crystal during growth and acts as a charge compensating defect. In the case of $LiAlO_2$, iron sits at a lithium site in the 2+ charge state and compensates the large number of lithium vacancies that were shown in Chapter 4 to exist in the crystal. It is not known whether Fe^{2+} sits at an isolated lithium site or is at a site adjacent to a lithium vacancy. Fe^{+} and Fe^{3+} are relatively easy to observe with EPR because of their odd number of electrons in the *d* shell. While Fe^{2+} is EPR active because of the unpaired electrons in the *d* shell (Hund's rules say that electrons in the *d* shell will fill empty orbitals first before pairing up, so Fe^{2+} has two paired electrons in the first *d* orbital, and four unpaired electrons in the next

four orbitals [117]), it has been found experimentally that *d*-shell ions with an even number of electrons are difficult to observe with EPR when the Zeeman effect is small compared to the fine-structure splitting [118, 119]. Since no EPR spectra are visible in as-grown lithium aluminate crystals, it can be safely concluded that iron is not in the easy to observe 1+ or 3+ charge states prior to x ray irradiation.

Table 5.4. The ionic radii of Li^+, Al^{3+}, Fe^{2+}, and Fe^{3+} when surrounded by four anions [120].

Element	Effective Ionic Radii in pm (10^{-12} m)
Al^{3+}	39
Fe^{2+}	63
Fe^{3+}	49
Li^+	59

Table 5.4 lists the effective ionic radii of the lithium aluminate constituent cations and the iron ion in different oxidation states. While it is not impossible for the Fe^{2+} ion to sit at an aluminum site, it will sit at a lithium site much more readily because of the closely matched radii. Even its 3+ charge state has a large ionic radius compared to Al^{3+}, so the Li^+ site would seem to be favored. Also, if Fe^{2+} sits at an aluminum site, it will act as a hole trap under ionizing radiation, giving up an electron so it can change to the 3+ oxidation state. That means that both Center A and the 11-line spectrum would both be hole traps, and there would be a large and unknown electron trapping defect, or several smaller electron trapping defects. Fe^{2+} sitting at both isolated lithium and aluminum sites would compensate each other, but x ray irradiation would then produce easily observable spectra from both Fe^+ and Fe^{3+} of the same order of magnitude, which is not observed. Taking into account that only one line is observed with ionizing radiation, along with the information in Table 5.4,

indicates that Fe^{2+} preferentially migrates to lithium sites.

Out of the other possible iron group transition-metals that are likely to be impurities in the $LiAlO_2$ crystal, Sc, V, Mn, Co, and Cu can be dismissed. 100% of their stable isotopes have $I \geq 3/2$, and would therefore display distinct and strong hyperfine splittings which are not observed. Ti and Zn were shown to be an order of magnitude smaller in concentration than Fe from the elemental impurity analysis conducted by Auvray-Gely *et al* [25]. The location of an EPR line from Cr^{3+} has already been reported at $\approx 180\,\mathrm{mT}$ by Yamaga *et al* [26]. That leaves Ni as the last alternative transition-metal that could give rise to a signal similar to Center A in its $3d^7$ 3+ charge state. If Ni^{3+} is formed after irradiation, then it would have existed as either Ni^{2+} or Ni^{4+} prior to irradiation. Ni^{2+} has an effective ionic radius of 55 pm which is too large to sit on the Al^{3+}. It would be a hole trap even if it did, and Center A has already been ruled out as a hole trap. If it sat on the Li^{+} site, then it would trap an electron and convert to Ni^{+} after irradiation, which is a $3d^9$ configuration. That leaves the possibility of Ni^{4+} trapping an electron on the Al^{3+}. While Ni^{3+} cannot be ruled out entirely without further research, lithium aluminate samples from ten different plates supplied by MTI were investigated and Center A was the strongest impurity line after x ray irradiation in all but one sample. Fe is the most abundant transition-metal in the world, and should on average, show up as a trace impurity in a metal oxide in larger concentrations than nickel. Auvray-Gely *et al*, for example, showed a nickel concentration half that of iron [25].

From the preceding arguments, the evidence would indicate that iron is inadvertently introduced into lithium aluminate crystals during growth and exists in the 2+ charge state. The Fe^{2+} ions act as charge compensators for lithium vacancies and sit at either isolated lithium sites or lithium sites adjacent to a lithium vacancy. With the introduction of ionizing radiation, the Fe^{2+} ions will trap an electron that was

lost to the conduction band by an O^{2-} ion adjacent to a lithium vacancy (the 11-line hole trap). This process can be summarized as

$$(1)\ h\nu + O^{2-} \rightarrow O^{-} + e^{-} \tag{5.7}$$

$$(2)\ Fe^{2+} + e^{-} \rightarrow Fe^{+}. \tag{5.8}$$

EPR investigations of iron in ternary oxides with similar crystal structures as $LiAlO_2$ seem to be non-existent from literature searches using Thomson Reuters Web of Science, but much has been published on the EPR behavior of iron in binary compounds such as the alkali-earth oxides and alkali-halides. In NaF, NaCl, KCl, MgO, and LiCl, EPR lines from Fe^{+} are observed at temperatures below approximately 20 K. This is the same behavior observed for Center A. In these crystals, iron sits on the cation site in the 2+ charge state and no EPR signals from iron are visible before receiving ionizing radiation, again, just as in $LiAlO_2$. While Fe^{+} in these compounds is normally in octahedral coordination and exhibits an isotropic g, there exists variants of this defect in some of these materials due to nearest neighbor cation vacancies that result in the Fe^{+} ion experiencing orthorhombic or monoclinic local symmetry. These distortions can change the coordination in the local region of the defect to tetrahedral, which then allows comparisons to $LiAlO_2$. Table 5.5 shows a comparison between **g**

Table 5.5. Comparison of Center A spin-Hamiltonian parameters from Table 5.1, with those reported for Fe^{+} in select materials.

Host	Symmetry	g_x	g_y	g_z	Reference
NaF	Orthorhombic	4.585	2.029	5.792	[114]
NaCl	Orthorhombic	4.222	2.630	6.135	[121]
LiCl	Orthorhombic	4.365	2.722	5.702	[122]
KCl	Monoclinic	3.1823	1.9084	7.121	[123]
$LiAlO_2$	Tetragonal	3.6301	2.1232	5.1401	This work

matrix parameters for Center A and Fe^{+} substitutional impurities in some of these

binary compounds. A correlation between the g values can clearly be seen, providing another indicator that Center A is in fact an Fe^{+} ion.

5.5 Thermoluminescence Results

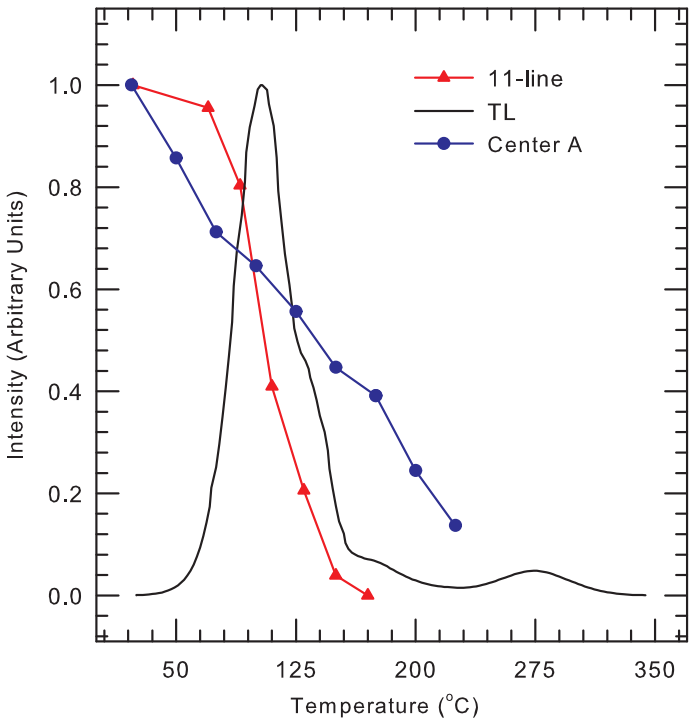

Figure 5.5. Thermal anneal data for the Center A EPR signal has been added to the data from Figure 4.9. The fact that Center A anneals away at a higher temperature indicates there are other electron and hole traps at work.

Figure 5.5 shows the same data from Figure 4.9 with the addition of the anneal curve of the Center A EPR signal. The conclusion drawn from this figure is that since Center A doesn't go to zero around 105 °C, the 11-line trapped hole is most likely releasing its holes to recombine at trapped-electron sites. Since Center A has half as many spins as the trapped-hole center, there must be other electron trapping sites that are playing a role in recombination, either some of the smaller signals seen in Figures 5.1 and 5.2, or transition-metals in charge states that are not paramagnetic. Also, since the trapped-hole disappears at 105 °C while Center A remains, there must

be other trapped hole sites as well; either some of the less intense EPR signals or non-paramagnetic species.

VI. Characterization of Copper-Diffused $LiAlO_2$

6.1 Introduction

Lithium aluminate is currently being investigated for radiation-detection applications involving OSL and thermoluminescence TL by different researchers [5–10, 100, 124, 125]. Copper-doped $LiAlO_2$ has been shown to have a large OSL response that is comparable to the commercially available OSL dosimeter material Al_2O_3:C, as well as increased sensitivity [10]. In this chapter, the fundamental mechanisms responsible for OSL in $LiAlO_2$ have been investigated. The strength of the OSL response depends in general on the nature of the active electron and hole traps in a material [70,72]. An OSL response from copper-diffused $LiAlO_2$ crystals was observed to be approximately 100 times larger than in as-grown crystals. Optical absorption, PL, PLE, and EPR were used to experimentally identify the electron and hole traps participating in the OSL. During an x ray irradiation at room temperature, Cu^+ ions sitting at Li^+ sites will trap holes and form Cu^{2+} ions. At the same time, Fe^{2+} ions that sit at Li^+ sites will trap electrons and form Fe^+, giving rise to the Center A EPR line discussed in Chapter 5. OSL occurs when trapped electrons are optically released from Center A and recombine with the holes at the Cu^{2+} ions.

Samples of $LiAlO_2$ from MTI cut from the same *c*-plates in the same dimensions as in Chapters 4 and 5 were subjected to copper diffusion at high temperature. The samples were wrapped in a single layer of thin (0.0125 mm thick) copper foil and placed into a one-zone tube furnace operating at 900 °C in flowing nitrogen gas. The wrapped sample was held at this temperature for 2 hours, and then was quickly cooled to room temperature within 2 minutes. With this process, copper enters the crystal as Cu^+ ions and occupies Li^+ sites. Nitrogen gas was used because during preliminary anneals in air, a very complicated Cu^{2+} EPR spectrum was seen in the as-annealed

crystal that behaved very differently from the behavior described in section 6.5. It is suspected that diffusion in air allows copper oxides to form on the surface of the crystal as well as replacing Li^+ ions in the bulk of the crystal, as there were three additional copper EPR spectra observed in addition to the "normal" Cu^{2+} spectra described in section 6.5. The flowing nitrogen gas allows copper to diffuse into the crystal without reacting with oxygen to form these surface complexes.

From the intensities of the EPR signals, the total concentration of Cu^{2+} ions produced during a room temperature x ray irradiation of the Cu-diffused crystal is estimated to be approximately $1.3 \times 10^{18}\,cm^{-3}$ using equation (3.2). The majority of copper ions that enter the crystal remain in the non-paramagnetic Cu^+ charge state after x ray irradiation, because the creation of Cu^{2+} is limited by the number of available electron traps and competition from other hole-trapping defects like the 11-line trapped-hole center discussed in Chapter 4. Therefore, the total amount of copper in the crystal is most likely 10 to 100 times greater than the Cu^{2+} estimate. Also, the uniformity of copper diffusion was not measured in this study. Although the following sections details the results of experiments with one copper-diffused crystal, similar behavior was observed with $LiAlO_2$ samples cut from different boules and diffused with copper at high temperature.

6.2 Optical Absorption Results

Optical absorption data was taken at room temperature using the Cary-5000 with unpolarized light propagating along the [001] direction in a two-sides polished crystal. The optical path length was 0.5 mm and corrections were made for reflective losses using equation (4.4) under the same principles as discussed in section 4.5.

Figure 6.1 shows the optical absorption spectra that were obtained. In Figure 6.1, spectrum (a) was taken from an as-grown reference crystal and shows that there

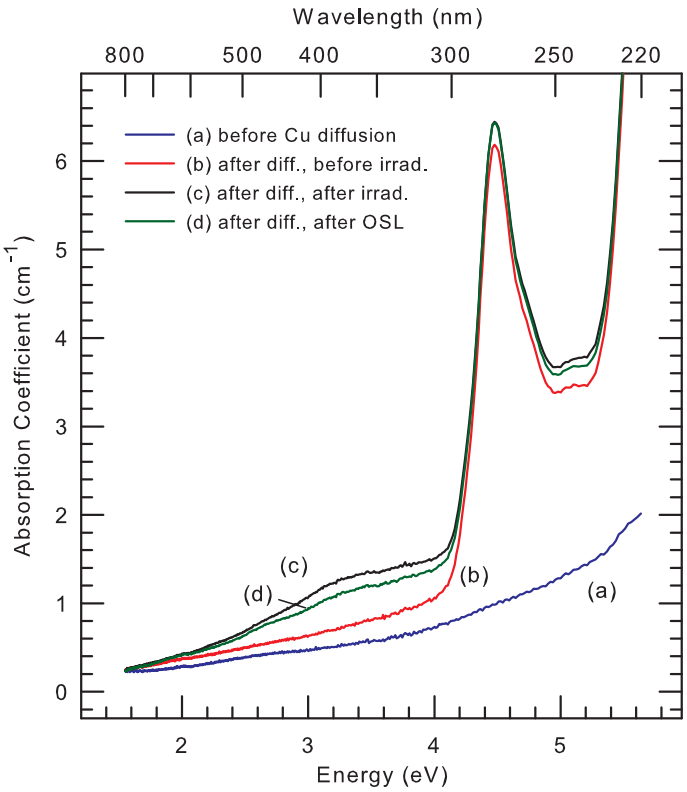

Figure 6.1. Optical absorption spectra from $LiAlO_2$ crystals taken at room temperature with unpolarized light propagating along the [001] direction. (a) As-grown reference crystal with no diffused copper. (b) After Cu diffusion but before x ray irradiation. (c) After Cu diffusion and after 60 kV, 30 mA generated x ray irradiation (d) After diffusion and after exposure to 425 nm OSL stimulation light.

were no major absorption bands present prior to copper diffusion. Spectrum (b) was taken from the sample that had been copper-diffused at 900 °C; spectrum (c) was taken after the copper-diffused sample was exposed to 60 kV, 30 mA x rays at room temperature; spectrum (d) was taken after exposing the x ray irradiated crystal to 425 nm OSL stimulation light for 300 s. As shown in Figure 6.1(b), the copper diffusion introduces a well-defined absorption band with a peak near 277 nm that has a partially resolved shoulder on its short-wavelength side. This peak is due to Cu^+ ions occupying Li^+ sites; Cu^{2+} and Cu^+ have effective ionic radii of 57 and 60 pm respectively, making them well suited to replace a Li^+ ion with its 59 pm effective ionic radius [120]. Similar absorption bands have also been observed in wide-band

gap insulators and are attributed to the $3d^{10}$ to $3d^9 4s^1$ intracenter transition of the Cu^+ ion [126–128]. The intense optical absorption at wavelengths shorter than 225 nm seen in spectra (b), (c), and (d) after copper diffusion is clearly associated with the introduction of copper into the crystal as it doesn't appear in the as-grown spectrum (a). This absorption is most likely a result of transitions to higher energy levels of the Cu^+ ion.

As shown in spectra (c) and (d), the x ray irradiation at room temperature introduces an absorption band peaking near 379 nm, with a tail extending into the visible beyond 500 nm, while having only a slight effect on the band at 277 nm. The difference in behavior between the 379 nm and 277 nm bands can be attributed in part to different oscillator strengths for the two optical absorption bands. The 379 nm band is the same band seen in Figure 4.8(b) for a nominally undoped as-grown $LiAlO_2$ crystal that had been exposed to x rays at room temperature. This band is caused by absorption from Center A (i.e., Fe^+), and the EPR results of Section 6.5 support this assignment. The spectrum in Figure 6.1(d) was taken after the 425 nm OSL stimulation light removed some of the trapped electrons from Center A, which accounts for the decrease in intensity of the 379 nm absorption band. The reason the OSL stimulation light does not completely eliminate the 379 nm absorption band is discussed in Section 6.5.

6.3 Photoluminescence Results (PL and PLE)

Figure 6.2 shows the photoluminescence (PL) and photoluminescence excitation (PLE) spectra obtained from the copper-diffused sample using the Fluorolog-3 by Horiba Scientific. The spectra were collected at room temperature with the PL emission band peak at 359 nm (3.45 eV) and the corresponding PLE band peak at 273 nm (4.54 eV). The Stokes shift is 1.09 eV, the full width at half maximum (FWHM) of

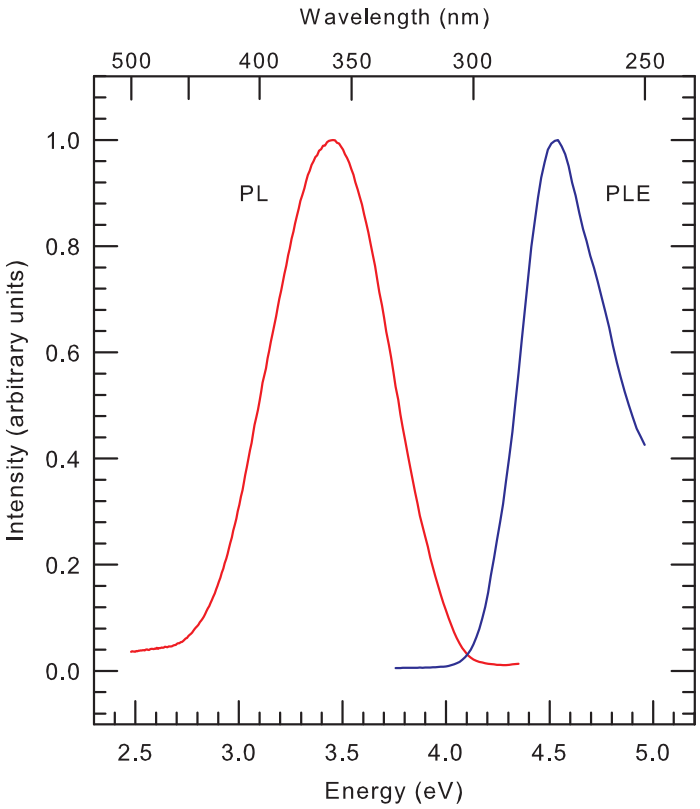

Figure 6.2. PL and PLE spectra obtained at room temperature from Cu^+ ions in a copper-diffused $LiAlO_2$ crystal. The PL spectrum was taken with 270 nm excitation light and the PLE spectrum was obtained by monitoring the emission at 360 nm.

the PL band is 0.68 eV, and the FWHM of the PLE band is 0.55 eV. The shape of the PL band is well described by a single Gaussian, while the PLE band requires more than one Gaussian because of the distinct shoulder visible on its high energy side. The shape of the PL emission band did not change as the excitation wavelength was varied from 250 to 290 nm, and the shape of the PLE band did not change as the emission monitoring wavelength was varied from 340 to 380 nm. This would indicate that the PL band in Figure 6.2 is a single band representing one recombination process instead of several overlapping bands.

The PL and PLE bands were not observed in the reference crystal. However, during early tests of nominally undoped $LiAlO_2$ crystals, these PL and PLE bands

were observed but at an intensity 2-3 orders of magnitude less than the copper-diffused sample. This would suggest that copper is introduced unintentionally during growth and indeed, Auvray-Gely *et al* reported 2 parts per million (2 ppm) Cu impurities in their elemental analysis of nominally undoped $LiAlO_2$ crystals [25]. This is an important reminder for researchers that very small quantities of impurities can have measurable effects on the properties of "pure" crystals.

The peak of the PLE band occurs at close to the same position as the peak of the intense absorption band in Figure 6.1 (273 nm vs. 277 nm). The difference is experimental and arises primarily from attempting to precisely correct the PLE spectrum for variations in the excitation lamp intensity. The close agreement in wavelength strongly suggests that the absorption band and the PLE peak have a common origin; specifically the $3d^{10}$ to $3d^9 4s^1$ intracenter transition of a Cu^+ ion. The PL emission would then be from an excited electron undergoing $3d^9 4s^1$ to $3d^{10}$ transitions in the Cu^+ ion. Fujimoto *et al* [6] has previously assigned PL and PLE bands from $LiAlO_2$:Cu crystals that are very similar to those shown in Figure 6.2 to Cu^+ ions substituting for Li^+ ions. Also, similar PL and PLE bands have been reported in other wide-band gap insulators with monovalent copper impurity ions such as LiCl [129], NaI [130], and $Li_2B_4O_7$ [131–133].

6.4 Optically Stimulated Luminescence Results

A significant OSL response was observed in the copper-diffused $LiAlO_2$ crystal after exposing it to x rays at room temperature. Figure 6.3 shows a typical OSL decay curve taken with the Fluorolog-3 spectrometer operating in the kinetics mode. The excitation light was set at 425 nm while emission was monitored at 360 nm. In general OSL decay curves are non-exponential [72], and this was confirmed for the decay curve in Figure 6.3 when plotted on a logarithmic scale. The OSL response

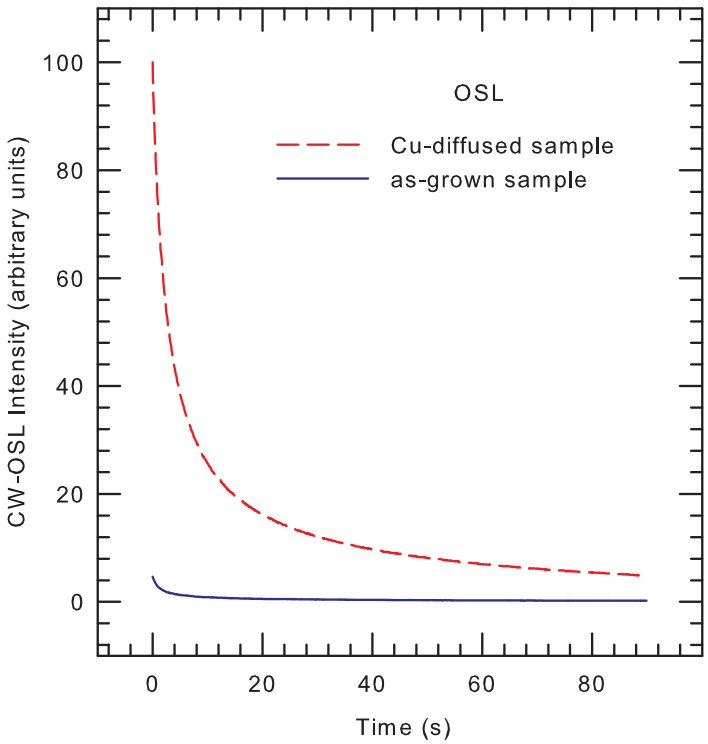

Figure 6.3. OSL response obtained at room temperature from a copper-diffused $LiAlO_2$ crystal. The excitation light was at 425 nm and the monitoring light was 360 nm. Also shown is the OSL response from the as-grown reference crystal with no copper diffusion.

from the reference crystal obtained under identical conditions, also shown in Figure 6.3, is approximately 10 times weaker than the copper-diffused signal.

The starting intensity of the OSL response (i.e., the intensity just after $t = 0$) from the copper-diffused $LiAlO_2$ crystal decreased as the stimulation wavelength was changed from 425 to 500 nm, which suggests that wavelengths closer to 400 nm are more effective in producing OSL emission than wavelengths near 500 nm. This behavior directly correlates the OSL wavelength response to the optical absorption spectrum of the copper-diffused crystals after x ray irradiation. As shown in Figures 6.1(c) and (d), the low-energy side of the broad 379 nm absorption band is decreasing in this 400 to 500 nm range. The 379 nm band is due to Fe^+ absorption from Center A, and excitation into this band ionizes the Fe^+, releasing an electron to participate in OSL luminescence. As the band decreases in the 400 to 500 nm region, ionization becomes

less effective, and therefore the OSL response decreases.

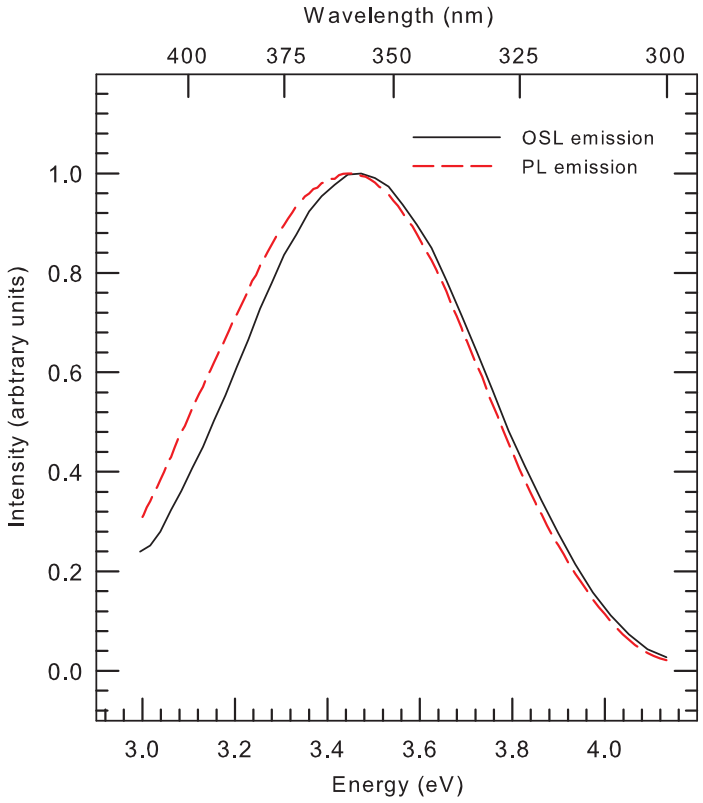

Figure 6.4. Spectral dependence of the OSL emitted light from the copper-diffused $LiAlO_2$ crystal. The peak in the OSL emission is at 357 nm. The PL emission curve from Figure 6.2 is included for comparison.

The solid curve in Figure 6.4 displays the spectral dependence of the OSL emission. The spectral dependence was obtained using the Fluorolog-3 by having the emission monochromator repeatedly scan from 300 to 410 nm, as the OSL signal was decaying as a function of time during stimulation with 450 nm light. Each scan took 6.5 s, therefore 20 scans were recorded as the OSL decayed over a period of 130 s. No significant change in the wavelength dependence was revealed during this series of scans, which suggests that the recombination site remains the same during OSL decay. The specific curve shown in Figure 6.4 was taken 4 s after initial exposure of the crystal to stimulation light. The OSL emission peak is at 357 nm (3.47 eV) with a FWHM of 0.63 eV, and is very close to the same values as the PL emission peak from Figure 6.2,

shown as the dashed curve in Figure 6.4. This leads to the unavoidable conclusion that the PL and OSL have a common origin; a Cu recombination site is responsible for both PL and OSL emissions in copper-diffused $LiAlO_2$ crystals. The slight differences in the two emission curves are attributed to small changes in the method of collecting the data, and are not believed to be fundamental in nature. A few research groups have attributed the presence of oxygen vacancies to observed optical phenomena in $LiAlO_2$ doped with transition-metals [134, 135] and rare-earths [100, 136], thus far, there is no experimental evidence to suggest that oxygen vacancies are involved in the OSL response of copper-diffused $LiAlO_2$ crystals.

As discussed in Section 6.3, nominally undoped $LiAlO_2$ samples may contain residual amounts of Cu^+ impurities. This unintentionally introduced copper could cause a small, but observable OSL response. That is most likely why the reference crystal in Figure 6.3 shows a significantly weaker OSL response than the copper-diffused crystal. The x ray irradiated undoped $LiAlO_2$ crystal used to measure absorption in Figure 4.8 also has a peak near 277 nm, which gives more credence to the idea that Cu impurities can be present and have a measurable effect in nominally pure crystals.

6.5 Electron Paramagnetic Resonance Results

Figure 6.5 shows two EPR spectra taken from the copper-diffused $LiAlO_2$ crystal. These data were obtained at 28 K with the magnetic field along the [001] direction. Figure 6.5(a) was recorded after the crystal was irradiated at room temperature with x rays. Before the irradiation, there were no significant EPR signals in this region of magnetic field. Three trapped-hole centers are produced by the x rays. The set of 11 equally spaced, but not equally intense, lines in the region between 326 and 336 mT has been assigned to a hole localized on an oxygen ion adjacent to a lithium vacancy, as detailed in Chapter 4. The other two sets of lines in Figure 6.5(a) are assigned

to x ray-induced Cu^{2+} ions (i.e., Cu^{2+} ions are formed during the irradiation when holes are trapped at Cu^{+} ions occupying Li^{+} sites). These two Cu^{2+} EPR spectra in $LiAlO_2$ have not been previously reported in the literature.

Stick diagrams above Figure 6.5(a) identify individual lines associated with each of the new Cu^{2+} centers. EPR spectra of Cu^{2+} ions are easily recognized by their hyperfine patterns caused by the two stable copper isotopes (^{63}Cu is 69.2% abundant with $I = 3/2$ and ^{65}Cu is 30.8% abundant with $I = 3/2$). Because of the $I = 3/2$ nuclear spins, sets of four-line hyperfine patterns are observed. The ^{65}Cu nuclei have a slightly larger magnetic moment than the ^{63}Cu nuclei, which explains why the separations among the four lines for ^{65}Cu are a little larger than the separations among the four lines for ^{63}Cu. Direct evidence verifying that these new sets of lines in Figure 6.5(a) are due to Cu^{2+} ions comes from the lines at highest and lowest magnetic fields, where the two isotopes are clearly resolved. The more widely spaced set of copper-related lines (the blue stick diagrams) is assigned to a Cu^{2+} ion at a Li^{+} site with an adjacent Li^{+} vacancy (i.e., a Cu^{2+}-V_{Li} center). The other set of copper-related lines (the red stick diagrams) is assigned to isolated Cu^{2+} ions (i.e., Cu^{2+} ions at Li^{+} sites with no defects nearby). With the magnetic field along the [001] direction, the g values for the isolated Cu^{2+} center and the Cu^{2+}-V_{Li} center are 1.943 and 1.976, respectively. A primary reason for assigning the two spectra in Figure 6.5(a) to an isolated Cu^{2+} ion and a Cu^{2+} ion next to a Li^{+} vacancy comes from $Li_2B_4O_7$ crystals where two similar Cu^{2+} defects have been reported [137]. A slight amount of confusion was initially encountered when attempting to make assignments for the EPR spectra in Figure 6.5(a) because the highest field lines (near 367 mT) from each Cu^{2+} center directly overlap. Once this overlap was recognized, the two Cu^{2+} sets of hyperfine lines were easily distinguished (as illustrated by the stick diagrams). In terms of "effective" charges relative to the regular lattice, the isolated Cu^{2+} centers (red) have

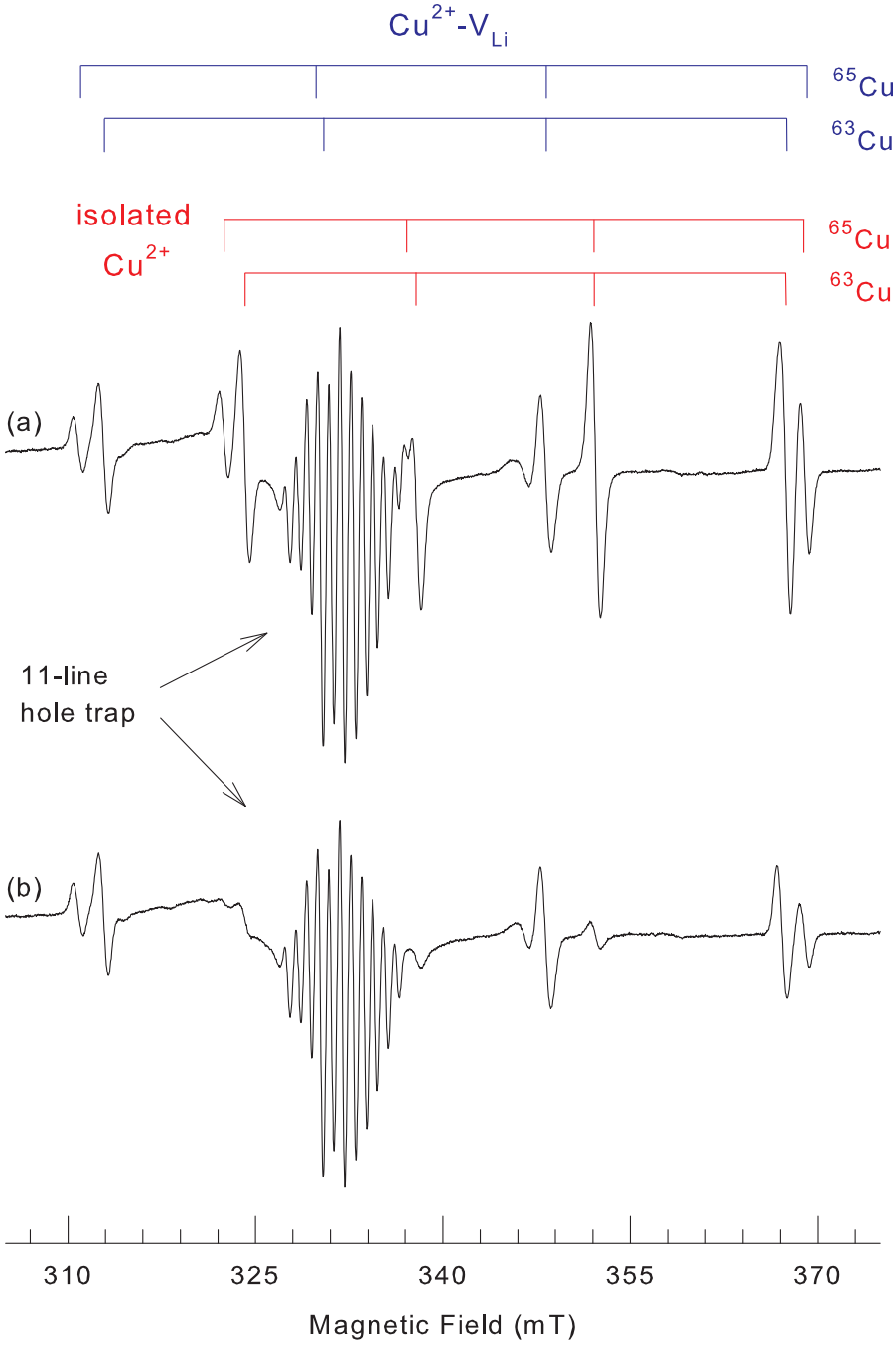

Figure 6.5. EPR spectra of Cu^{2+} ions produced by x rays in a copper-diffused $LiAlO_2$ crystal. These data were taken at 28 K with the magnetic field along the [001] direction and a microwave frequency of 9.401 GHz. (a) Spectrum taken after irradiating at room temperature with x rays, but before OSL. (b) Spectrum taken after exposure to OSL stimulation light (425 nm) at room temperature.

a positive charge and the Cu^{2+}-V_{Li} centers (blue) are electrically neutral. Trapped-hole centers represented by the 11-line spectrum in Figure 6.5 are also neutral defects (Chapter 4).

After obtaining the post-irradiation EPR spectrum in Figure 6.5(a), the OSL response of the copper-diffused crystal was recorded at room temperature using a stimulation wavelength of 425 nm. This emptied the OSL-active traps. Then the EPR spectrum in Figure 6.5(b) was taken at 28 K with the magnetic field along the [001] direction. Comparing Figure 6.5(a) with Figure 6.5(b) shows that the isolated Cu^{2+} centers (identified by the red stick diagrams) were nearly eliminated by the OSL stimulation light and thus are shown to be a major participant in the OSL process. The other two trapped-hole centers, specifically the Cu^{2+}-V_{Li} centers (identified by the blue stick diagrams) and the 11-line Li-vacancy-associated centers, did not change significantly during the exposure to the OSL stimulation light, and thus are not participants in the OSL response of the crystal. Optimizing the OSL signal will require maximizing the concentration of isolated Cu^{2+} ions formed by the ionizing radiation.

The identity of the electron trap participating in the OSL process was revealed to be the Center A Fe^{+} signal with the aid of EPR. The Center A EPR line near 141.5 mT (with a microwave frequency of 9.401 GHz) was observed in both as-grown and copper-diffused $LiAlO_2$ crystals after an x ray irradiation at room temperature. This signal is shown by the solid line in Figure 6.6.

As discussed in Chapter 5, the EPR spectrum in Figure 6.6 is not present in our as-grown $LiAlO_2$ crystals prior to x ray irradiation. This indicates that the Fe impurities are initially present as Fe^{2+} ions substituting for Li^{+} ions and serve as the primary charge compensator for the large number of Li^{+} vacancies known to be present in the as-grown $LiAlO_2$ crystals (Chapter 4). These Li^{+} vacancies may be

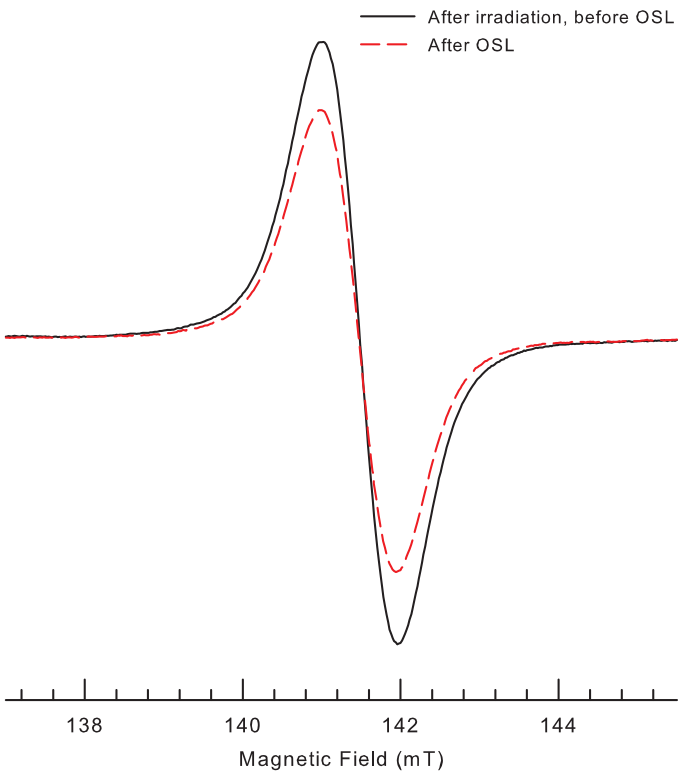

Figure 6.6. EPR spectra from radiation-induced Fe^{+} ions in a copper-diffused $LiAlO_2$ crystal. These data were taken at 15 K with the magnetic field along the [001] direction and a microwave frequency of 9.401 GHz. (a) Solid line taken after irradiating at room temperature with x rays but before OSL. (b) Red dashed line taken after exposure to OSL stimulation light (425 nm).

non-locally compensated by distant Fe^{2+} ions or they may have an Fe^{2+} ion at an adjacent Li^{+} site. Although the Center A EPR spectrum in Figure 6.6 is assigned to trapped electrons in the form of Fe^{+} ions, it is not known if these Fe^{+} ions are adjacent to Li^{+} vacancies. A more detailed analysis of the angular dependence of the Center A EPR spectrum in the future may answer this question. (It does not appear that oxygen vacancies provide charge compensation for lithium vacancies in as-grown crystals; as discussed in Chapter 7, neither F or F^{+} center optical absorption bands are seen in as-grown $LiAlO_2$)

As shown in Figure 5.1(b) and by the more intense EPR spectrum (solid curve) in Figure 6.6, Fe^{+} ions are formed when Fe^{2+} ions initially present in the $LiAlO_2$ crystal

trap an electron during exposure to ionizing radiation. The less intense spectrum (dashed red curve) in Figure 6.6 was taken after exposing the x ray-irradiated crystal to 425 nm OSL stimulating light for 300 s. This light reduced the Center A EPR spectrum by nearly 25% as a large photoionization cross-section for the Fe^{+} ions allows the stimulating light to efficiently release electrons. (In Figure 6.1, the 379 nm absorption peak in spectrum (d) also decreased by about 25% after exposure to 425 nm OSL stimulating light.) The optically released electrons recombine with holes at the isolated Cu^{2+} ions. All of the Fe^{+} ions represented by the solid line spectrum in Figure 6.6 are not expected to release electrons by OSL stimulating light. There are two hole centers (the 11-line hole center and the Cu^{2+}-V_{Li} center) produced by the x rays that are not significantly affected by OSL stimulation light, as seen in Figure 6.5(b). These centers represent more than half of the total trapped holes in Figure 6.5(a), with isolated Cu^{2+} centers accounting for the remaining trapped holes. The 11-line and the Cu^{2+}-V_{LI} trapped-hole centers are neutral defects and have smaller cross-sections for electron capture than positively charged isolated Cu^{2+} ions. This means that optically released electrons from Fe^{+} ions will recombine at lower rates with these neutral trapped-hole centers, and thus explains a lack of significant change in the intensities of the 11-line hole center and the Cu^{2+}-V_{Li} center in Figure 6.5(b) when most of the isolated Cu^{2+} centers are accepting electrons. It is also expected that many of the optically released electrons will be retrapped by Fe^{2+} ions. Because of the neutral hole traps and retrapping, the number of Fe^{+} ions in Figure 6.6 is only partially reduced when the x ray-irradiated crystal is briefly exposed to OSL stimulation light.

6.6 Summary

Optimizing a material for optically stimulated luminescence (OSL) applications requires the following information: (1) the identities of the participating trapped-electron and trapped-hole centers introduced during an exposure to radiation, (2) the spectral dependence (i.e., the peak position and shape) of the absorption band that allows the stimulation light to initiate the OSL recombination process, and (3) the recombination site and the spectral dependence of the emitted light. This chapter has addressed these three points. Lithium aluminate ($LiAlO_2$), doped or diffused with copper, has been shown to produce a large optically stimulated luminescence (OSL) signal. The participating defects initially present in the material are Cu^+ ions and Fe^{2+} ions, both on Li^+ sites. During an irradiation, the Cu^+ ions trap holes and become Cu^{2+} ions and the Fe^{2+} ions trap electrons and become Fe^+ ions. The Fe^+ ions have a broad optical absorption band peaking near 379 nm with a tail extending beyond 500 nm. Stimulation light with wavelengths in this Fe^+ band releases electrons, which then recombine with holes at the Cu^{2+} ions and form Cu^+ ions in a short-lived excited state, i.e., $(Cu^+)^*$ ions. The OSL emitted light with a peak near 357 nm is characteristic of the radiative decay of these $(Cu^+)^*$ ions and is the same as the photoluminescence observed from intracenter excitations of Cu^+ ions in $LiAlO_2$. The following is a summary of the OSL process in Cu-doped $LiAlO_2$.

(1) Irradiation step $\quad e^- + Fe^{2+} \rightarrow Fe^+ \quad$ and $\quad h^+ + Cu^+ \rightarrow Cu^{2+}$

(2) Stimulation step $\quad Fe^+ + h\nu$ (425 nm absorption)$\rightarrow Fe^{2+}$ + released e^-

(3) Emission step $\quad$ released $e^- + Cu^{2+} \rightarrow (Cu^+)^* \rightarrow Cu^+ + h\nu$ (357 nm emission)

In conclusion, these results suggest that $LiAlO_2$ containing an appropriate combination of Cu^+ ions, Fe^{2+} ions, and lithium vacancies will be a useful OSL material. To be active in OSL, the Cu^+ ions must be on Li^+ sites and isolated from other defects.

(It is important to note that not all of the Cu^{+} ions in a sample may be in these isolated sites.) The Fe^{2+} ions must also occupy Li^{+} sites with charge-compensating Li^{+} vacancies nearby or at more distant sites. These compensating Li^{+} vacancies are an important defect in OSL-active Cu-diffused $LiAlO_2$ material. If there are no Li^{+} vacancies, Fe^{2+} ions are not expected to be present on Li^{+} sites and thus there would be no defects to trap electrons during an exposure to ionizing radiation (even though the crystal may contain Fe ions in other valence states and possibly at different sites). Once an appropriately co-doped $LiAlO_2$ sample (with copper and iron) is available, optimum OSL monitoring wavelengths are expected to be between 330 and 390 nm and optimum stimulation wavelengths are expected to be between 400 and 450 nm.

VII. Characterization of Neutron-Irradiated $LiAlO_2$

7.1 Introduction

If $LiAlO_2$ is to be utilized in applications that involve exposure to neutron irradiation, then an understanding of the point defects that are created by neutron collisions is critically important. Oxygen ions will be displaced by neutron collisions leaving behind oxygen vacancies, and for oxide crystals, the oxygen vacancy is the most fundamental and extensively studied point defect. Oxygen vacancies are important in oxides because they can effect the properties and performance of a material, and should be expected to produce effects in neutron-irradiated $LiAlO_2$. In the role of lithium aluminate as a tritium breeder material for example, it has been known for some time that it is challenging to efficiently extract tritium from the breeder material [4,138]. It is possible that the trapping of tritium ions at oxygen vacancies causes a decrease in the recoverable yield of tritium. It is well established that hydrogen, in the form of H^- or H^{2-} ions, can be stably trapped in oxygen vacancies in MgO and ZnO [139–142]. Analogous tritium-trapping behaviors may be occurring with oxygen vacancies in neutron-irradiated $LiAlO_2$.

In this chapter, oxygen vacancies with one trapped electron (F^+ centers or V_O^+ centers) and aluminum vacancies produced after irradiation of single crystals of $LiAlO_2$ with high-energy neutrons are investigated. These F^+ centers are responsible for an optical absorption band peaking near 238 nm and an electron paramagnetic resonance (EPR) spectrum showing resolved hyperfine structure from the two ^{27}Al ions neighboring the vacancy. A metastable state of the F^+ center is also identified which occurs because of an asymmetrical sharing of the unpaired spin between the two Al^{3+} ions neighboring the vacancy. There are two similar "ground" states that are distinguished by which of the Al ions has the greater unpaired spin density. One state has

a slightly higher energy and is therefore metastable. Exposing the neutron-irradiated crystal to ultraviolet light converts a few of the F^+ centers to F centers, i.e., vacancies with two trapped electrons. The F centers have an optical absorption band that peaks at 272 nm. Photoluminescence (PL) and photoluminescence excitation (PLE) bands from the F centers peak near 416 and 277 nm, respectively.

Also in this chapter, the observation of doubly ionized ($S = 1/2$) aluminum vacancies produced during neutron irradiation is discussed. These defects consist of one hole trapped on an oxygen ion adjacent to the aluminum vacancy. The 11-line trapped-hole EPR spectrum discussed in Chapter 4 is not observed from neutron-irradiated samples, even after a subsequent exposure to x rays. This would indicate that the lithium vacancies that are present in as-grown $LiAlO_2$ crystals are no longer serving as a simple trap for radiation-induced holes. The most likely reason is the lithium vacancies have trapped oxygen interstitials during the neutron irradiation. A similar trapping of oxygen interstitials by isolated magnesium vacancies has been reported in neutron-irradiated MgO [143].

Undoped c-plate single crystals of $LiAlO_2$ were obtained from MTI and cut into 3 $\times$ 3 $\times$ 0.5 mm^3 pieces. Several samples were irradiated with neutrons using the central irradiation facility (CIF) at the Ohio State University Nuclear Reactor Laboratory (Columbus, Ohio). This is a pool-type reactor that operates at a maximum power of 450 kW. One sample was held in the CIF for 3 hours and another sample was held in the CIF for 1.5 hours. Similar spectroscopic results were obtained from both samples except the 1.5 hour sample produced less intense spectra than the 3 hour sample in all cases. In the CIF, the total neutron flux was $\approx 2.1 \times 10^{13}$ $\frac{\text{neutrons}}{\text{cm}^2\text{s}}$ and the thermal neutron flux was $\approx 1.4 \times 10^{13}$ $\frac{\text{neutrons}}{\text{cm}^2\text{s}}$. The sample temperatures were not measured during irradiation but are estimated to have remained below 150 °C.

7.2 Electron Paramagnetic Resonance Results

7.2.1 The F^+ Center.

Figure 7.1(a) shows the EPR spectrum obtained from the 3 hour neutron-irradiated lithium aluminate single crystal. The spectra were taken at 100 K with **B** along the [001] direction and approximately 20 μW of microwave power. As has been mentioned previously, prior to irradiation, there are no significant EPR signals in as-grown $LiAlO_2$ crystals; only a few weak lines from transition-metals can be seen. Figure 7.1(a) is really a combination of two different types of singly ionized oxygen vacancy EPR signals that are shown separately in Figures 7.1(b) and 7.1(c). The two oxygen vacancy spectra contain large numbers of partially resolved ^{27}Al hyperfine lines of similar intensity in the magnetic field region extending from 284 to 384 mT. The three intense lines that are cut off in the figure between 322 and 340 mT are from unrelated defects and they cover up a portion of the middle hyperfine lines from the F^+ centers. They will be discussed further in subsection 7.2.2. One of the two oxygen-vacancy spectra in Figure 7.1(a) is assigned to stable F^+ centers and the other is assigned to a metastable state of the F^+ centers (labeled F^{+*}). The concentration of defects was estimated from equation 3.2 to be 1.1×10^{19} cm^{-3}. Even though relatively large concentration of oxygen vacancies are present in the neutron-irradiated crystal, the EPR spectra are not easy to observe. The hyperfine lines from the F^+ and F^{+*} centers are broad ($\approx$ 2 mT) and easily saturate with microwave power. This is why the microwave power used is less than the 2 mW that was used for the 11-line trapped hole and the Cu^{2+} EPR signals. Each spectrum in Figure 7.1 is an average of 25 scans, which improves the signal-to-noise ratio by a factor of five.

The procedures that established the presence of two distinct oxygen-vacancy centers in Figure 7.1(a) are explained in the following steps. Figure 7.1(a) shows the spectrum immediately after neutron-irradiation. The neutron-irradiated crystal was

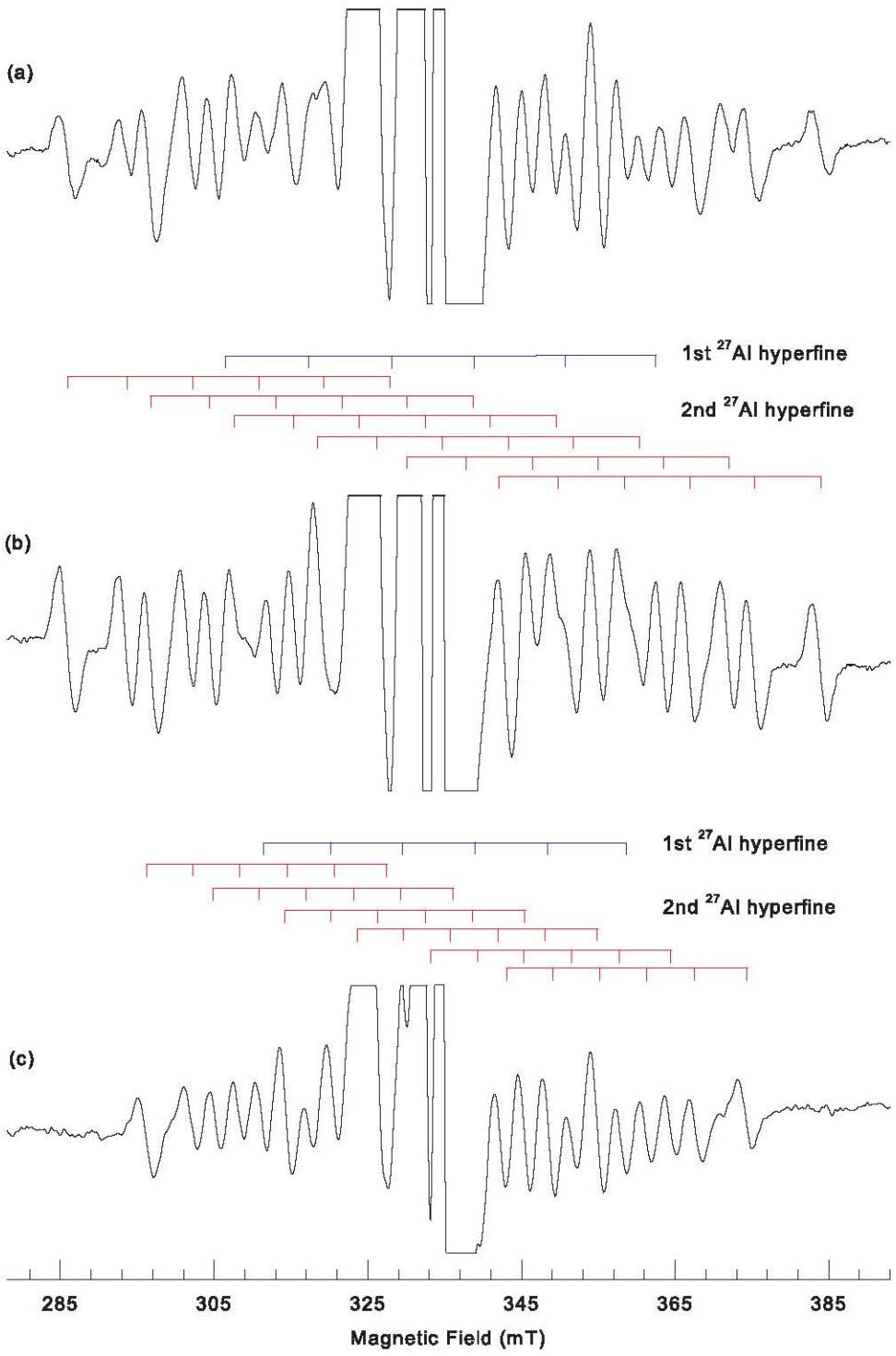

Figure 7.1. EPR spectra of oxygen vacancies in a neutron-irradiated $LiAlO_2$ crystal. Data were taken at $100\,K$ with the magnetic field along the [001] direction. Stick diagrams identify the hyperfine lines from the two ^{27}Al nuclei adjacent to the oxygen vacancy. (a) Spectrum with both F^+ and F^{+*} centers. (b) Spectrum of only the F^+ centers. (c) Spectrum of only the F^{+*} centers.

then held at 200 °C for 1 minute in a one-zone tube furnace. It was placed back into the EPR spectrometer and cooled down to 100 K where the EPR spectrum was taken again. Figure 7.1(b) shows the spectrum obtained after the anneal is entirely due to the F^+ center. In order to identify the lines from the second oxygen-vacancy center, Figure 7.1(b) was adjusted down in intensity until its highest-field line matched the intensity of the highest-field line in Figure 7.1(a). Figure 7.1(b) was then subtracted from Figure 7.1(a), producing the difference curve in Figure 7.1(c) which represents the spectrum from the metastable F^{+*} center. Both F^+ and F^{+*} centers are present in Figure 7.1(a), but the F^{+*} centers become thermally unstable below 200 °C. As they become unstable they convert over to the more stable F^+ centers, which are seen to increase in intensity in Figure 7.1(b) from their intensity in Figure 7.1(a) by the same amount as the F^{+*} centers that were converted.

The oxygen ion in $LiAlO_2$ is surrounded by two lithium and two aluminum ions. In the normal lattice, each of these four neighbors has a slightly different distance to the center of the oxygen ion. When the oxygen ion is missing, the lattice will undergo relaxation that will alter the cation distances from the unrelaxed values, but they will most likely remain unequal. For the paramagnetic vacancy, there will be an unequal sharing of the unpaired electron among the four cations, with more spin density at the Al^{3+} neighbors and less spin density at the Li^+ neighbors. Since the two Al^{3+} ions have inequivalent positions relative to the center of the oxygen vacancy, they will also have an unequal sharing of the spin density between them. In Figures 7.1(b) and 7.1(c), the hyperfine structure from the larger interactions with the adjacent ^{27}Al nuclei is easily resolved while no hyperfine structure is visible from the smaller interactions with the ^7Li nuclei as would be expected (the ^{27}Al are 100% abundant with $I = 5/2$ and the ^7Li are 92.5% abundant with $I = 3/2$). The blue stick diagrams with six lines in Figures 7.1(b) and 7.1(c) represent the hyperfine splitting from the

larger of the two ^{27}Al interactions (referred to in Figure 7.1 as the 1st ^{27}Al hyperfine). Each of the blue hyperfine-split lines is then further split into six red lines from the smaller ^{27}Al hyperfine interaction (referred to in Figure 7.1 as the 2nd ^{27}Al hyperfine). This results in 36 hyperfine lines from two ^{27}Al interactions. There is some overlap among these ^{27}Al lines and a few are hidden by the three larger unrelated lines in the middle of the spectra.

The EPR spectra of the F^+ and F^{+*} centers in Figures 7.1(b) and 7.1(c) were found to be nearly isotropic, and therefore each spectrum can be described approximately by a constant g value and two hyperfine parameters, one for each ^{27}Al neighbor. A spin Hamiltonian with an electron Zeeman term and two hyperfine terms was used to determine a set of values for these parameters for each center. The spin Hamiltonian is given by

$$\mathcal{H} = g\mu_B \hat{\mathbf{S}} \cdot \mathbf{B} + A_1 \hat{\mathbf{S}} \cdot \hat{\mathbf{I}}_1 + A_2 \hat{\mathbf{S}} \cdot \hat{\mathbf{I}}_2 \tag{7.1}$$

The comprehensive simulation software EasySpin was used to predict the positions of individual EPR lines for this spin Hamiltonian (where $S = 1/2$, $I_1 = 5/2$, and $I_2 = 5/2$) [144]. EasySpin converts the spin Hamiltonian in equation (7.1) to a 72×72 matrix and then performs a full diagonalization to obtain the energy levels. The input data were initial estimates for the g value, A_1 and A_2, the microwave frequency, and crystal structure data. The difference between the highest field line and the next two lines converted into MHz were used as initial estimates for A_1 and A_2. The g value and the hyperfine parameters were manually varied until a good fit was obtained. The parameters that resulted from the fitting routine are given in Table 7.1. Figure 7.2 shows the result of the EasySpin simulation with the F^+ EPR spectrum from Figure 7.1(b). Each oxygen vacancy EPR spectra is slightly asymmetrical because of second-order effects from the large hyperfine parameters. For example, in the F^+

Table 7.1. Spin-Hamiltonian parameters for the F^+ and F^{+*} centers in a neutron-irradiated $LiAlO_2$ crystal. These g and A values were obtained from the EPR spectra in Figures 7.1(b) and 7.1(c), taken with the magnetic field along the [001] direction. Estimates of uncertainties are ± 0.0005 for the g values and ± 2 MHz for the A values.

	F^+ center	F^{+*} center
g	2.0030	2.0030
A_1 for 1st ^{27}Al hyperfine	310 MHz	258 MHz
A_2 for 2nd ^{27}Al hyperfine	240 MHz	182 MHz

center spectrum in Figure 7.1(b), the highest two lines near 379 mT are separated by 8.62 mT while the lowest two lines near 289 mT are separated by 7.64 mT.

For F^+ centers in Al_2O_3 crystals, the measured g value is 2.0030 and the isotropic portions of the hyperfine interactions are 147.0 MHz for two of the ^{27}Al neighbors and 29.8 MHz for the other two ^{27}Al neighbors [145]. Table 7.1 shows that the g values for the F^+ and F^{+*} centers in lithium aluminate are the same as the g value of the F^+ center in Al_2O_3. The hyperfine interactions for the two ^{27}Al neighbors of the F^+ and F^{+*} centers in $LiAlO_2$ are, however, about a factor of two larger than the corresponding larger value for the F^+ center in Al_2O_3. The differences in the ^{27}Al hyperfine parameters for the two materials may be related to the distances from the center of the oxygen vacancy to the aluminum neighbors. The two closest Al^{3+} ions in Al_2O_3 are 1.855 Å from the vacant oxygen site while the Al^{3+} ions in $LiAlO_2$ are 1.755 and 1.766 Å from the vacancy. This smaller distance in $LiAlO_2$ is consistent with a larger unpaired spin density on the two Al^{3+} ions.

A possible explanation for the existence of two oxygen vacancy centers is unequal sharing of the unpaired spin density by the two ^{27}Al ions adjacent to the oxygen vacancy. The EPR spectra in Figures 7.1(b) and 7.1(c) do not provide information about which of the two Al^{3+} ions has the greater spin density, nor do they provide

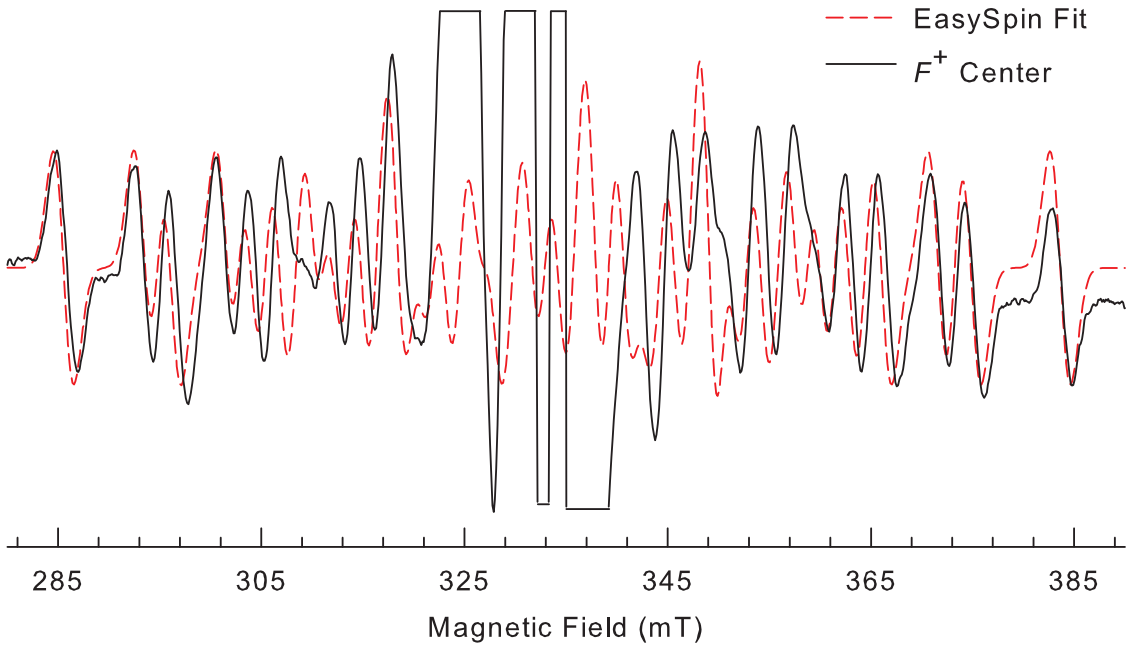

Figure 7.2. EasySpin simulation spectra with F^+ center EPR spectra from Figure 7.1(b). The parameters in Table 7.1 were obtained from the fit.

information about the relative lattice relaxations of the two ions. It is reasonable to assume, however, that the Al^{3+} ion that has a larger spin density in the F^+ center will have a smaller spin density in the F^{+*} center and vice versa, which then gives rise to two distinct distributions of the unpaired spin density for the singly ionized oxygen vacancies. Each of these configurations (i.e., the F^+ and F^{+*} centers) will be accompanied by its unique relaxation of the two Al^{3+} ions in the surrounding lattice. Presumably, the F^+ center minimum energy configuration is less than the F^{+*} center minimum energy configuration, and their potential wells are separated by a potential barrier. When the F^{+*} has sufficient energy to overcome this barrier, it is then able to convert to F^+ centers. Kurtz *et al* reported the EPR spectra of the F^+ center of Na, K, and Li-doped β-alumina after irradiation with 1.5 MeV electrons in 1981 [146]. They only observed one type of F^+ center with Na and K dopants, but reported seeing two types of F^+ centers with Li-doped β-alumina. Coupled with the fact that only one type of F^+ center has been reported in neutron-irradiated Al_2O_3 [147],

these previously reported results would provide some circumstantial evidence that the presence of lithium may also be required for the metastable F^{+*} center to exist.

7.2.2 The Aluminum Vacancy.

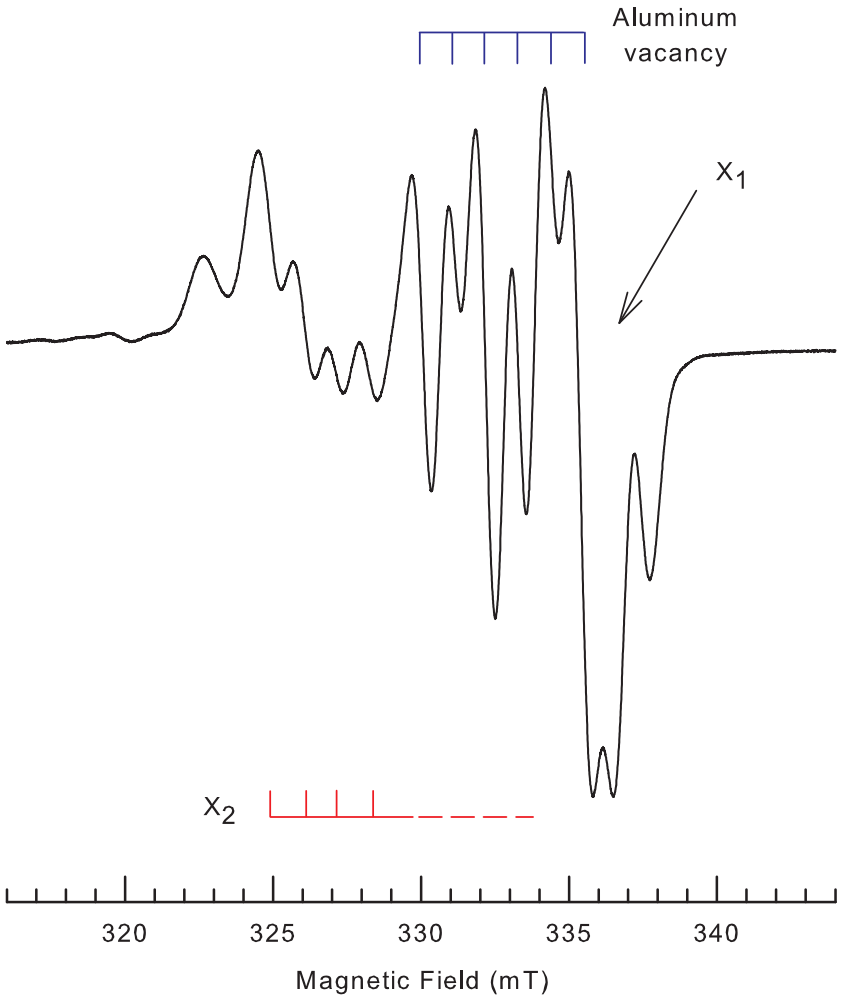

Figure 7.3. EPR spectrum from a a neutron-irradiated $LiAlO_2$ crystal, taken at 36 K and with high microwave power. The set of six equally spaced lines are assigned to doubly ionized aluminum vacancies. The X_1 and X_2 signals have not been identified.

The EPR signals that were off-scale in the middle of the spectra in Figure 7.1 can be seen more clearly in Figure 7.3. Figure 7.3 was obtained from the sample that was irradiated for 3 hours with the magnetic field along the [001] direction, a temperature of 36 K, and with a microwave power of 2 mW. There are at least three distinct

defects, and possibly more, contributing to the EPR spectrum in Figure 7.3. Neutron irradiation can produce several types of point defects such as paramagnetic aggregates of vacancies (e.g., dimers, and trimers, etc.) in addition to isolated vacancies. Also, interstitial ions may be contributing to one or more of the observed spectra. In Figure 7.3, a set of six equally spaced lines can easily been seen and identified with the blue stick diagram above the spectrum. This six-line EPR spectrum is assigned to a doubly ionized aluminum vacancy (V_{Al}^{2-}, $S = 1/2$) produced during the neutron irradiation. In this defect, a hole is trapped on an oxygen ion adjacent to the aluminum vacancy. There was little angular dependence observed for the six-line spectrum. This would indicate that the trapped hole may be rapidly hopping among all four of the oxygen ions that surround an aluminum vacancy instead of being localized on only one of the neighboring oxygen ions. The holelike g value of 2.019 and a ^{27}Al hyperfine splitting parameter of 1.09 mT would also indicate a vacancy assignment. These values are very similar to the g and ^{27}Al hyperfine parameters of the 11-line trapped hole EPR spectrum discussed in Chapter 4. The other EPR lines in Figure 7.3 have not been identified with any defect. This includes the single intense line, labeled X_1 located near 335 mT and the set of lines, labeled X_2, that extend from 324.5 mT to possibly near 335 mT. A line at low field near 322 mT, and a line at high field near 337.5 mT, also remain unidentified.

The 11-line trapped hole EPR spectrum is not present in the neutron-irradiated $LiAlO_2$ spectrum of Figure 7.3. In order to eliminate the possibility that the temperature at the sample during irradiation was hot enough to have inadvertently annealed out the 11-line spectrum, the neutron-irradiated sample was subsequently irradiated with x rays at room temperature. The 11-line EPR signal still did not appear after the x ray irradiation. Thus, there appear to be no, or very few, isolated lithium vacancies in a neutron-irradiated lithium aluminate crystal, even though large con-

centrations of lithium vacancies are known to be present in as-grown crystals. One possible explanation for the absence of the 11-line spectrum is the trapping of oxygen interstitials by lithium vacancies, which was suggested to have occurred in MgO [143]. Once a lithium vacancy has trapped an oxygen interstitial, it can no longer serve as a simple hole trap. This theory is supported by the fact that after a neutron-irradiated $LiAlO_2$ crystal is heated to 600 °C, and exposed to x rays at room temperature, the 11-line trapped hole EPR spectrum is once again the primary defect visible. This would indicate that the heating allowed the oxygen interstitials to recombine with oxygen vacancies, which frees up the lithium vacancies to once again trap holes on adjacent oxygen ions as discussed in Chapter 4.

7.3 Optical Absorption Results

Figure 7.4 shows the optical absorption spectrum (blue curve) of the $LiAlO_2$ crystal taken at room temperature after a 3 hour irradiation with neutrons. Unpolarized light propagated along the [001] direction in the crystal and the path length (i.e., thickness) was 0.5 mm. The primary band in Figure 7.4 has a peak near 238 nm (5.21 eV) and is assigned to F^+ centers. This 238 nm absorption peak was initially observed by Auvray-Gely *et al* in $LiAlO_2$ crystals irradiated with high-energy electrons [94]. Katsui *et al* also observed this peak after irradiating a $LiAlO_2$ single crystal with deuterons (D_2^+) [106]. Evidence that the 238 nm optical absorption band is due to F^+ centers is provided by the thermal annealing results reported in Section 7.4.

As shown in Figure 4.8, there are no absorption bands in the $200 - 300$ nm region in an as-grown crystal. Also, the 238 nm absorption peak does not appear after x ray irradiation at room temperature of an as-grown crystal (the x rays are unable to create oxygen vacancies through a direct momentum-conserving displacement mechanism

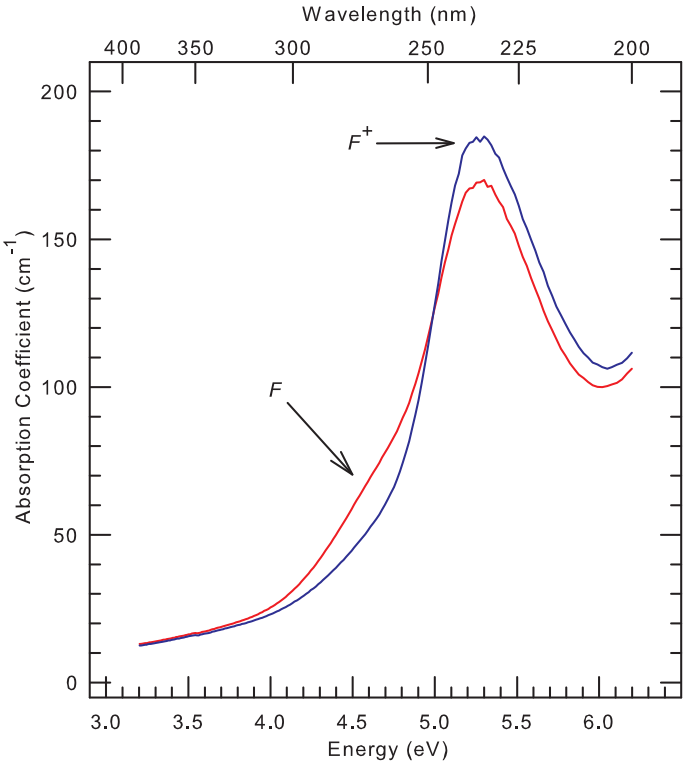

Figure 7.4. Room-temperature optical absorption spectra of a $LiAlO_2$ crystal. The blue curve was taken after the neutron irradiation. The red curve was taken after exposing the irradiated crystal to a Hg lamp. The F^+ band peaks near 238 nm and the F band peaks near 272 nm.

and would only be able to change the charge state of pre-existing oxygen vacancies). The lack of a 238 nm absorption band would indicate that there are very few, if any, oxygen vacancies initially present in Czochralski-grown $LiAlO_2$ crystals. The lack of an observable x ray-induced F^+ center EPR spectrum before neutron irradiation also supports the absence of oxygen vacancies in the as-grown crystals. These results taken together establish that the oxygen vacancies represented by the EPR spectra in Figure 7.1 and the 238 nm absorption band in Figure 7.4 were produced by displacement events initiated by high-energy neutrons.

There is a weak shoulder near 272 nm (4.56 nm) on the low energy side of the primary absorption band taken after neutron irradiation in Figure 7.4 (blue curve). If a neutron irradiated $LiAlO_2$ crystal is exposed to a low-intensity Hg lamp, the main

238 nm absorption band is reduced and the absorption band at 272 nm is enhanced as shown for the red curve in Figure 7.4. The most likely explanation is that light from the Hg lamp releases electrons from unidentified traps (Fe^+ or other transition-metal ions). The released electrons are then trapped by F^+ centers, which then become F centers (an oxygen vacancy with two trapped electrons). The broad, less intense, absorption band peaking near 272 nm in the red curve in Figure 7.4 is assigned to the F center. In both CaO and SrO crystals, the F center optical absorption band occurs at a lower energy than the F^+ center absorption band [148, 149]. The portion of F^+ centers that are converted to F centers in $LiAlO_2$ by the Hg lamp is controlled by the number and types of electron traps present. After using light from the Hg lamp to increase the intensity of the 272 nm absorption band, exposing the crystal at room temperature to 325 nm light from a He-Cd laser decreased the intensity of the 272 nm band.

A value for the oscillator strength f of the F^+ band can be determined by combining the EPR and optical absorption results from the same sample. The oscillator strength is a characteristic parameter of a defect that is related to the probability that an optical transition will result in absorption. Smakula's equation, in the form appropriate for a Gaussian-shaped band, can be used to calculate f [150]. It is given by

$$Nf = (0.87 \times 10^{17}) \frac{n}{(n^2+2)^2} \alpha_{\max} W \tag{7.2}$$

where N is the concentration of absorbing species, n is the index of refraction at a given peak position, $\alpha_{\max}$ is the absorption coefficient of the peak height, and W is the full width at half maximum of the absorption peak. N was determined to be $1.1 \times 10^{-19} \mathrm{cm}^{-3}$ from Figure 7.1 and equation (3.2). If the baseline of the absorption band for the blue curve in Figure 7.4 is not zero but increases with energy, then the absorption coefficient $\alpha_{\max}$ at the peak is approximately 135 cm^{-1} and W is 0.90 eV.

The index of refraction at the peak is approximately 1.65 [37]. Substituting these quantities into equation (7.2) gives an oscillator strength of 0.07 for the 238 nm F^+ center absorption band in $LiAlO_2$ crystals.

7.4 Thermal Stability of the F^+ Center

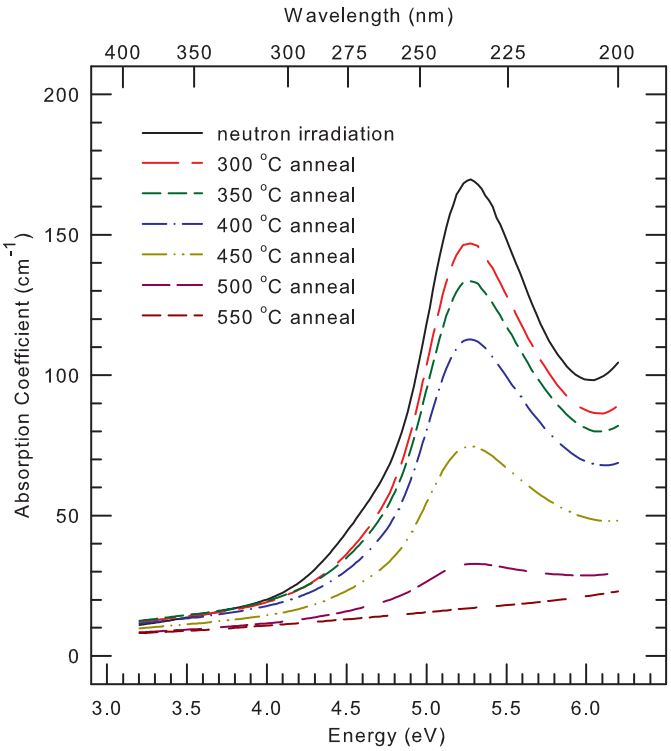

Figure 7.5. Thermal stability of the 238 nm optical absorption band assigned to F^+ centers. The sample was held at each temperature for 1 minute and then returned to room temperature where the absorption spectrum was recorded.

A thermal anneal study was performed on the $LiAlO_2$ crystal that had been irradiated with neutrons for 3 hours. Both the EPR spectra of the F^+ centers and the 238 nm optical absorption band were monitored. In these experiments, the crystal was held for 1 minute at a series of progressively higher temperatures. After each anneal step, the crystal was returned to room temperature where the optical absorption spectrum was taken, and then cooled to 100 K where the EPR spectrum was

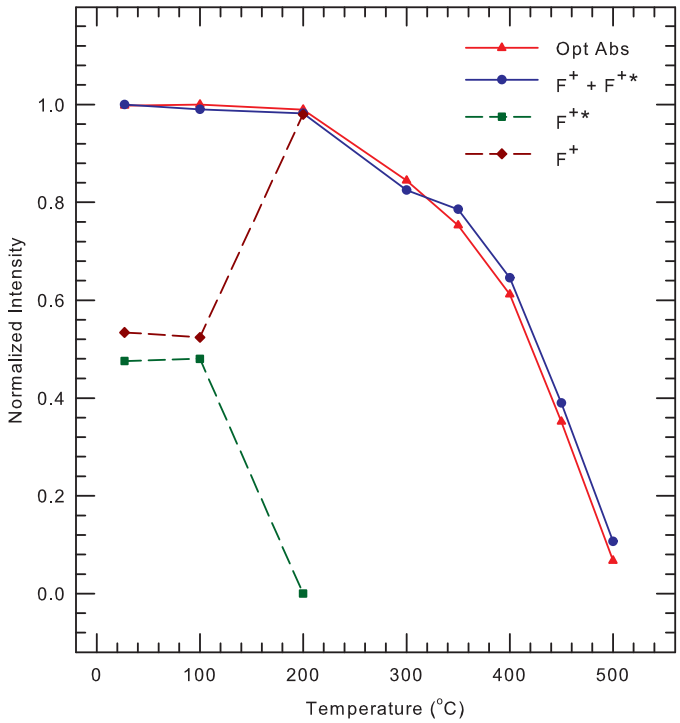

Figure 7.6. Correlation of the thermal decay of the 238 nm optical absorption band and the EPR spectra representing the F^+ and F^{+*} centers. During the first annealing step, the F^+ and F^{+*} centers are both present (as indicated by the dashed green and dark red lines). The blue curve represents the total number of F^+ and F^{+*} centers.

taken. Figure 7.5 illustrates how the intensity of the 238 nm optical absorption band decreases with increasing temperature. Figure 7.6 shows the excellent correlation of the optical absorption peak and EPR intensities as a function of annealing temperature, which confirms that these spectra have a common origin. The temperature where half of the F^+ centers have thermally decayed is approximately 425 °C.

In Figure 7.6, the blue curve represents the combined F^+ and F^{+*} intensities. At the beginning of the thermal anneal (i.e., at room temperature), both F^+ and F^{+*} centers are present in the EPR spectrum. Both of these defects are also present after the 100 °C anneal step. After the 200 °C anneal step, the F^{+*} centers have disappeared and the intensity of the F^+ center EPR spectrum has increased by the amount the F^{+*} spectrum decreased. These effects are illustrated by the dashed lines (green and dark red) in Figure 7.6 and also by the EPR spectra in Figure 7.1. As

described in subsection 7.2.1, this thermally induced conversion of F^{+*} centers to F^{+} centers strongly suggests that the F^{+*} centers are a metastable state of the F^{+} centers.

7.5 PL and PLE of the F Center

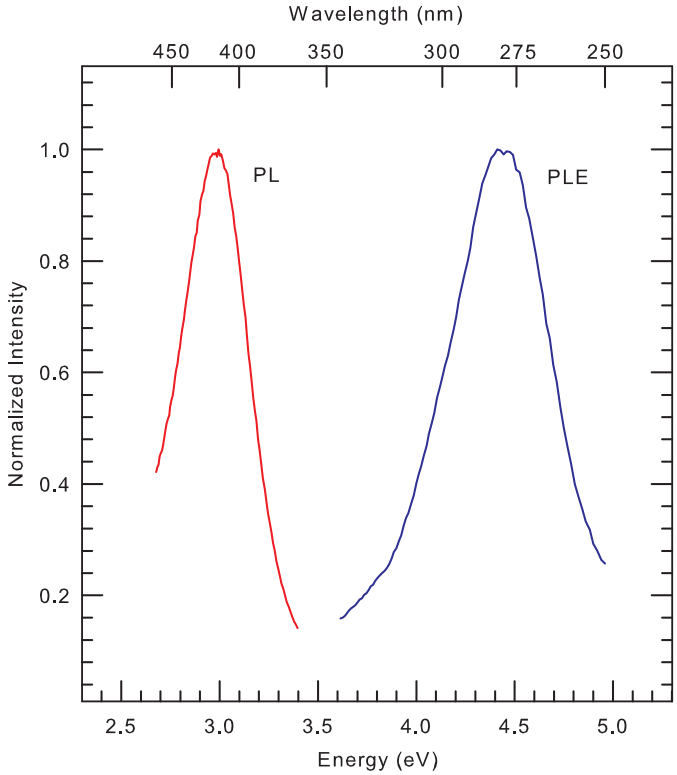

Figure 7.7. Photoluminescence (PL) and photoluminescence excitation (PLE) spectra obtained from a neutron-irradiated $LiAlO_2$ crystal. The responsible defect is the F center.

Figure 7.7 shows the PL and PLE spectra taken at room temperature from the $LiAlO_2$ crystal irradiated for 3 hours with neutrons. The emission band was obtained using an excitation wavelength of 300 nm. It peaks at 411 nm (3.02 eV) and has a full width at half maximum (FWHM) of 0.36 eV. The related excitation band was obtained by monitoring the emission at 410 nm. This PLE band peaks near 277 nm (4.48 eV) and has a FWHM of 0.57 eV. The resulting Stoke's shift of 1.46 eV is

large. Before recording the spectra in Figure 7.7, the crystal was held at 300 °C for 1 minute. Heating to 300 °C destroyed defect aggregates that were contributing interfering spectra to the emission and excitation, thereby allowing "clean" PL and PLE spectra to be obtained. The PLE and PL spectrum have been corrected to account for variations in excitation lamp output, detection system response, and wavelength to energy conversions. The PL peak position shifts to 416 nm (2.98 eV) after these corrections are applied. These corrections are explained in detail in [151].

Comparison of the PLE band in Figure 7.7 with the optical absorption spectra in Figure 7.4 shows that the PLE band does not coincide with the F^+ center absorption band (blue spectrum in Figure 7.4) peaking at 238 nm. This lack of correlation eliminates the F^+ center as the defect responsible for the PL band. The peak of the PLE spectrum is, however, close to the peak of the F center band that appears as a shoulder of the F^+ absorption band when the crystal is exposed to the Hg lamp (red spectrum in Figure 7.4). The difference between the peak of the PLE band and the peak of the F center band is small (272 vs 277 nm). This small difference is believed to be experimental and arises from the difficulty in identifying the peak position of the F center absorption band in Figure 7.4 and also in correcting the PLE spectrum for variations in excitation lamp intensity. This suggests that the PLE and optical absorption bands have a common origin, and allows an assignment of the PL and PLE spectra in Figure 7.7 to F centers.

There does not appear to be an emission band at room temperature associated with the F^+ center absorption band at 238 nm. Repeated attempts using excitations wavelengths between 235 and 250 nm failed to find any PL emission bands, other than the 411 nm band in Figure 7.7, from a neutron-irradiated crystal. Also, a preliminary search with a crystal at 77 K did not reveal any new PL band. The absence of a luminescence band associated with the F^+ centers in $LiAlO_2$ can be explained

using the phenomenological model of Bartram and Stoneham [152]. They noted that emission is expected to be quenched when the cross-over point of the excited state and ground state curves in a two-state configuration-coordinate diagram occurs below the energy reached in absorption. Their empirical relationships, based on the phonon energies and relative ionic radii, suggest that emission should not be expected from the F^+ centers in lithium aluminate crystals.

VIII. Summary and Conclusion

Ionizing and particle-irradiation induced point defects in $LiAlO_2$ have been aggressively identified and characterized. Large numbers of lithium vacancies are present in as-grown lithium aluminate single crystals that serve as hole traps after exposure to ionizing radiation. An oxygen ion adjacent to a lithium vacancy will trap a hole, creating an O^- paramagnetic defect. This defect has an equal hyperfine interaction with the two adjacent ^{27}Al ions and produces an intense 11-line EPR spectra centered around 332 mT. These trapped-hole defects become thermally unstable around 105 °C; they release their holes which recombine with trapped electrons at transition-metal ions and are responsible for a thermoluminescence peak centered at 105 °C.

Iron serves as the primary transition-metal impurity in as-grown $LiAlO_2$. Fe^{2+} replaces Li^+ during growth and serves as an electron trap under ionizing radiation. When Fe^{2+} traps an electron and converts to Fe^+, a very intense single EPR line becomes visible centered at 141.5 mT. The Fe^+ also induces broad optical absorption centered around 379 nm that is not present prior to exposure to ionizing radiation. Fe^+ is the trapped-electron defect that participates in thermoluminescence by serving as the primary electron-hole recombination site.

Copper-$LiAlO_2$ has the potential to serve as an excellent OSL dosimeter. After diffusing copper into $LiAlO_2$ crystals at high temperatures, an intense optical absorption band is produced centered at 277 nm. This peak has the same origin as a PLE band at 273 nm, which is the Cu^+ $3d^{10} \rightarrow 3d^9 4s^1$ transition. During the diffusion process, copper ions replace Li^+ ions in $LiAlO_2$ creating the PLE and optical absorption bands. A PL band at 359 nm is associated with the PLE band. After exposure to ionizing radiation, some of the Cu^+ is converted into Cu^{2+} by trapping a hole on an adjacent oxygen ion. This gives rise to two Cu^{2+} EPR spectra, one spectrum from isolated Cu^{2+} (with no lithium vacancies nearby), and one from Cu^{2+}

adjacent to a lithium vacancy. The isolated Cu^{2+} participates in the OSL response of copper-diffused $LiAlO_2$, by trapping electrons released from Fe^{+} after exposure to 425 nm excitation light. A strong OSL signal is produced from the recombination of electrons and holes that occurs at the Cu^{2+} site.

During exposure to neutron irradiation, three distinct EPR spectra from oxygen and aluminum vacancies are observed. The singly-ionized oxygen vacancy EPR spectra shows 36 lines arising from inequivalent hyperfine interactions and spin density sharing among the two ^{27}Al ions adjacent to the oxygen vacancy. There are two types of oxygen vacancy signals, a stable (F^+ center) and a metastable (F^{+*} center) state. The metastable state becomes thermally unstable around 200 °C and converts over to the stable state. An intense optical absorption peak appears at 238 nm that is thermally correlated with the intensities of the oxygen vacancy EPR signals. An excitation band peaking near 277 nm and an emission band peaking near 411 nm are caused by the neutral oxygen vacancy (F center). No excitation band or emission band associated with either F^+ center state has been detected.

$LiAlO_2$ is a very promising material for neutron scintillation, OSL radiation dosimetry, and as a tritium breeding material. A thorough understanding of point defect behavior in this material after exposure to ionizing and neutron irradiation is crucial for nuclear application optimization. This dissertation has contributed to a thorough and in-depth understanding of the fundamental physics occurring in lithium aluminate single crystals under ionizing and neutron irradiation. A suggestion for future work would be to study the behavior of hydrogen and tritium in $LiAlO_2$. The current research focus on tritium breeding blankets has been primarily concerned with measuring the rate of tritium release and mechanical properties of lithium ternary oxides [138, 153, 154]. The rate of recovery of tritium cannot be adequately explained without understanding how tritium interacts with the surrounding lattice and only

EPR can truly provide such insight.

A useful EPR experiment would start with neutron-irradiating a single crystal of $LiAlO_2$ long enough so that the amount of tritium produced in the sample would exceed the $5 \times 10^{10}\,cm^{-3}$ minimum spin threshold for EPR detectability. If an EPR signal from tritium were identified in the sample, it could be characterized with the same techniques used in the previous chapters. Measurements of the angular dependence and thermal stability of the EPR signal could determine where tritium sits in the crystal lattice (e.g., on a lithium site or forming an OH with an oxygen), as well as if any correlation exists with the F^+ center and the aluminum vacancy. It would be useful in such an experiment to have samples that have received multiple doses, and samples that have been shielded from high energy neutrons with those that have not. Samples that receive only thermal neutrons would contain tritium but little displacement damage versus those exposed to fast and thermal neutrons. If the behavior of tritium release can be understood in the absence of other neutron-generated defects, that may facilitate a better understanding of tritium release behavior when oxygen and aluminum vacancies are present. Understanding those factors could explain why tritium is released from neutron-irradiated lithium compounds at a given rate and how to optimize the rate of release.

Another future area of research is to study point defects and optical properties of $LiAlO_2$ doped with other compounds. Some optical measurements have been carried out on $LiAlO_2$ doped with Cr, Mn, Ce, Tb, Eu, and Ti but an exploration of point defects in these materials has been inadequate [5,26,100–102]. So far, only speculation concerning point defect behavior and suspect EPR assignments from polycrystalline samples currently exist. A good EPR experiment would involve single crystals of $LiAlO_2$ doped with different light emitting elements and to multiple dopant levels. Many of these elements have characteristic hyperfine splitting that would aid in the

identification of any associated EPR signals, which could then be characterized and correlated with any observed optical properties such as thermoluminescence or OSL.

Bibliography

1. X. Ke, X. Jun, D. Peizhen, Z. Yongzong, Z. Guoqing, Q. Rongsheng, and F. Zujie, "γ-$LiAlO_2$ single crystal: a novel substrate for GaN epitaxy," *Journal of Crystal Growth*, vol. 193, no. 1-2, pp. 127–132, September 1998.

2. Y. J. Sun, O. Brandt, U. Jahn, T. Y. Liu, A. Trampert, S. Cronenberg, S. Dhar, and K. H. Ploog, "Impact of nucleation conditions on the sructural and optical properties of M-plane GaN $(1\bar{1}00)$ grown on γ-$LiAlO_2$," *Journal of Applied Physics*, vol. 92, no. 10, pp. 5714–5719, November 2002.

3. K. Munkata, Y. Yokoyama, A. Baba, T. Kawagoe, T. Takeishi, M. Nishikawa, R. D. Penzhorn, H. Moriyma, K. Kawamoto, Y. Morimoto, and K. Okuno, "Tritium release from catalytic breeder materials," *Fusion Engineering and Design*, vol. 58-59, pp. 683–687, November 2001.

4. M. Oyaidzu, T. Takeda, H. Kimura, A. Yoshikawa, M. Okada, K. Munakata, M. Nishikawa, and K. Okuno, "Correlation between annihilation of radiation defects and tritium release in neutron-irradiated $LiAlO_2$," *Fusion Science and Technology*, vol. 48, no. 1, pp. 638–641, July 2005.

5. J. Pejchal, Y. Fujimoto, V. Chani, F. Moretti, T. Yanagida, M. Nikl, Y. Yokota, A. Beitlerova, A. Vedda, and A. Yoshikawa, "Crystal growth and luminescence properties of Ti-doped $LiAlO_2$ for neutron scintillator," *Journal of Crystal Growth*, vol. 318, no. 1, pp. 828–832, March 2011.

6. Y. Fujimoto, K. Kamada, T. Yanagida, N. Kawaguchi, S. Kurosawa, D. Totsuka, K. Fukuda, K. Watanabe, A. Yamazaki, Y. Yokota, and A. Yoshikawa, "Lithium Aluminate Crystals as Scintillator for Thermal Neutron Detection," *IEEE Transactions on Nuclear Science*, vol. 59, no. 5, pp. 2252–2255, October 2012.

7. J. I. Lee, A. S. Pradhan, J. L. Kim, I. Chang, B. H. Kim, and K. S. Chung, "Preliminary study on development and characterization of high sensitivity $LiAlO_2$ optically stimulated luminescence material," *Radiation Measurements*, vol. 47, no. 9, pp. 837–840, September 2012.

8. ——, "Characteristics of $LiAlO_2$ - Radioluminescence and optically stimulated luminescence," *Radiation Measurements*, vol. 56, pp. 217–222, 2013.

9. A. Twardak, P. Bilski, B. Marczewska, and W. Gieszcyk, "Analysis of TL and OSL kinetics of lithium aluminate," *Radiation Measurements*, vol. 71, pp. 143–147, December 2014.

10. A. Twardak, P. Bilski, B. Marczewska, J. I. Lee, J. L. Kim, W. Gieszcyk, A. Mrozik, M. Sadel, and D. Wrobel, "Properties of lithium aluminate for application as an OSL dosimeter," *Radiation Physics and Chemistry*, vol. 104, pp. 76–79, November 2014.

11. K. S. Krane, *Introductory Nuclear Physics*. John Wiley & Sons, Inc., 1988, section 14.1.

12. ITER. (2014) Tritium breeding. ITER. [Online]. Available: http://www.iter.org/mach/TritiumBreeding

13. H. Nakaya, H. Matsuura, Y. Nakao, S. Shimakawa, M. Goto, S. Nakagawa, and M. Nishikawa, "Core configuration of a gas-cooled reactor as a tritium production device for fusion reactor," *Nuclear Engineering and Design*, vol. 271, pp. 505–209, May 2014.

14. Department of Homeland Security. About the domestic nuclear detection office. Department of Homeland Security. [Online]. Available: http://www.dhs.gov/about-domestic-nuclear-detection-office

15. J. P. McKelvey, *Solid State Physics*. Krieger Publishing Company, 1993, chapter 9.

16. M. Fox, *Optical Properties of Solids*. Oxford University Press, 2010, chapter 5.

17. G. F. Knoll, *Radiation Detection and Measurement*, 4th ed. John Wiley & Sons, Inc., 2010, section 8.II.A.

18. C. W. E. van Eijk, "Inorganic scintillator for thermal neutron detection," *Radiation Measurements*, vol. 38, no. 4-6, pp. 337–342, August-December 2004.

19. G. W. Hollenberg, "Fast Neutron Irradiation Results on Li_2O, Li_4SiO_4, Li_2ZrO_3 and $LiAlO_2$," *Journal of Nuclear Materials*, vol. 123, pp. 896–900, May 1984.

20. J. L. Ethridge, D. E. Baker, and A. D. Miller, "Effects of Fast Neutron Irradiation on Thermal Conductivity of Li_2O and $LiAlO_2$," *Journal of the American Ceramic Society*, vol. 71, no. 6, pp. C294–C296, June 1988.

21. F. Agullo-Lopez, C. R. A. Catlow, and P. D. Townsend, *Point Defects in Materials*. Academic Press, 1988.

22. F. Seitz, "Color Centers in Alkali Halide Crystals," *Reviews of Modern Physics*, vol. 18, no. 3, pp. 384–408, July 1946.

23. T. E. Mitchell and A. H. Heuer, "Solution Hardening by Aliovalent Cations in Ionic Crystals," *Materials Science and Engineering*, vol. 28, no. 1, pp. 81–97, April 1977.

24. M. H. Auvray-Gely and A. Dunlop, "Defect Production by X- and Gamma-Rays in Gamma Lithium Aluminate," *Nuclear Instruments & Methods in Physics Research B*, vol. 32, pp. 23–27, May 1988.

25. M. H. Auvray-Gely, A. Perez, and A. Dunlop, "Electron paramagnetic resonance and optical absorption studies of irradiated lithium aluminate," *Philosophical Magazine Part B*, vol. 57, no. 2, pp. 137–148, 1988.

26. M. Yamaga, J. P. R. Wells, M. Honda, T. P. J. Han, and B. Henderson, "Investigation on the valence of Cr ions in $LiAlO_2$," *Journal of Luminescence*, vol. 108, no. 1-4, pp. 313–317, June 2004.

27. Diamond 3.0 software. Crystal Impact. [Online]. Available: http://www.crystalimpact.com/diamond/Default.htm

28. M. M. Chou, H. C. Huang, D.-S. Gan, and C. W. Hsu, "Defect characterizations of γ-$LiAlO_2$ single crystals," *Journal of Crystal Growth*, vol. 291, no. 2, pp. 485–490, June 2006.

29. M. Marezio and J. P. Remeika, "High-Pressure Synthesis and Crystal Structure of α-$LiAlO_2$," *The Journal of Chemical Physics*, vol. 44, no. 8, pp. 3143–3144, April 1966.

30. C. H. Chang and J. L. Margrave, "High-Pressure-High-Temperature Syntheses. III. Direct Syntheses of New High-Pressure Forms of $LiAlO_2$ and $LiGaO_2$ and Polymorphism in $LiMO_2$ Compounds (M=B, Al, Ga)," *Journal of the American Chemical Society*, vol. 90, no. 8, pp. 2020–2022, April 1968.

31. A. K. Fischer, "Atmospheric Pressure Synthesis for β-$LiAlO_2$," *Inorganic Chemistry*, vol. 16, no. 4, pp. 974–974, April 1977.

32. T. Hahn, Ed., *International Tables for Crystallography: Brief Teaching Edition of Volume A*, 5th ed., ser. Space-Group Symmetry. John Wiley & Sons, Ltd, 2010, p. 128.

33. M. Marezio, "The Crystal Structure and Anomalous Dispersion of γ-$LiAlO_2$," *Acta Crystallographica*, vol. 19, no. 3, pp. 396–400, September 1965.

34. S. Indris and P. Heitjans, "Local electronic structure in a $LiAlO_2$ single crystal studied with ^{7}Li NMR spectroscopy and comparison with quantum chemical calculations," *Physical Review B*, vol. 74, no. 24, p. 5120, December 2006.

35. S. Q. Wu, Z. F. Hou, and Z. Z. Zhu, "First-principles study on the structural, elastic, and electronic properties of γ-$LiAlO_2$," *Computational Materials Science*, vol. 46, no. 1, pp. 221–224, July 2009.

36. T. Huang, S. Zhou, H. Teng, H. Lin, J. Zou, J. Zhou, and J. Wang, "Growth and Characterization of High-quality $LiAlO_2$ Single Crystal," *Journal of Materials Science & Technology*, vol. 24, no. 2, pp. 145–148, March 2008.

37. B. Cockayne and B. Lent, "The Czochralski Growth of Single Crystal Lithium Aluminate, $LiAlO_2$," *Journal of Crystal Growth*, vol. 54, no. 3, pp. 546–550, September 1981.

38. B. Velickov, A. Mogilatenko, R. Bertram, D. Klimm, R. Uecker, W. Neumann, and R. Fornari, "Effects of the Li-evaporation on the Czochralski growth of γ-$LiAlO_2$," *Journal of Crystal Growth*, vol. 310, no. 1, pp. 214–220, January 2008.

39. C. Cohen-Tannoudji, B. Diu, and F. Laloe, *Quantum Mechanics*. Wiley-VCH Verlag GmbH & Co. KGaA, 2005, vol. 1 and 2, chapter IX.

40. J. A. Weil and J. R. Bolton, *Electron Paramagnetic Resonance: Elementary Theory and Practical Applications*, 2nd ed. John Wiley & Sons, Inc, 2007, p. 15.

41. A. Abragam and B. Bleaney, *Electron Paramagnetic Resonance of Transition Ions*. Oxford University Press, 1970, p. 3.

42. J. A. Weil and J. R. Bolton, *Electron Paramagnetic Resonance: Elementary Theory and Practical Applications*, 2nd ed. John Wiley & Sons, Inc, 2007, figure 1.9.

43. C. Cohen-Tannoudji, B. Diu, and F. Laloe, *Quantum Mechanics*. Wiley-VCH Verlag GmbH & Co. KGaA, 2005, vol. 1 and 2, p. 971.

44. J. A. Weil and J. R. Bolton, *Electron Paramagnetic Resonance: Elementary Theory and Practical Applications*, 2nd ed. John Wiley & Sons, Inc, 2007, figure 1.8.

45. ——, *Electron Paramagnetic Resonance: Elementary Theory and Practical Applications*, 2nd ed. John Wiley & Sons, Inc, 2007, p. 21-23.

46. ——, *Electron Paramagnetic Resonance: Elementary Theory and Practical Applications*, 2nd ed. John Wiley & Sons, Inc, 2007, table E.1.

47. ——, *Electron Paramagnetic Resonance: Elementary Theory and Practical Applications*, 2nd ed. John Wiley & Sons, Inc, 2007, p. 21.

48. ——, *Electron Paramagnetic Resonance: Elementary Theory and Practical Applications*, 2nd ed. John Wiley & Sons, Inc, 2007, p. 525.

49. J.-M. Spaeth and H. Overhof, *Point Defects in Semiconductors and Insulators*, ser. Springer Series in Materials Science, R. M. O. Jr., R. Hull, and J. Parisi, Eds. Springer-Verlag, 2003, vol. 51, p. 35.

50. ——, *Point Defects in Semiconductors and Insulators*, ser. Springer Series in Materials Science, R. M. O. Jr., R. Hull, and J. Parisi, Eds. Springer-Verlag, 2003, vol. 51, p. 45-47.

51. ——, *Point Defects in Semiconductors and Insulators*, ser. Springer Series in Materials Science, R. M. O. Jr., R. Hull, and J. Parisi, Eds. Springer-Verlag, 2003, vol. 51, p. 46.

52. J. A. Weil and J. R. Bolton, *Electron Paramagnetic Resonance: Elementary Theory and Practical Applications*, 2nd ed. John Wiley & Sons, Inc, 2007, chapter 12.

53. M. Fox, *Optical Properties of Solids*. Oxford University Press, 2010, section 9.2.

54. C. Cohen-Tannoudji, B. Diu, and F. Laloe, *Quantum Mechanics*. Wiley-VCH Verlag GmbH & Co. KGaA, 2005, vol. 1 and 2, p. 1279.

55. R. Pappalardo, "Absorption Spectra of Cu^{2+} in Different Crystal Coordinations," *Journal of Molecular Spectroscopy*, vol. 6, pp. 554–571, 1961.

56. H. A. Weakliem, "Optical Spectra of Ni^{2+}, Co^{2+}, and Cu^{2+} in Tetrahedral Sites in Crystals," *The Journal of Chemical Physics*, vol. 36, no. 8, pp. 2117–2140, April 1962.

57. M. Fox, *Optical Properties of Solids*. Oxford University Press, 2010, figure 9.1.

58. ——, *Optical Properties of Solids*. Oxford University Press, 2010, section 9.1.

59. D. S. McClure, *Electronic Spectra of Molecules and Ions in Crystals*. New York, New York: Academic Press, 1959, p. 88.

60. ——, *Electronic Spectra of Molecules and Ions in Crystals*. New York, New York: Academic Press, 1959, p. 50, p. 92.

61. C. Cohen-Tannoudji, B. Diu, and F. Laloe, *Quantum Mechanics*. Wiley-VCH Verlag GmbH & Co. KGaA, 2005, vol. 1 and 2, p. 67.

62. D. O. O'Connell, B. Henderson, and J. M. Bolton, "Unixial Stress and Polarisation Studies of F_2 Centre Luminescence in MgO," *Solid State Communications*, vol. 38, no. 4, pp. 283–285, April 1981.

63. M. Fox, *Optical Properties of Solids*. Oxford University Press, 2010, p. 3.

64. C. Furetta, "Thermoluminescence," *Rivista Del Nuovo Cimento*, vol. 21, no. 2, pp. 1–62, February 1998.

65. ——, "Review-Models in thermoluminescence," *Journal of Materials Science*, vol. 39, no. 7, pp. 2277–2294, April 2004.

66. A. J. J. Bos, "Theory of Thermoluminescence," *Radiation Measurements*, vol. 41, no. S1, pp. S45–S56, December 2006.

67. R. C. DuVarney, A. K. Garrison, and R. H. Thorland, "Electron Paramagnetic and Nuclear Double Resonance of F^+ Centers in BeO Single Crystals," *Physical Review*, vol. 188, no. 2, pp. 657–661, December 1969.

68. Y. Chen and M. M. Abraham, "Trapped-Hole Centers in Alkaline-Earth Oxides," *Journal of Physics and Chemistry of Solids*, vol. 51, no. 7, pp. 747–764, 1990.

69. S. McKeever, *Thermoluminescence of solids*. The Pitt Building, Trumpington Street, Cambridge CB2 1RP: Cambridge University Press, 1985, chapter 3.

70. E. G. Yukihara, S. W. S. McKeever, and M. S. Akselrod, "State of art: Optically stimulated luminescence dosimetry-Frontiers of future reasearch," *Radiation Measurements*, vol. 71, pp. 15–24, December 2014.

71. L. Oster, S. Druzhyna, and Y. S. Horowitz, "Optically stimulated luminescence in LiF:Mg,Ti: Application to solid-state radiation dosimetry," *Nuclear Instruments and Methods in Physics Research A*, vol. 648, no. 1, p. 261, August 2011.

72. S. W. S. McKeever, "Optically stimulated luminescence dosimetry," *Nuclear Instruments and Methods in Physics Research B*, vol. 184, no. 1-2, pp. 29–54, September 2001.

73. Bruker BioSpin Corp, *EMX Series User's Manual*, manual version 1.1. ed., 2009.

74. Wikipedia. (2014, January) Gunn diode. [Online]. Available: http://en.wikipedia.org/wiki/Gunn_diode

75. J. A. Weil and J. R. Bolton, *Electron Paramagnetic Resonance: Elementary Theory and Practical Applications*, 2nd ed. John Wiley & Sons, Inc, 2007, section E.2.2.

76. Wikipedia. (2014, September) Schottky diode. [Online]. Available: http://en.wikipedia.org/wiki/Schottky_diode

77. J. A. Weil and J. R. Bolton, *Electron Paramagnetic Resonance: Elementary Theory and Practical Applications*, 2nd ed. John Wiley & Sons, Inc, 2007, figure E.6.

78. ——, *Electron Paramagnetic Resonance: Elementary Theory and Practical Applications*, 2nd ed. John Wiley & Sons, Inc, 2007, p. 525-529.

79. Private Communication with L. E. Halliburton.

80. Photron. (2014, October) Deuterium lamps. [Online]. Available: http://www.photron.com.au/.assets/brochures/deuterium_lamp.pdf

81. M. Fox, *Optical Properties of Solids*. Oxford University Press, 2010, p. 4.

82. G. F. Knoll, *Radiation Detection and Measurement*, 4th ed. John Wiley & Sons, Inc., 2010, chapter 9.

83. O. F. Schirmer, "O^- bound small polarons in oxide materials," *Journal of Physics: Condensed Matter*, vol. 18, no. 43, pp. R667–R704, November 2006.

84. "MTI Corporation," February 2014. [Online]. Available: http://www.mtixtl.com/

85. J.-M. Spaeth and H. Overhof, *Point Defects in Semiconductors and Insulators*, ser. Springer Series in Materials Science, R. M. O. Jr., R. Hull, and J. Parisi, Eds. Springer-Verlag, 2003, vol. 51, chapter 3.6.

86. J. A. Weil and J. R. Bolton, *Electron Paramagnetic Resonance: Elementary Theory and Practical Applications*, 2nd ed. John Wiley & Sons, Inc, 2007, section 4.4.

87. D. A. Buchanan, "EPR and ENDOR Studies of Point Defects in Lithium Tetraborate Crystals," Ph.D. dissertation, Air Force Institute of Technology, Wright-Patterson Air Force Base, OH, November 2012, appendix B.

88. R. T. Cox, "Electron Spin Resonance Studies of Holes Trapped at Mg^{2+}, Li^+ and Cation Vacancies in Al_2O_3," *Solid State Communications*, vol. 9, no. 22, pp. 1989–1992, November 1971.

89. R. H. D. Nuttall and J. A. Weil, "The magnetic properties of the oxygen-hole aluminum centers in crystalline SiO_2. I. $[AlO_4]^0$," *Canadian Journal of Physics*, vol. 59, no. 11, pp. 1696–1708, November 1981.

90. O. F. Schirmer, "The structure of the paramagnetic lithium center in zinc oxide and beryllium oxide," *Journal of the Physics and Chemistry of Solids*, vol. 29, no. 8, pp. 1407–1429, August 1968.

91. M. W. Swinney, J. W. McClory, J. C. Petrosky, S. Yang, A. T. Brant, V. T. Adamiv, Y. V. Burak, P. A. Dowben, and L. E. Halliburton, "Identification of electron and hole traps in lithium tetraborate ($Li_2B_4O_7$) crystals: Oxygen vacancies and lithium vacancies," *Journal of Applied Physics*, vol. 107, no. 11, p. 9, June 2010.

92. J. A. Weil and J. R. Bolton, *Electron Paramagnetic Resonance: Elementary Theory and Practical Applications*, 2nd ed. John Wiley & Sons, Inc, 2007, p. 105-110.

93. R. H. Bartram, C. E. Swenberg, and J. T. Fournier, "Theory of Trapped-Hole Centers in Aluminum Oxide," *Physical Review*, vol. 139, no. 3A, pp. A941–A951, August 1965.

94. M. H. Auvray-Gely, A. Perez, and A. Dunlop, "Optical Absorption Study of Irradiation Damage in γ-$LiAlO_2$," *Crystal Lattice Defects and Amorphous Materials*, vol. 17, pp. 119–125, 1987.

95. Y. Asaoka, H. Moriyama, K. Iwasaki, K. Moritani, and Y. Ito, "In-situ luminescence measurement of lithium aluminate under ion beam irradiation," *Journal of Nuclear Materials*, vol. 191-194 Part A, pp. 268–271, September 1992.

96. S. Kuck and S. Hartung, "Comparative study of the spectroscopic properties of Cr^{4+}-doped $LiAlO_2$ and $LiGaO_2$," *Chemical Physics*, vol. 240, no. 3, pp. 387–401, January 1999.

97. G. A. Waychunas and G. R. Rossman, "Spectroscopic Standard for Tetrahedrally Coordinated Ferric Iron: γ $LiAlO_2$:Fe^{3+}," *Physica and Chemistry of Minerals*, vol. 9, no. 5, pp. 212–215, May 1983.

98. T. Kutty and M. Nayak, "Cation Coordination and Fe^{3+} Luminescence in $LiAlO_2$ Polymorphs Prepared by a Hydrothermal Method," *Materials Research Bulletin*, vol. 34, no. 2, pp. 249–262, January 1999.

99. N. Suriyamurthy, B. S. Panigrahi, and A. Natarajan, "Luminescence study of iron doped lithium aluminate phosphor," *Materials Science and Engineering A*, vol. 403, no. 1-2, pp. 182–185, Augsut 2005.

100. B. Dhabekar, E. A. Raja, S. Menon, T. K. G. Rao, R. K. Kher, and B. C. Bhatt, "Identification of defect centres using TSL, PL, OSL and ESR studies in $LiAlO_2$ based phosphors," *Journal of Physics D: Applied Physics*, vol. 41, no. 11, pp. 1–6, June 2008.

101. M. G. Brik, H. Teng, H. Lin, S. Zhou, and N. M. Avram, "Spectroscopic and crystal field studies of $LiAlO_2$:Mn^{2+} single crystals," *Journal of Alloys and Compounds*, vol. 506, no. 1, pp. 4–9, September 2010.

102. X. Yang, G. Ning, X. Li, and Y. Lin, "Synthesis and luminescence properties of a novel Eu^{3+}-doped γ-$LiAlO_2$ phosphor," *Materials Letters*, vol. 61, no. 25, pp. 4694–4696, October 2007.

103. M. Fox, *Optical Properties of Solids*. Oxford University Press, 2010, p. 366, Problem 1.13.

104. ——, *Optical Properties of Solids*. Oxford University Press, 2010, problem 2.13.

105. O. F. Schirmer, "Optical Absorption of Small Polarons Bound in Octahedral Symmetry: V^- Type Centers in Alkaline Earth Oxides," *Zeitschrift für Physik B*, vol. 24, no. 3, pp. 235–244, September 1976.

106. H. Katsui, S. Nagata, B. Tsuchiya, M. Zhao, and T. Shikama, "Damage and deuterium retention in $LiAlO_2$ single crystals irradiated with deuterium ions using ion-beam techniques and optical absorption measurements," *Journal of Nuclear Materials*, vol. 417, no. 1-3, pp. 753–755, October 2011.

107. J. A. Weil and J. R. Bolton, *Electron Paramagnetic Resonance: Elementary Theory and Practical Applications*, 2nd ed. John Wiley & Sons, Inc, 2007, section 10.2.

108. ——, *Electron Paramagnetic Resonance: Elementary Theory and Practical Applications*, 2nd ed. John Wiley & Sons, Inc, 2007, p. 307.

109. G. F. Foster and H. Statz, "Method of Treating Zeeman Splittings of Paramagnetic Ions in Crystalline Fields," *Physical Review*, vol. 113, no. 2, pp. 445–454, January 1959.

110. B. Bleaney, "The Spin Hamiltonian of a Γ_8 Quartet," *Proceedings of the Physical Society*, vol. 73, no. 6, pp. 939–942, June 1959.

111. J. A. Weil and J. R. Bolton, *Electron Paramagnetic Resonance: Elementary Theory and Practical Applications*, 2nd ed. John Wiley & Sons, Inc, 2007, section 6.7.

112. F. S. Ham, G. W. Ludwig, G. D. Watkins, and H. H. Woodbury, "Spin Hamiltonian of Co^{2+}," *Physical Review Letters*, vol. 5, no. 10, pp. 468–470, November 1960.

113. W. C. Holton, J. Schneider, and T. L. Estle, "Electron Paramagnetic Resonance of Photosensitive Iron Transition Group Impurities in ZnS and ZnO," *Physical Review*, vol. 133, no. 6A, pp. 1638–1641, March 1964.

114. A. K. Garrison, "Electron Paramagnetic Resonance of NaF:Fe^+," *Materials Research Bulletin*, vol. 2, no. 2, pp. 155–164, February 1967.

115. U. Kaufmann, "EPR and optical absorption of Fe^+, Fe^{2+}, Fe^{3+}, and Fe^{4+} on tetragonal sites in $CdSiP_2$," *Physical Review B*, vol. 14, no. 5, pp. 1848–1857, September 1976.

116. J. M. Baker, A. A. Jenkins, and R. C. C. Ward, "Electron paramagnetic resonance in lithium oxide from a centre containing Fe^{3+}," *Journal of the Physics: Condensed Matter*, vol. 3, no. 43, pp. 8467–8477, October 1991.

117. UC Davis Chem Wiki. (2015) Hund's rules. [Online]. Available: http://chemwiki.ucdavis.edu/Inorganic_Chemistry/Electronic_Configurations/Hund%27s_Rules

118. A. Abragam and B. Bleaney, *Electron Paramagnetic Resonance of Transition Ions*. Oxford University Press, 1970, section 3.14.

119. E. Malguth, A. Hoffmann, W. Gehlhoff, O. Gelhausen, M. R. Phillips, and X. Xu, "Structural and electronic properties of Fe^{3+} and Fe^{2+} centers in GaN from optical and EPR experiments," *Physical Review B*, vol. 74, no. 16, p. 165202, October 2006.

120. J. L. Dean, Ed., *Lange's Handbook of Chemistry*, 14th ed. McGraw Hill, LoCo, 1992, table 4.6.

121. S. V. Nistor, M. V. Stefánescu, and D. C. Mateescu, "A Study On Fe^{+} Centers in NaCl Crystals," *Solid State Communications*, vol. 53, no. 11, pp. 989–992, March 1985.

122. S. V. Nistor, I. Ursu, and M. Velter-Stefanescu, "Electron-trapped centers in x-irradiated LiCl:Fe crystals," *Physical Review B*, vol. 35, no. 10, pp. 4594–4601, April 1987.

123. E. Boseman, F. Callens, J. Haes, F. Maes, P. Matthys, and P. Moens, "EPR of KCl:Fe," *Solid State Communications*, vol. 77, no. 12, pp. 931–935, March 1991.

124. J. C. Mittani, M. Prokić, and E. G. Yukihara, "Optically stimulated luminescence and thermoluminescence of terbium-activated silicates and aluminates," *Radiation Measurements*, vol. 43, no. 2-6, pp. 323–326, February-June 2008.

125. J. Pejchal, Y. Fujimoto, V. Chani, T. Yanagida, Y. Yokota, A. Yoshikawa, M. Nikl, and A. Beitlerova, "Modifications of micro-pulling down method for growth of selected Li -containing crystals for neutron scintillator and VUV scintillation crystals," *Journal of Crystal Growth*, vol. 360, pp. 127–130, December 2012.

126. G. D. Patra, M. Tyagi, D. G. Desai, B. Tiwari, S. Sen, and S. C. Gadkari, "Photo-luminescence properties of Cu and Ag doped $Li_2B_4O_7$ single crystals at low temperatures," *Journal of Luminescence*, vol. 132, no. 5, pp. 1101–1105, May 2012.

127. G. D. Patra, S. G. Singh, B. Tiwari, S. Sen, D. G. Desai, and S. C. Gadkari, "Thermally stimulated luminescence process in copper and silver co-doped lithium tetraborate single crystals and its implication to dosimetry," *Journal of Luminescence*, vol. 137, pp. 28–31, May 2013.

128. R. Oggioni and P. Scaramelli, "Optical Absorption and Photoluminescence of Cu-Doped Alkali Halide Crystals," *Physica Status Solidi (b)*, vol. 9, no. 2, pp. 411–421, 1965.

129. J. Simonetti and D. S. Mcclure, "The $3d \rightarrow 4p$ transitions of Cu^+ in LiCl and of transition-metal ions in crystals," *Physical Review B*, vol. 16, no. 9, pp. 3887–3892, November 1977.

130. R. L. Bateman and W. J. V. Sciver, "Optical Absorption by the Cu^+ Center in NaI," *Physica Status Solidi (b)*, vol. 46, no. 2, pp. 779–784, August 1971.

131. R. R. Patil and S. V. Moharil, "On the role of copper impurity in LiF:Mg, Cu, P phosphor," *Journal of Physics: Condensed Matter*, vol. 7, no. 50, pp. 9925–9933, December 1995.

132. B. Tiwari, N. S. Rawat, D. G. Desai, S. G. Singh, M. Tyagi, P. Ratna, S. C. Gadkari, and M. S. Kulkarni, "Thermoluminescence studies of Cu-doped $Li_2B_4O_7$ single crystals," *Journal of Luminescence*, vol. 130, no. 11, pp. 2076–2083, November 2010.

133. N. S. Rawat, M. S. Kulkarni, M. Tyagi, P. Ratna, D. R. Mishra, S. G. Singh, B. Tiwari, A. Soni, S. C. Gadkari, and S. K. Gupta, "TL and OSL studies on lithium borate single crystals doped with Cu and Ag," *Journal of Luminescence*, vol. 132, no. 8, pp. 1969–1975, August 2012.

134. Z. Jun, Z. Sheng-Ming, L. Yang, W. Jun, Z. Lian-Han, and X. Jun, "Spectra Analysis of a Novel Ti-Doped $LiAlO_2$ Single Crystal," *Chinese Physics Letters*, vol. 22, no. 10, pp. 2622–2625, October 2005.

135. H. Teng, S. Zhou, H. Lin, T. Jia, X. Hou, and J. Wang, "Growth and characterization of high-quality Mn-doped $LiAlO_2$ single crystal," *Chinese Optics Letters*, vol. 8, no. 4, pp. 414–417, April 2010.

136. B. Dhabekar, E. A. Raja, S. Menon, T. K. G. Rao, R. K. Kher, and B. C. Bhatt, "ESR, PL and TL studies of $LiAlO_2$:Mn/Ce phosphor," *Radiation Measurements*, vol. 43, no. 2-6, pp. 291–294, February-June 2008.

137. A. T. Brant, D. A. Buchanan, J. W. McClory, P. A. Dowben, V. T. Adamiv, Y. V. Burak, and L. E. Halliburton, "EPR identification of defects responsible for thermoluminescence in Cu-doped lithium tetraborate ($Li_2B_4O_7$) crystals," *Journal of Luminescence*, vol. 139, pp. 125–131, July 2013.

138. M. Nishikawa, T. Kinjyo, T. Ishizaka, S. Beloglazov, T. Takeishi, M. Enoeda, and T. Tanifuji, "Release behavior of bred tritium from $LiAlO_2$," *Journal of Nuclear Materials*, vol. 335, no. 1, pp. 70–76, October 2004.

139. J. Tombrello, H. T. Tohver, Y. Chen, and T. M. Wilson, "EPR detection of substitutional H^{2-} ion in magnesium oxide," *Physical Review B*, vol. 30, no. 12, p. 7374, December 1984.

140. R. Pandey and J. M. Vail, "F-type centres and hydrogen anions in MgO: Hartree-Fock ground states," *Journal of Physics: Condensed Matter*, vol. 1, no. 17, pp. 2801–2820, May 1989.

141. M. M. Kuklja, E. V. Stefanovich, E. A. Kotomin, A. I. Popov, R. González, and Y. Chen, "***Ab initio*** and semiempirical calculations of H^- centers in MgO crystals," *Physical Review B*, vol. 59, no. 3, pp. 1885–1890, January 1999.

142. A. Janotti and C. G. Van de Walle, "Hydrogen multicentre bonds," *Nature Materials*, vol. 6, no. 1, pp. 44–47, January 2007.

143. L. E. Halliburton and L. A. Kappers, "Radiation-induced oxygen interstitials in MgO," *Solid State Communications*, vol. 26, no. 2, pp. 111–114, April 1978.

144. S. Stoll and A. Schweiger, "EasySpin, a comprehensive software package for spectra simulation and analysis in EPR," *Journal of Magnetic Resonance*, vol. 178, no. 1, pp. 42–55, January 2006.

145. R. C. DuVarney, A. K. Garrison, J. R. Niklas, and J. M. Spaeth, "Electron-nuclear double resonance of the F^+ center in α-alumina," *Physical Review B*, vol. 24, no. 7, pp. 3693–3696, October 1981.

146. S. R. Kurtz, D. G. Stinson, H. J. Stapleton, and M. M. Abraham, "EPR and electron-nuclear double-resonance studies of an F^+ center in sodium, potassium, and lithium β-alumina," *Physical Review B*, vol. 24, no. 9, pp. 4983–4998, November 1981.

147. S. Y. La, R. H. Bartram, and R. T. Cox, "The F^+ Center in Reactor-Irradiated Aluminum Oxide," *Journal of Physics and Chemistry of Solids*, vol. 34, no. 6, pp. 1079–1086, June 1973.

148. B. P. Johnson and E. B. Hensley, "Additive Coloration of Strontium Oxide," *Physical Review*, vol. 180, no. 3, pp. 931–933, April 1969.

149. B. Henderson, S. E. Stokowski, and T. C. Ensign, "Luminescence from F Centers in Calcium Oxide," *Physical Review*, vol. 183, no. 3, pp. 826–830, July 1969.

150. D. L. Dexter, "Absorption of Light by Atoms in Solids," *Physical Review*, vol. 101, no. 1, pp. 48–55, January 1956.

151. I. P. Ferguson, "Photoluminescence and Optically Stimulated Luminescence Studies of $LiAlO_2$ and $LiGaO_2$ Crystals," Master's thesis, Air Force Institute of Technology, March 2015.

152. R. H. Bartram and A. M. Stoneham, "On the Luminescence and Absence of Luminescence of *F* Centers," *Solid State Communications*, vol. 17, no. 12, pp. 1593–1598, December 1975.

153. Y. Nishikawa, M. Oyaidzu, A. Yoshikawa, K. Munakata, M. Okada, M. Nishikawa, and K. Okuno, "Correlation between tritium release and thermal annealing of irradiation damage in neutron-irradiated Li_2SiO_3," *Journal of Nuclear Materials*, vol. 367-370, no. Part B, pp. 1371–1376, August 2007.

154. D. Zhu, T. Oda, Y. Shono, and S. Tanaka, "Release behavior of hydrogen isotopes thermally sorbed in Li_2TiO_3," *Journal of Nuclear Materials*, vol. 442, no. Supplement 1, pp. 437–441, November 2013.

REPORT DOCUMENTATION PAGE

Form Approved
OMB No. 0704–0188

1. REPORT DATE *(DD–MM–YYYY)*	2. REPORT TYPE	3. DATES COVERED *(From — To)*
17–09–2015	Dissertation	October 2012 — September 2015

4. TITLE AND SUBTITLE

CHARACTERIZATION OF POINT DEFECTS IN LITHIUM ALUMINATE ($LiAlO_2$) SINGLE CRYSTALS

5a. CONTRACT NUMBER

5b. GRANT NUMBER

5c. PROGRAM ELEMENT NUMBER

6. AUTHOR(S)

Maurio S. Holston, CPT, USA

5d. PROJECT NUMBER

14P168

5e. TASK NUMBER

5f. WORK UNIT NUMBER

7. PERFORMING ORGANIZATION NAME(S) AND ADDRESS(ES)

Air Force Institute of Technology
Graduate School of Engineering and Management (AFIT/EN)
2950 Hobson Way
WPAFB OH 45433-7765

8. PERFORMING ORGANIZATION REPORT NUMBER

AFIT-ENP-DS-15-S-025

9. SPONSORING / MONITORING AGENCY NAME(S) AND ADDRESS(ES)

POC: MAJ Thomas McQuary (thomas.mcquary@dtra.mil)
Defense Threat Reduction Agency
8725 John J. Kingman Rd
Ft. Belvoir, VA 22060

10. SPONSOR/MONITOR'S ACRONYM(S)

DTRA

11. SPONSOR/MONITOR'S REPORT NUMBER(S)

12. DISTRIBUTION / AVAILABILITY STATEMENT

DISTRIBUTION STATEMENT A:
APPROVED FOR PUBLIC RELEASE; DISTRIBUTION UNLIMITED.

13. SUPPLEMENTARY NOTES

This material is declared a work of the U. S. Government and is not subject to copyright protection in the United States

14. ABSTRACT

Lithium aluminate ($LiAlO_2$) is an insulating wide-band gap material currently under development for tritium breeding and radiation detection and dosimetry applications. Point defects are imperfections in a crystal lattice localized over a few atomic lengths that can alter the electrical, mechanical, or optical properties of materials. An understanding of point defect behavior is a necessary precursor for optimizing lithium aluminate for nuclear applications. This dissertation has identified and characterized the major point defects created and induced through x-ray and neutron radiation using electron paramagnetic resonance and fluorescence spectroscopy, thermoluminescence, and optical absorption. This dissertation explains for the first time the mechanism responsible for OSL in copper-diffused $LiAlO_2$ and characterizes for the first time the hole (Li vacancies) and electron-trapping (F and F^+ centers and transition-metal ions) defects. These results should prove useful to any researcher that utilizes $LiAlO_2$ in applications involving radiation.

15. SUBJECT TERMS

$LiAlO_2$, EPR, neutron detection, photoluminescence, thermoluminescence, optical absorption, lithium, oxygen, vacancies, x rays, optically stimulated luminescence

16. SECURITY CLASSIFICATION OF:			17. LIMITATION OF ABSTRACT	18. NUMBER OF PAGES	19a. NAME OF RESPONSIBLE PERSON
a. REPORT	b. ABSTRACT	c. THIS PAGE			Dr. John McClory, AFIT/ENP
U	U	U	UU	143	19b. TELEPHONE NUMBER *(include area code)* (937) 255-3636 x7308 john.mcclory@us.af.mil